

Department of Photonics Engineering
Technical University of Denmark



TERAHERTZ TIME-DOMAIN SPECTROSCOPY OF CHALCOGENIDE GLASSES
AND DEVICES FOR TERAHERTZ RADIATION MANIPULATION

by

Maksim Zalkovskij

September 2013

Abstract

In this thesis I describe experiments utilizing both state of the art cleanroom fabrication processes and several terahertz time-domain spectroscopy systems (THz-TDS).

We have characterized linear optical parameters of two different chalcogenide glasses (As_2S_3 and GaLaS) for ultrabroadband terahertz (THz) spectra spanning from 0.2 to 18 THz. We observed a complicated dispersion profile for both glasses. At low frequencies we observe a monotonously increasing absorption which is a general signature of disordered materials, while at higher frequencies (above 4 THz) we observe absorption features originating from medium-range order in the glasses. Two transparency windows have been identified in As_2S_3 at frequencies 7.2-8.5 and 12-13 THz. Furthermore, utilizing a high power THz-TDS system, we have measured the THz-induced optical Kerr effect in both As_2S_3 and As_2Se_3 , induced by intense THz pulses with peak strengths exceeding 400 kV/cm. To our best knowledge this is the first observation of the THz-induced optical Kerr effect in a solid material.

By the use of cleanroom facility of DTU Danchip we fabricated different designs for manipulation of THz radiation.

- Terahertz antennas with subwavelength gaps for THz electrical field enhancement, revealing strong electromigration effects, when exposed to high intensity THz pulses.
- Polarization-sensitive fractal metamaterials, showing 60 % field transmission at 1 THz for TE polarized light while the TM waves have almost 80 % field transmission at 0.6 THz.
- Optically active metamaterials, with maximum of the polarization plane rotation rate of approximately $500^\circ/\lambda$ at 0.53 THz.
- Transparent metallic electrodes, reaching transmittance of almost 90 % at the resonance frequency of 0.57 THz.

Resume

I denne afhandling beskriver jeg eksperimentalt arbejde som både involver avancerede renrumsfabrikation og forskellige terahertz tid-domæne spektroskopi (THz-TDS) opstillinger.

Vi har karakteriseret de lineære optiske egenskaber af to forskellige chalcogenide glasser (As_2S_3 and GaLaS) med ultra-bredbåndet terahertz (THz) spektroskopi mellem 0.2 og 18 THz. Vi har målt meget komplekse dispersionsprofiler for begge prøver. Ved lave frekvenser ses en monotont stigende absorption, hvilken er en universel opførsel af uordnede materialer. Ved højere frekvenser (over 4 THz) ses absorptionssignaturer som stammer fra mellem-distance orden i glassene. To transparente frekvensbånd er blevet identificeret for As_2S_3 ved frekvenser 7.2-8.5 og 12-13 THz. Ved brug af intens THz-stråling med feltstyrker over 400 kV/cm har vi observeret THz-induceret optisk Kerr effekt i både As_2S_3 and As_2Se_3 . Vi mener at dette er den første observation af THz-induceret optisk Kerr effekt i et fast materiale.

Ved gøre brug af renrumsfaciliteten i DTU Danchip har vi fabrikeret flere forskellige prøver til manipulation af THz stråling.

- Terahertz antenner med en spalte som er meget mindre end bølgelængden til at forstærke det elektriske felt af THz-bølger. Disse strukturer udviser en stor grad af *elektromigration*, når de udsættes for intense THz-pulser.
- Polarisationsfølsomme fraktale metamaterialer, som viste 60 % feltrmission ved 1 THz for TE-polariseret lys, mens TM-bølger havde næsten 80 % feltrmission ved 0.6 THz.
- Optisk aktive metamaterialer med maksimum polarisationsrotation på ca. $500^\circ/\lambda$ ved 0.53 THz.
- Gennemsigtige metalliske elektroder, med transmittans på næsten 90 % ved resonans (0.57 THz).

Preface

The present thesis is the summary of the scientific research carried out as part of my Ph.D. scholar in the period May 1st 2010 – July 1st 2013, at the Technical University of Denmark (DTU). The analytical and characterization/measurement results presented in this thesis are mainly obtained at DTU department of Fotonik, while the micro- and nanofabrication was performed at the cleanroom facility of DTU Danchip. The project was supervised by Associate Professor Andrei Lavrinenko, Professor Peter Uhd Jepsen and Senior Researcher Radu Malureanu.

The thesis is organized in the following way:

Chapter 1 describes three different terahertz time-domain spectroscopy (THz-TDS) systems located at THz laboratory at DTU Fotonik and used during this Ph.D. project.

Chapter 2 covers the THz-TDS results of chalcogenide glasses (ChGs). Results cover both the characterization of linear optical parameters and THz-induced third-order nonlinear response (Keff effect) of ChGs. The ChGs samples were fabricated by Senior Scientific Researcher Aurelian Popescu at National Institute of R&D for Optoelectronics INOE 2000 (Romania).

Chapter 3 describes the THz electrical field enhancement effect in subwavelength metallic slit structures. The fabricated THz antennas with subwavelength gap sizes were exposed with high power THz-TDS systems by Dr. Krzysztof Iwaszczuk, while the numerical prediction of electric field enhancement described in section 3.2.1 was performed by Dr. Andrew C. Strikwerda.

Chapter 4 covers three different designs of THz metamaterials. The behavior of fractal metamaterials (section 4.2.1) and transparent electrodes (section 4.4.1) were numerically determined by the group of Professor Lei Zhou at Fudan University (Shanghai, China). The analytical description of optical active metamaterials (section 4.3.1) was performed by Dr.

Sergei Zhukovsky. The 2 μm thick nickel membranes were mainly fabricated by Senior Researcher Radu Malureanu at DTU Danchip.

This Ph.D. stipendium was financed by The Danish Research Council for Technology and Production Sciences through the project No. 09-070397-FTP. A publication list obtained during this Ph.D. period is presented in section 6.

Kgs. Lyngby, September 23th, 2013



Maksim Zalkovskij

Acknowledgment

This thesis is the result of my Ph.D. scholarship performed in collaboration between *Metamaterials* and *Terahertz Technologies and Biophotonics* located at Technical University of Denmark, the faculty of Fotonik (DTU Fotonik).

First I would like to thank my supervisors Andrei Lavrinenko (DTU Fotonik), Peter Uhd Jepsen (DTU Fotonik) and Radu Malureanu (DTU Fotonik) for making this project possible and for their outstanding guidance, which I am very grateful to. Andrei Lavrinenko for his great job teaching me about light/matter interaction, for teaching me a great deal of Russian terms regarding this area and for great personal guidance during the whole project period. Peter Uhd Jepsen for introducing me to the field of terahertz time-domain spectroscopy for which I have gained a huge amount of passion. Furthermore for greatly improving my skills regarding handling of optical measurement systems. Radu Malureanu for his high involvement during my time at cleanroom. For introducing me to new fabrication techniques as e.g. 3D lithography by direct laser tool, 3D silver deposition and for always having an answer to the issues I run into regarding micro- and nanofabrication.

I would like to thank the rest my colleges at *Metamaterials* and *Terahertz Technologies and Biophotonics* Optofluidics groups, for enjoyable and supportive discussions. I would like to mention few of them that greatly supported and helped me during this project. Former group member David Cooke (now leader of *Terahertz* group at McGill University) for introducing me to the broadband THz-TDS system at DTU Fotonik and assisting me with the first measurements. Jonas Buron for helping out in the terahertz laboratory and for fruitful discussions and advices. I am very grateful to both Krzysztof Iwaszczuk and Andrew C. Strikwerda for assisting me with high power THz-TDS measurements and for time spent with building and optimizing high power THz-TDS system during winter/spring 2013, which made it possible to measure THz-induced Kerr effect in chalcogenide glasses presented in this thesis. I want to thank former group member Andrey Novitsky for his support and work on field enhancement in metallic subwavelength slits. I am grateful to Sergei Zhukovsky for his

work on the description of optical active metamaterial and his huge support with manuscript writing.

I would like to express my sincere gratitude to the entire staff at DTU DanShip for always helping and teaching me a lot on nano- and microfabrication during the last five years of my scientific career.

A special thanks to the administration of DTU Fotonik, specially Birgitte Lydik Paaske, Charlotte Melgaard Larsen, Lone Bjørnstjerne and Anja Sohn Henriksen, for being of great help during my daily work.

I thank my wonderful friends Sebastian, Edwin and Arthur for their great support in all aspects of my life.

Finally I would like to thank my mom, Liidia, and brother, Andrej, for their unlimited love!

Contents

Abstract.....	ii
Resume.....	iv
Preface	vi
Acknowledgment	viii
1 Chapter 1 Terahertz time domain spectroscopy	1
1.1 Introduction to terahertz spectrum.....	1
1.2 Terahertz pulse generation and detection by photoconductive switch.....	2
1.2.1 Generation	4
1.2.2 Detection.....	5
1.2.3 THz-TDS based on PC switch at DTU Terahertz laboratory	5
1.3 Terahertz pulse generation and detection with a laser induced gas plasma	8
1.3.1 Generation	8
1.3.2 Detection.....	9
1.3.3 ABCD THz-TDS system located at DTU Terahertz laboratory	11
1.4 Terahertz pulse generation in LiNbO ₃ crystal and electro optical detection.....	15
1.4.1 Generation in lithium niobate crystal.....	15
1.4.2 Detection by electro-optical sampling.....	18
1.4.3 Lithium niobate THz-TDS system located at DTU Terahertz laboratory.....	21
1.5 Conclusion.....	24
2 Chapter 2 Chalcogenide glasses.....	25
2.1 Introduction to chalcogenide glasses.....	25
2.2 Narrowband terahertz time domain spectroscopy investigation of linear properties of As ₂ S ₃ and GaLaS.....	25

2.3	Broadband terahertz time domain spectroscopy investigation of linear properties of As_2S_3 and GaLaS.	28
2.4	Kerr effect in As_2S_3 and As_2Se_3 glasses.....	35
2.5	Conclusion.....	45
3	Chapter 3 Terahertz field enhancement.....	47
3.1	Introduction.....	47
3.2	Numerical-, fabrication- and characterization results of THz antennas	47
3.2.1	Numerical simulation of THz antennas	47
3.2.2	Fabrication of THz antennas	50
3.2.3	Characterization of THz antennas.....	54
3.3	Conclusion.....	61
4	Chapter 4 Terahertz Metamaterials	63
4.1	Introduction.....	63
4.2	Fractal metamaterials	63
4.2.1	Numerical simulations of fractal metamaterial	64
4.2.2	Fabrication of fractal metamaterial	67
4.2.3	Characterization of fractal metamaterial	70
4.3	Optical active metamaterials	72
4.3.1	Analytical and numerical model	74
4.3.2	Fabrication of optical active metamaterials	78
4.3.3	Characterization of optical active metamaterial	81
4.4	Transparent metallic electrodes based on metamaterials	84
4.4.1	Analytical and numerical model	85

4.4.2	Design.....	90
4.4.3	Fabrication	92
4.4.4	Characterization	95
4.5	Conclusion.....	97
5	Conclusion and outlook	99
6	Ph.D. Publications	103
6.1	Publications related to this thesis.....	103
6.2	Publications unrelated to this thesis.....	105
7	Bibliography	107

List of figures

Figure 1.1: The electromagnetic frequency spectrum.....	1
Figure 1.2: Schematic illustration of photoconductive switch.	3
Figure 1.3: THz pulse generated by a PC switch. (a) time and (b) frequency domain.....	6
Figure 1.4: THz-TDS systems based on PC switches..	7
Figure 1.5: The four-wave mixing method.....	9
Figure 1.6: Illustration of air-biased-coherent-detection..	11
Figure 1.7: The Ti:sapphire amplifier system from Spectra-Physics Spitfire.	12
Figure 1.8: THz pulses generated by four-wave rectification method	13
Figure 1.9: Cherenkov-like cone of emitted THz wave generated by OR.....	16
Figure 1.10: The tilted pulse front configuration.	17
Figure 1.11: The free-space electro-optic (EO) sampling configuration.....	19
Figure 1.12: The LiNbO ₃ THz-TDS setup.....	22
Figure 1.13: THz pulse generated by a LiNbO ₃ THz-TDS system.	23
Figure 2.1: (a) The terahertz pulse is emitted by a photoconductive switch	26
Figure 2.2: Refractive index and absorption coefficient for bulk As ₂ S ₃ sample.	27
Figure 2.3: Refractive index and absorption coefficient for bulk GaLaS samples.	28
Figure 2.4: (a) Sketch of thin film sample deposited on HR Si 1 x 2 cm piece.....	29
Figure 2.5: ABCD THz-TDS setup.	30
Figure 2.6: Measured terahertz pulses with ABCD THz-TDS system.	31
Figure 2.7: The amplitude spectra in the frequency domain.	32

Figure 2.8: Refractive index and absorption coefficient of As_2S_3	33
Figure 2.9: Structure of arsenic sulfide clusters, As_4S_4 and As_2S_3	34
Figure 2.10: Refractive index and absorption coefficient of GaLaS.....	35
Figure 2.11: Schematic illustration of THz-TDS system used for Kerr measurements.	36
Figure 2.12: Illustration of polarizations of probe and THz pulses before entering the sample.	37
Figure 2.13: THz pulse generated by a $LiNbO_3$ crystal.....	38
Figure 2.14: THz-induced birefringence in a As_2S_3 and As_2Se_3	39
Figure 2.15: The peak values of THz-induced signal for As_2S_3 and As_2Se_3	40
Figure 2.16: Kerr signal as a function of rotation angle of As_2S_3	41
Figure 2.17: Refractive index and absorption coefficient for As_2S_3 and As_2Se_3 bulk samples.....	42
Figure 2.18: THz pulse in time domain recorded after passing a 0.716 mm thick As_2S_3	43
Figure 2.19: Nonlinear refractive index of As_2S_3 and As_2Se_3	44
Figure 3.1: Schematical illustration of numerically simulated THz antenna with various	48
Figure 3.2: Electric field distribution for a THz antenna with a gap size of 0.6 μm	49
Figure 3.3: Fabrication flow of THz antennas.	51
Figure 3.4: THz antennas.....	53
Figure 3.5: SEM images of THz antenna	54
Figure 3.6: Illustration of electromigration combined with a SEM image.....	55
Figure 3.7: SEM images of electromigration at different electrical field strengths	56
Figure 3.8: SEM images of electromigration at different electrical field strengths.	57
Figure 3.9: Mapping of the electric field profile of an exited THz antenna.....	59

Figure 4.1: Show schematic pictures of the simulated unit cell structure.	64
Figure 4.2: Show FDTD calculated normal incidence transmission/reflection spectra	65
Figure 4.3: The FDTD calculated electric field distributions inside the fractal slits.....	66
Figure 4.4: FDTD calculated transmission spectra through the fractal PMM	67
Figure 4.5: Main fabrication steps and schematic overview of the structure.	68
Figure 4.6: SEM images of the fractal PMM.	70
Figure 4.7: Measured relative transmission amplitude normalized to air.	71
Figure 4.8: Measured transmission amplitude and transmission phase of fractal PMM.	72
Figure 4.9: Unit cell of Babinet-inverted dimer MM, where two hollow elements are air.....	73
Figure 4.10: SEM image of unit cell showing the unit vectors defining the dimer geometry.	75
Figure 4.11: Transmission spectra τ_{xx} and τ_{yy} for V-shaped and parallel-shaped dimer MM.	76
Figure 4.12: Eigenmode transmission coefficients $t_{1,2}(\omega)$	77
Figure 4.13: SEM images of V-shape and parallel samples with a period of 500 μm	79
Figure 4.14: Optical images of Babinet-inverted dimer MMs.	80
Figure 4.15: Relative amplitude transmission of V-shaped and parallel planar.....	81
Figure 4.16: Relative transmission and circular polarization conversion	83
Figure 4.17: Optical activity for V-shape dimer MM.	84
Figure 4.18: Transparent metallic electrode.	86
Figure 4.19: Schematic illustration of the proposed structure.	86
Figure 4.20: Transmittance as the function of ε_B and P/λ . All other parameters are fixed.	87
Figure 4.21: Transmittance as the function of ε_B and P/λ	89

Figure 4.22: Schematics of AB and C meshes in the xy plane.....	91
Figure 4.23: Simulated transmittance and reflectance spectra of C-layer.....	92
Figure 4.24: Schematic of the fabrication procedure of transparent electrodes.....	93
Figure 4.25: Optical images of fabrication results.	94
Figure 4.26: Measured transmittance of transparent electrodes by T-Ray 4000 THz-TDS system. .	95
Figure 4.27: Transmittance and reflectance for both the whole AB/C device and C-layer.....	96
Figure 4.28: Transmittance and reflectance data comparison between numerical	96

1 Chapter

Terahertz time domain spectroscopy

1.1 Introduction to terahertz spectrum

Terahertz (THz = 10^{12} Hz) radiation is electromagnetic radiation that lies between the microwave and infrared regions of the spectrum, shown in Fig. 1.1. THz radiation is generally defined by the frequency range of 0.1 to 30 THz ($\lambda = 3000\text{-}10\ \mu\text{m}$, $1\ \text{THz} = 300\ \mu\text{m} = 1\ \text{ps} = 10^{-12}\ \text{s} = 33.3\ \text{cm}^{-1} = 4.14\ \text{meV}$).

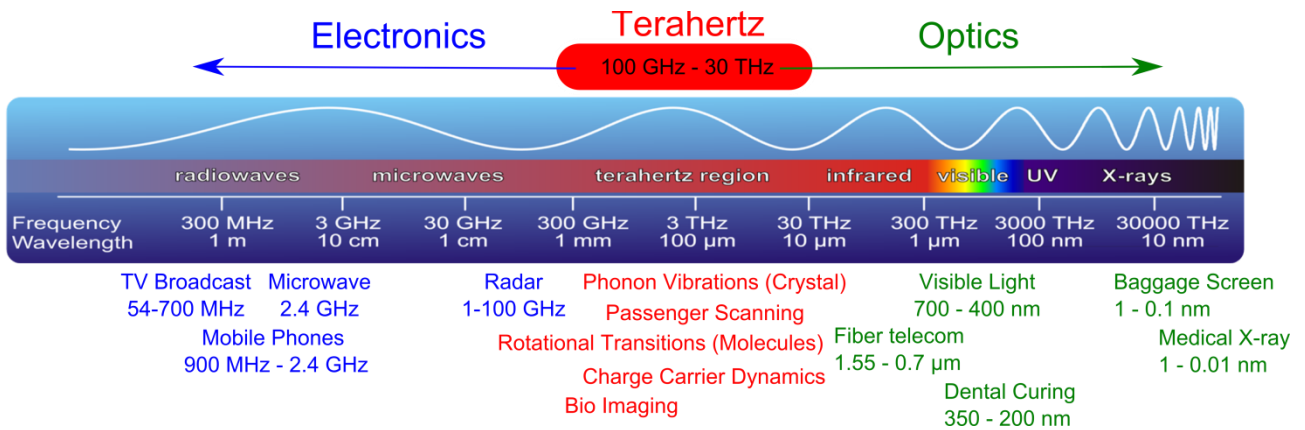


Figure 1.1: The electromagnetic frequency spectrum. The THz region (100 GHz – 30 THz) is located between microwaves and infrared.

The THz spectral range has enormous potential in a broad range of fields. Due to very low photon energies of THz waves (1 THz = 4.14 meV) they have proven to be well suited for diagnostics and imaging of biological tissues [1], [2], [3]. THz waves are non-ionizing and damage to cells or tissues is minimal. Many intriguing results have already been reported in recent years as e.g. imaging of human tumor tissues [4], [5], label-free characterization of genetic material [6] and detection of protein dynamics and solvent dynamics interact during folding [7]. Within communication technology and its increasing requirement for data rates that in near future will reach 5-10 Gb/s [8]. In order to respond to the increasing demand for data rates it is necessary to increase carrier frequency beyond 100 GHz, and therefore move towards THz spectra [9], [10]. Several groups have already presented solutions for guiding

Chapter 1 Terahertz time domain spectroscopy

the THz pulses, where metal waveguides is proven as a good candidate for short range dispersive- and lose- free transmission systems [11], [12], [13], while omnidirectional THz mirrors has the potential to be implemented for free-space communication systems [14]. In security technology THz systems have shown huge perspectives as THz waves can penetrate through many materials e.g. plastic, textile, paper, ceramics, wood among others, which are opaque for optical frequencies. Additionally many solids exhibits characteristic spectral features in THz region, which enables different chemical substances to be detected even inside a mail or closed package [15], [16], [17], [18]. The characteristic feature bands for drugs and explosive span between 0.5 THz and 4.0 THz, where explosives such as e.g. TNT, PETN, HMX and PE4, can be detected [19].

A wide variety of physical phenomena occur at THz frequencies. THz wave interacts with systems that have energy transitions in the meV range and characteristic fixtures takes place in the picosecond range. Therefore the THz spectroscopy has obtained a huge interest as a tool to investigate a wide range of processes. Free carriers in semiconductors strongly absorb THz waves and the peak in the absorption spectrum is located in THz range [20], [21]. Phonon processes in semiconductors [22], chalcogenide glasses [23] and polymorphs [24] also occur at THz frequencies. Water dynamics can also be studied by THz spectroscopy systems. The hydrogen bond rearrangement in water molecules takes place namely in the picosecond time scale [25].

1.2 Terahertz pulse generation and detection by photoconductive switch

Photoconductive (PC) switches for generation and detection of terahertz waves has been the most commonly used technique to date. The main concept of this method, that permits one to use the speed competence of optical pulses to manipulate electrical signals with picosecond time precision, was published as early as in 1975 by D. H. Auston [26]. Here it was shown that by applying DC voltage of 20 V on metallic electrode with a 340 μm wide gap deposited on bare silicon it was possible to achieve electrical signals with a time resolution of a few picoseconds. In 1984 at AT&T Bell Laboratories by D. H. Auston et al. [27], show that

Chapter 1 Terahertz time domain spectroscopy

a PC switch can be used to both generate and detect those extremely rapid electromagnetic picosecond pulses. In 1988 D. Grischkowsky developed and demonstrated the use of PC switches in a free space [28]. Though the THz transient only traveled approximately 2 cm in free space, this work established a solid platform of THz pulse generation and detection that has become standard to THz spectroscopy systems. Remarkably 24 years later D. Grischkowsky and his co-workers guided a THz pulse for 170 meters [29], where both generation and detection was performed by PC switches.

An illustration of a traditional PC switch is shown in Fig. 1.2.

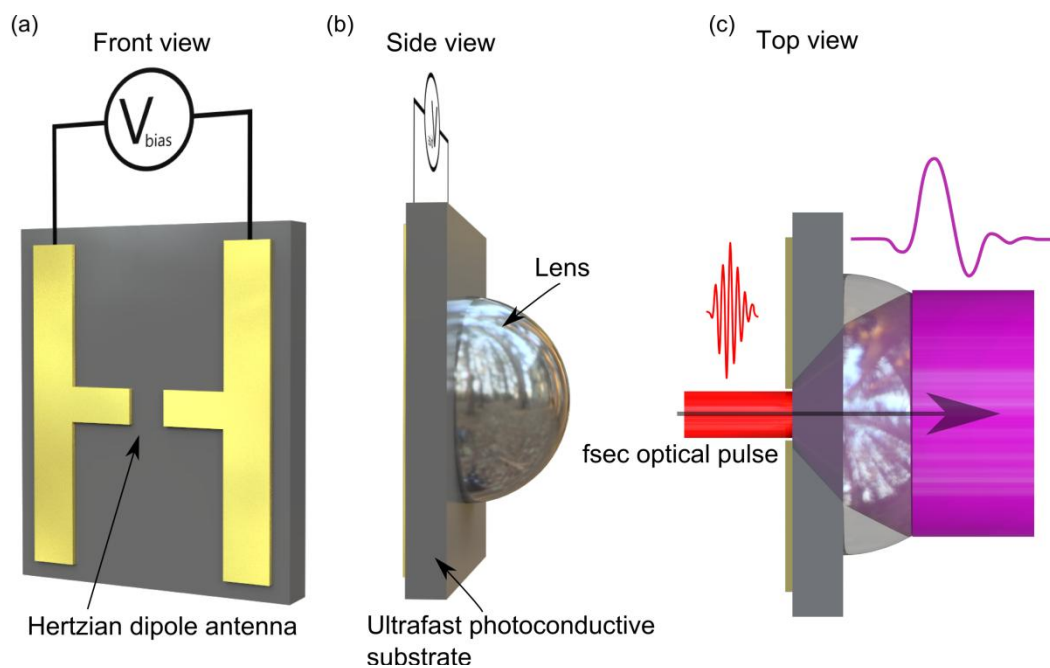


Figure 1.2: Schematic illustration of photoconductive switch from (a) front, (b) side and (c) top view. A dipole antenna placed on ultrafast photoconductive substrate. A femtosecond optical pulse excites free carriers that get accelerated in the antenna gap by the applied bias voltage. The acceleration of free carriers emits THz radiation, which is collected and coupled out by a silicon lens.

A PC switch consist of a semiconductor material, H-shaped metallic electrodes and a silicon lens. There are several requirements for the PC substrate to be used for PC switch. It is crucial that it possess short carrier lifetime, high breakdown voltage and high mobility. Among many candidates (e.g. Si-InP, silicon on sapphire and Cr doped Si-GaAs). The low temperature grown GaAs (LT-GaAs) is perhaps the most frequently chosen. LT-GaAs has ultrafast carrier time in the order of 0.3 ps, high mobility, high resistivity ($10^6 \Omega \cdot \text{cm}$) with

breakdown field of 5×10^5 V/cm and band gap of 1.43 eV. The properties of LT-GaAs depend highly on growth conditions of molecular beam epitaxy (MBE) process and the post-growth annealing. During the growth step the excess of As is merged into GaAs as point defects. These defects can thereafter act as nonradioactive recombination centers that will decrease the free carrier lifetime. Lowering the growth temperature of MBE process, results in higher concentration of those defects, which yields a LT-GaAs with extreme short carrier lifetime. To increase the resistivity of the LT-GaAs it undergoes post-growth annealing process at 600 °C which produces an increase of resistivity from approximately $10 \Omega\cdot\text{cm}$ to $10^6 \Omega\cdot\text{cm}$ and still maintains the short carrier lifetime [30]. The metallic H-shape electrodes that are usually made of gold are deposited in contact with LT-GaAs with a typical gap size of 10-50 μm (Fig. 1.2a). Geometry of metallic electrodes are straightforwardly achieved by standard ultraviolet lithography and therefore the PC switches can be mass produced in a cleanroom facility. A DC bias voltage in the range of 10-30 V is applied on the electrodes for THz generation purpose. The silicon lens is placed on the backside of PC switch in a contact with PC substrate (Fig. 1.2b). It will collect the THz radiation that is emitted at a point source. The lens is made of high resistivity (HR) silicon ($> 10.000 \Omega\cdot\text{cm}$) to minimize the absorption of THz pulse while it propagates through the lens. The refractive index of HR silicon and GaAs at THz frequencies are nicely matched, 3.4 and 3.6 respectively. The matching of refractive index is of high importance to reduce the reflection at the LT-GaAs/HR Si interface.

1.2.1 Generation

The PC switch is operated for generation purpose as followed. The gap between the metallic electrodes is photoexcited with a femtosecond pulse with energy (800nm, 1.55eV) above the energy gap of LT-GaAs (1.46 eV). It will create electron-hole plasma in the exposed area. The electron-hole pairs are accelerated in the gap by the applied electrical DC field, which will create a transient current $\mathbf{J}(t)$. The polarization due to the influence of transient current will create a time dependent opposing field that will screen the electric DC field. This transient field results in generation of electromagnetic radiation, on the order of picoseconds. This process can be described analytically by Maxwell's equations where transient current gives rise to electromagnetic radiation [31]

Chapter 1 Terahertz time domain spectroscopy

$$\nabla \times \mathbf{E}_{THz}(t) = -\mu \frac{\partial \mathbf{H}_{THz}(t)}{\partial t}, \quad (1.1)$$

$$\nabla \times \mathbf{H}_{THz}(t) = \mathbf{J}(t) + \frac{\partial \varepsilon(t) \mathbf{E}_{THz}(t)}{\partial t}, \quad (1.2)$$

where, \mathbf{E}_{THz} is the radiated electrical field, \mathbf{H}_{THz} is the radiated magnetic field intensity, μ and ε are permittivity and permeability respectively of PC substrate. The stimulated electrical field from PC switch will be a few picoseconds long and almost single cycle in nature in time domain, while it will cover a broad range of frequencies in frequency domain. Due to extreme short carrier life time of the PC switch it will recover to its initial state before the arrival of the next optical pulse.

1.2.2 Detection

The detection of THz pulse by PC switch is performed in similar matter as generation. Since the free carrier life time of a PC substrate is much shorter than the duration of the THz pulse, it can act as a sampling gate for the waveform of the THz transient. The optical pulse will photoexcite the free carriers, while the THz pulse will now accelerate them and drive current between electrodes. Therefore instead of applying a DC bias voltage to metallic electrodes (as done in the generation case) the electrodes are now connected to a lock-in amplifier that records the current flow. The lock-in amplifier is locked to the frequency of the modulation of the DC bias voltage applied on emitter. The photocurrent is thereafter recorded as a function of the delay time to obtain the representation of THz pulse in time domain. This is performed by delaying the optical beam path of the detection line by a delay stage. One can also delay the generation path with the respect to detection path.

1.2.3 THz-TDS based on PC switch at DTU Terahertz laboratory

Figure 1.3 show the content of THz pulse both in time and frequency domain.

Chapter 1 Terahertz time domain spectroscopy

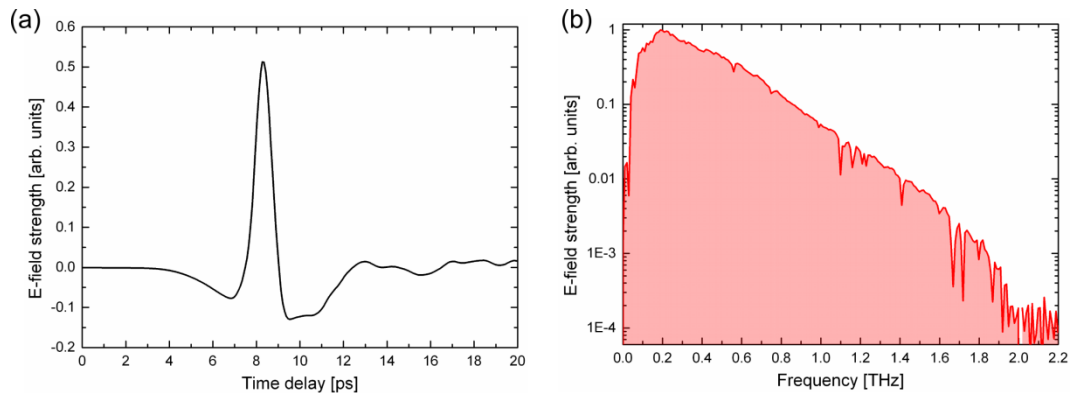


Figure 1.3: THz pulse generated by a PC switch. (a) time and (b) frequency domain.

The THz pulse shown in Fig. 1.3a is generated by a commercial THz time domain spectroscopy (THz-TDS) system, Picometrix T-Ray 4000 [32]. The average of 100.000 waveforms is shown, with signal to noise dynamic range of approximately 10.000 (80 dB power dynamic range) at 0.2 THz. The Picometrix T-Ray 4000 operates at a scan rate of 100 Hz and the total acquisition time of 100.000 waveforms is approximately 17 minutes. Bandwidth up to 2 THz with specific optical configuration was achieved (Fig. 1.3b), though bandwidth up to 5 THz can be realized by the use of PC switches [33].

The PC switches are normally stimulated by a femtosecond Ti:Sapphire laser with a wavelength of 800 nm, a repetition rate of approximately 75-100 MHz, pulse duration in the range of 10–100 fs and average power in the range of 100-300 mW. The stability, reasonable price, “easy to use” interface and little maintenance of Ti:Sapphire femtosecond laser together with the reliable and cheap THz source from a PC switches are some of the reasons of why this method became highly exploited worldwide.

Figure 1.4 shows schematic illustration and optical images of THz-TDS systems used during this project.

Chapter 1

Terahertz time domain spectroscopy

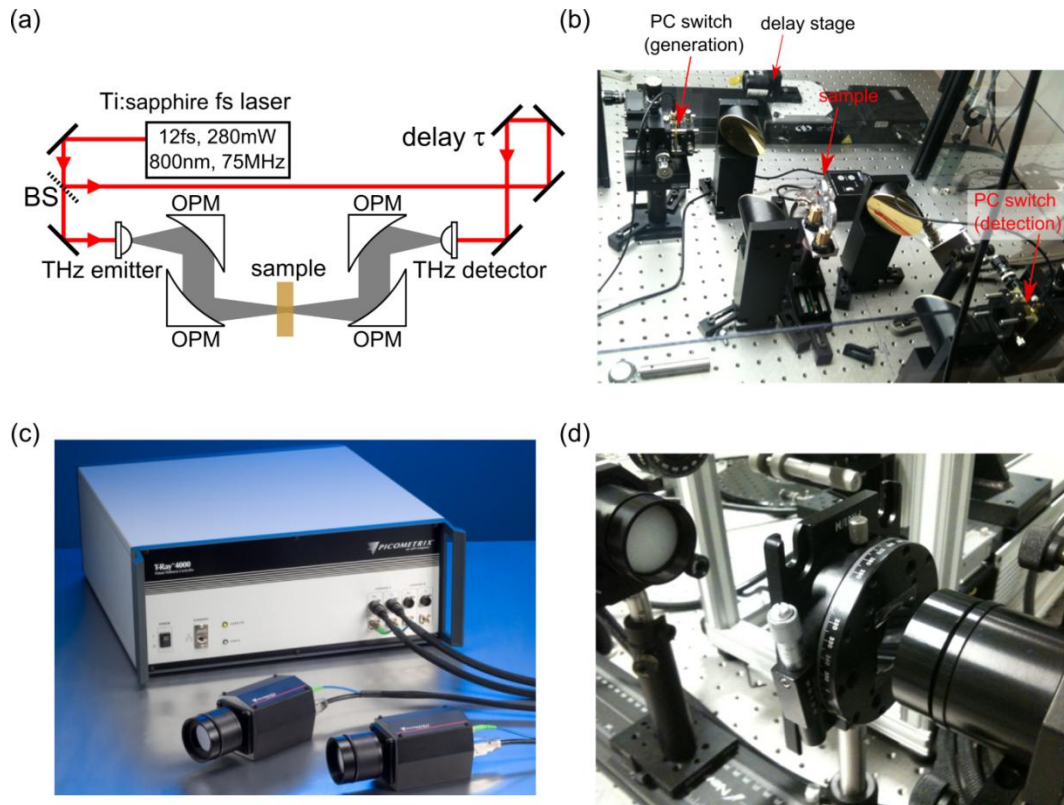


Figure 1.4: THz-TDS systems based on PC switches. (a) Schematic illustration of basic components of THz-TDS system. (b) Optical image of custom build THz-TDS system in transmission configuration. (c) Commercial THz-TDS system (Picometrix T-Ray 4000). (d) Picometrix T-Ray 4000 in transmission configuration.

Figure 1.4a shows the main optical components of THz-TDS systems, which includes femtosecond laser, beam splitter, delay stage, PC switches and passive optical components as e.g. parabolic mirrors. Both custom build (Fig. 1.4b) and commercial THz-TDS system (Fig. 1.4c,d) are able to perform transmission and reflection measurements. In custom build solution it might require several hours, to change from one configuration to another, while it is done in less than 10 minutes with Picometrix solution. The main advantage of the Picometrix T-Ray 4000 system when compared with the custom solution is the fast scan rate of 100 Hz. The scan time of a single THz pulse by custom build setup can take several minutes, depending on time resolution and scan-length. The scan rate of 100 Hz enables not only the fast acquisition of huge set of measured THz waveform, but also allows THz-TDS analysis of large areas, enabling THz-TDS imaging [34].

Though THz-TDS systems based on PC switches are very popular due to the factors such as stability, low cost, fast scan rate and flexibility, there are still a few limitation factors, that

demand other methods for generation and detection of THz pulses. The two main drawbacks of PC switches are the relative low bandwidth (0.2-5 THz) and weak electrical field strength in the order of several V/cm. The next two sections describe other THz-TDS systems that overcome these limitations. First is generation and detection of a THz pulse in a laser induced gas plasma, which yields high bandwidth. Next the following section explains the generation method of a THz pulse in lithium niobate crystal, which enables very high electrical field strength on the order of few MV/cm.

1.3 Terahertz pulse generation and detection with a laser induced gas plasma

1.3.1 Generation

The single cycle THz pulse generation in laser induced gas plasma was first reported in 1993 by H. Hamster et al. [35], almost 10 years after D. H. Auston reported the use of PC switch for generation and detection [27]. H. Hamster et al. has demonstrated that it was possible to generate subpicosecond (FWHM 0.3 ps) single cycle pulses by focusing laser pulses (120 fs, 50 mJ) into helium gas. The concept of this pioneering work has gone on to become a highly recognized method to generate and detect ultrabroadband THz pulses. Several years later in 2000, D. J. Cook et al. introduced an important modification to this method by adding the second harmonic (2ω) to the fundamental wave (ω) [36]. Here the second harmonic pulse is generated by passing the fundamental pulse (65 fs, 800 nm, 150 μ J) through a highly non-linear 100 μ m thick β -barium borate (BBO) crystal. Generation of a THz pulse with high peak electrical field strength (2 kV/cm) was observed when both fundamental and second harmonic were focused either in argon, nitrogen and air. Additionally the high importance, the phase matching of the fundamental and second harmonic pulses was shown. This generation process of a THz pulse is described through a four-wave difference frequency mixing method

$$E_{THz} \propto \chi^{(3)} E_{2\omega} E_{\omega}^* E_{\omega}^*, \quad (1.3)$$

where two fundamental (E_ω) photons are mixed with a single second harmonic ($E_{2\omega}$) photon and through nonlinear third-order optical susceptibility of the gas plasma ($\chi^{(3)}$) generates a photon at THz range (E_{THz}). The four-wave mixing method is illustrated in Fig. 1.5.

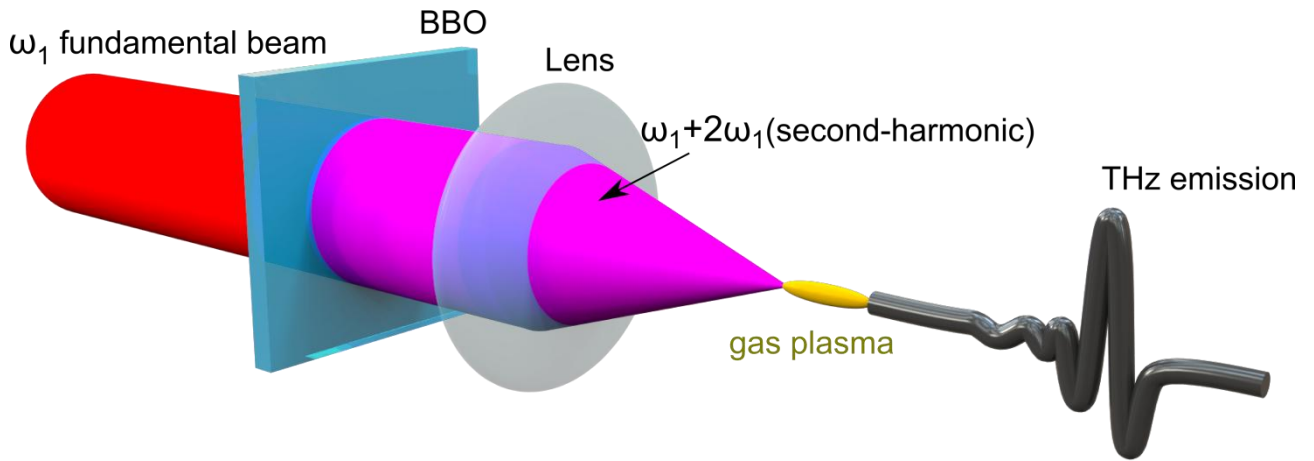


Figure 1.5: The four-wave mixing method. The second harmonic wave ($2\omega_1$) is generated when the fundamental wave (ω_1) passes through β -barium borate (BBO) crystal. Focusing both fundamental and second harmonic results in a gas plasma. THz emission is generated through a four-wave mixing process.

In the mid-2000s several independent groups have made significant and important contribution to this method [37], [38], [39]. During this period the THz field strength was highly improved and values greater than 100 kV/cm were reported [38]. Furthermore different generation schemes were presented and the importance of phase, amplitude, and polarization were described [39].

1.3.2 Detection

The progress of the generation of THz pulses through the four wave mixing processes was developed through the early and mid-2000s and shortly after followed by a scheme for detection of broadband terahertz pulses with a laser induced plasma in gasses [40], [41]. In 2006 the group of X.-C. Zhang reported for the first time that it was possible to detect broadband THz pulses through a third order nonlinear optical process in gasses. The basic mechanism of the detection process is similar to the generation process of four-wave mixing (Eq. (1.3)). By focusing the fundamental probe (ω) beam with a THz pulse, an optical field of second harmonic (2ω) is generated

Chapter 1
Terahertz time domain spectroscopy

$$E_{2\omega} \propto \chi^{(3)} E_{THz} E_{\omega}^* E_{\omega}^* \quad (1.4)$$

Two fundamental photons E_{ω} are mixed with a THz photon E_{THz} and through the nonlinear third-order optical susceptibility of the gas plasma ($\chi^{(3)}$) second harmonic ($E_{2\omega}$) is generated. With a constant probe field the generated second harmonic is proportional to the field strength of THz pulse ($E_{2\omega} \propto E_{THz}$), and therefore the intensity of the second harmonic will also be proportional to the intensity of the THz field ($I_{2\omega} \propto I_{THz}$). This fact makes it possible to record the intensity of the THz pulse directly by measuring the intensity of the second harmonic with a photomultiplier tube (PMT), though this method is incoherent. In same work X.-C. Zhang showed that it was possible to use laser-induced plasma as the local oscillator to obtain a coherent detection and few years later where he presented an implementation of external oscillating (from 0 to π) bias field at gas plasma. By implementing a pair of electrodes and synchronizing the bias field to the modulation frequency of the optical beam, it is possible to change the direction of external bias field from 0 to π relative to every other THz pulse. The intensity of second harmonic field measured by lock-in amplifier (locked to the modulation frequency of the external electrical field), can be written as

$$I_{2\omega} \propto 4 \left(\chi^{(3)} I_{\omega} \right)^2 E_{bias} E_{THz} \quad (1.5)$$

where E_{bias} is the external bias field, E_{THz} is the electrical THz field and I_{ω} is the intensity of probe beam [41]. Since the intensity of second harmonic is proportional with the amplitude of THz field ($I_{2\omega} \propto E_{THz}$), it is possible to record the THz field by measuring the intensity of second harmonic with a PMT. This scheme of measuring the THz pulses is known as air-biased-coherent-detection (ABCD) and is sketched in Fig. 1.6.

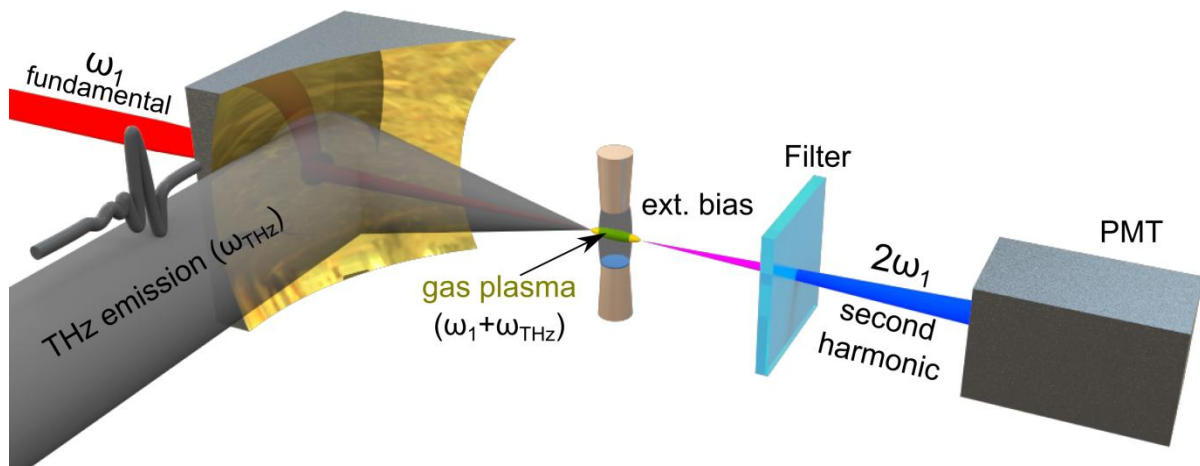


Figure 1.6: Illustration of air-biased-coherent-detection. The second harmonic wave ($2\omega_1$) is generated by mixing two fundamental (ω_1) photons with a single THz photon (ω_{THz}). After the generation of second harmonic wave it propagates together with the fundamental wave through a 400 nm bandpass filter, before reaching photomultiplier tube (PMT).

The air-biased-coherent-detection is an amazing detection scheme, which allows the detection of ultrabroadband (1 - 200 THz) THz pulses. There are a few factors that can limit the bandwidth detected by ABCD. The time duration of the fundamental pulse will influence the time resolution of THz pulse and therefore will set the limit of highest possible detectible frequency. A minimal difference in phase matching of fundamental pulse and THz pulse in air will also reduce the detectible bandwidth.

For narrow bandwidth (0.2 - 5 THz) the ABCD might not be the optimal solution. The external bias field is generated by applying a very high voltage on the electrodes, on the order of few kV and can be fatal if not handled with high care. Alternatively the detection by electro-optic sampling is easier to handle and provides higher signal to noise ratio when compared with ABCD, though the detectible bandwidth is limited to approximately 0.2 – 6 THz. The electro-optic sampling method is described in chapter 1.4.2.

1.3.3 ABCD THz-TDS system located at DTU Terahertz laboratory

The terahertz time domain spectroscopy system with air-biased-coherent-detection (ABCD THz-TDS) at DTU Terahertz laboratory is run by a Ti:sapphire amplifier system from Spectra-Physics Spitfire, shown in Fig. 1.7.

Chapter 1

Terahertz time domain spectroscopy



Figure 1.7: The Ti:sapphire amplifier system from Spectra-Physics Spitfire.

The Spitfire Pro Ti:sapphire amplifier system consist of four main parts, Millennia pump, Empower pump, Tsunami oscillator and Spitfire amplifier. The Spitfire amplifier receives approximately several nJ femtosecond pulses from Tsunami oscillator. The nJ femtosecond pulses are first stretched to nanosecond duration and then amplified to approximately 3.5 mJ by multiple passes through the gain medium, which is at optical resonance [42] and pumped by Empower pump (20 W, 527nm, 1kHz). Thereafter the 3.5 mJ nanosecond pulses are compressed to approximately 35 femtosecond. The Spitfire Pro Ti:sapphire amplifier system can also be modified to generate high power 100 femtosecond pulses, by changing two gratings both for stretching and compressing. Time and frequency domain of THz pulses generated by the four-wave mixing method in laser induced air plasma, with both 35 and 100 femtosecond pulses are shown in Fig. 1.8.

Chapter 1 Terahertz time domain spectroscopy

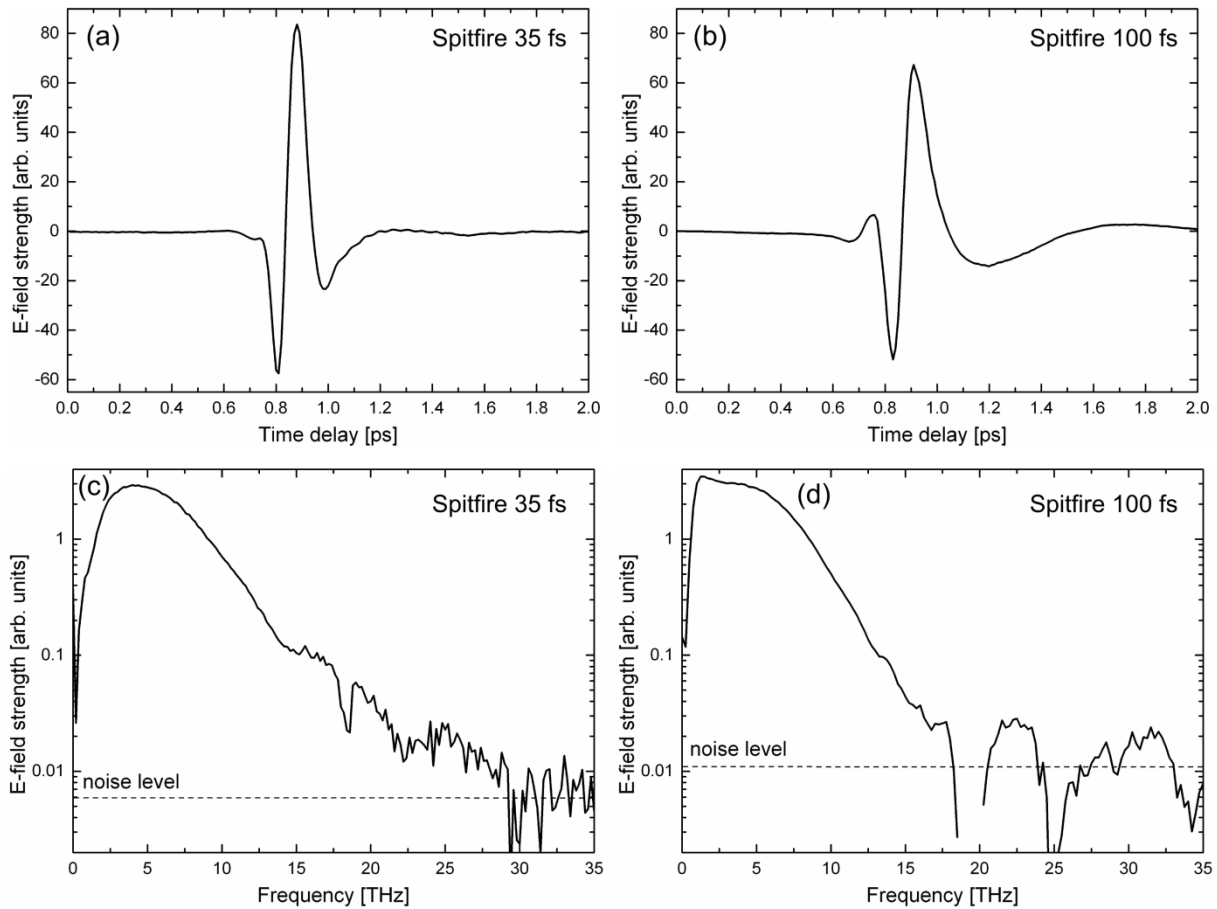


Figure 1.8: THz pulses generated by four-wave rectification method in laser induced air plasma using 35 fs and 100 fs optical pulses. (a) time and (c) frequency spectra of THz pulse generated by 35 fs optical pulse. (b) time and (d) frequency spectra of THz pulse generated by 100 fs optical pulse. ((c, d) log y-scale)

Figure 1.8 illustrates the difference between two THz pulses when generated by either 35 or 100 femtosecond optical pulses. Both measurements were performed in transmission configuration. Comparing both THz pulses in time domain (Fig. 1.8a,b) it is notable that the THz pulse generated by shorter optical pulse (35 fs) exhibit a narrower time pulse profile, when compared with THz pulses generated by 100 femtosecond optical pulse. The shorter THz pulse in time domain will encode a broader frequency spectra range (Fig. 1.8c,d), due to the nature of Fourier transform. This behavior is explained by the fact that the shorter optical pulse contains larger range of frequency content and therefore it is possible through difference-frequency generation to produce a THz pulse with broader bandwidth. When a 35 femtosecond optical pulse is used, it is possible to generate ultrabroadband THz pulse with bandwidth up to approximately 30 THz (Fig. 1.8c). The phonon from high resistivity silicon

Chapter 1 Terahertz time domain spectroscopy

wafer which is placed after the laser induced gas plasma (used as a pass filter for THz pulses) is clearly seen at approximately 18.4 THz (Fig. 1.8c) [43]. Switching the optical pulse to 100 femtosecond evidently reduces the bandwidth to approximately 15 THz (Fig. 1.8d).

We have shown the possibility of generating ultrabroadband THz pulses with a frequency range span between 0.2 THz and 30 THz by four-wave mixing method in laser induced air plasma using 35 femtosecond pulses. It is evident that the four-wave mixing method provides THz pulses with a bandwidth much broader than what is possible with photoconductive switches (Fig 1.3). A bandwidth up to 30 THz is not the limit of what one can achieve by four-wave mixing method, though as in 2010 H. G. Roskos and his group reported generation of THz pulses with four-wave rectification method with a remarkable bandwidth exceeding 100 THz [44]. The main parameters to achieve such a performance from four-wave rectification method were to use a shorter optical pulse (20 femtoseconds) and optimizing the geometry of BBO crystal. Besides the right cut at 32° of BBO crystal and the distance to the gas plasma, it have been also shown that the right tilt (8.1° horizontal, 2.3° vertical) of BBO crystal plays a significant role when optimizing the temporal overlap of fundamental and second harmonic in the gas plasma. Recently in 2012 E. Matsubara *et al.* achieved a THz pulse with a bandwidth up to 200 THz using air plasma, by applying even shorter optical pulse (10 femtoseconds) [45].

The four-wave mixing method in laser induced air plasma is an effective and pronounced method for generation of ultrabroadband THz pulses and one can do spectroscopy investigation covering a spectral range from far to near infrared (0.2 – 200 THz) with a single pulse. The maximum electrical field strength is of such THz pulses is in the order of several to tens of kV/cm. For THz pulses with higher electrical fields (order of several hundreds of kV/cm) it is necessary to use other generation methods. Generation of high power THz pulses in lithium niobate crystal, described in the following section, has shown to be a great method to achieve THz pulses with electrical field strength exciding MV/cm.

1.4 Terahertz pulse generation in LiNbO₃ crystal and electro optical detection

1.4.1 Generation in lithium niobate crystal

Another method to generate THz pulses is by nonlinear interaction of femtosecond laser pulses with second-order nonlinear medium. When an optical pulse propagates through a nonlinear electro-optic crystal, a low frequency polarization is stimulated which follows the intensity envelope of the optical pulse. This process is known as optical rectification (OR) and had been experimentally shown in 1962 using potassium dihydrogen phosphate as the nonlinear medium [46]. OR is a second-order nonlinear process and is based on difference frequency generation of the optical pulse. The nonlinear polarization P_{NL} induced by the OR can be written as [47]

$$P_{NL}(\Omega) = \varepsilon_0 \chi^{(2)} \int_0^\infty E(\Omega + \omega) E^*(\omega) d\omega, \quad (1.6)$$

where ε_0 is the permittivity of free space, $E(\omega)$ is the electrical field of the pump pulse, Ω is the THz frequency and $\chi^{(2)}$ is the nonlinear second-order susceptibility of the medium. As can be seen from equation (1.6), a narrowband pump pulse will generate low THz frequencies, while a broadband pump pulse can generate a broadband THz pulse. This nature of OR has been experimentally observed for THz pulses generated by laser induced gas plasma. The phase matching between the pump pulse and generated THz pulse have a great impact on the overall efficiency of OR process. The buildup of the THz radiation over macroscopic distances in the nonlinear medium is influenced by the dispersion of the medium. Therefore the efficiency of OR is highest when group velocity of optical pump pulse $v_g(\omega)$ and phase velocity of the generated THz radiation $v(\Omega)$ are matched

$$v(\Omega) = v_g(\omega_0). \quad (1.7)$$

Chapter 1
Terahertz time domain spectroscopy

In 1983 D. H. Auston have described the possibility to generate subpicosecond waves in electro-optic medium by focusing a femtosecond optical pulse [48]. The nonlinear polarization (Eq. (1.6)) of the dipole moment has a time variation which is governed by the rapidly rising and falling envelope of the optical pulse, and therefore the generated wave has a wide frequency spectrum extending from DC into the far infrared. Due to infrared lattice vibrations in electro-optic medium (e.g. lithium niobate (LiNbO_3)) the phase velocity of the generated THz radiation $v(\Omega)$ will be lower than the group velocity of optical pump pulse $v_g(\omega)$. Therefore the low frequency waves will emit in Cherenkov-like cone shape as shown in Fig. 1.9.

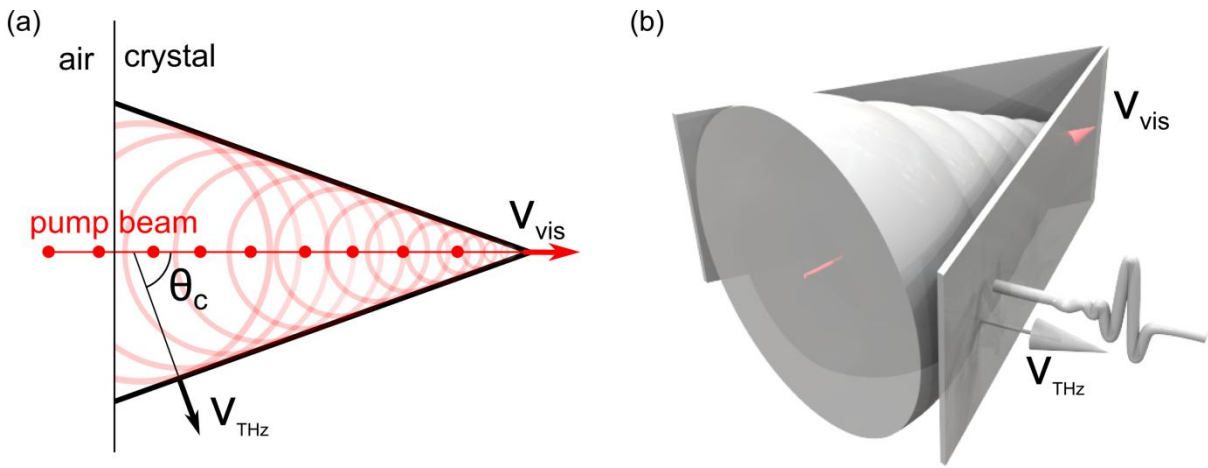


Figure 1.9: Cherenkov-like cone of emitted THz wave generated by OR in electro-optic crystal. (a) phase velocity of the generated THz radiation v_{THz} (thick black line) is lower than the group velocity of optical pump pulse v_{vis} . θ_c is the direction angle of emitted THz radiation. (b) spatial visualization of THz radiation generation by Cherenkov configuration in electro-optic crystal.

As shown in Fig. 1.9 direction of emitted THz pulse is described by the angle θ_c . Due to high dispersion in some electro-optic crystals such as in LiNbO_3 and lithium tantalite (LiTaO_3), where the refractive index in the terahertz range $n(\Omega)$ is more than two times larger than in the visible $n(\omega)$, it is necessary to include the emitted angle θ_c when satisfying the phase matched condition

$$v(\Omega) = \cos(\theta_c) v_g(\omega). \quad (1.8)$$

Chapter 1 Terahertz time domain spectroscopy

The projection of group velocity of optical pump pulse $v_g(\omega)$ in the propagation direction of the generated THz wave is $\cos(\theta_c)v_g(\omega)$.

In 1984 D. H. Auston et. al. experimentally showed the realization of generation of subpicosecond pulse by OR in LiTaO₃. By focusing 100 femtosecond pulses into LiTaO₃ it was possible to generate subpicosecond single-cycle pulses with amplitude of 10 V/cm. To obtain the time domain profile of subpicosecond pulse, the probe beam was delayed in time by varying its path length.

Though the generation of THz wave in Cherenkov-like cone matter by OR in electro-optic crystal is a great method to achieve THz pulses, there are two main drawbacks. The Cherenkov configuration (Fig. 1.9a) applies a tightly focused laser beam, which does not allow the use of high power pump pulses due to the risk of crystal damage. In addition the Cherenkov radiation generated at a given time will not interact with the radiation generated later. Both of the above mention issues were solved in 2002 when János Hebling *et al.* proposed a tilted pulse front configuration [49], that enabled the rapid development of high power THz pulse systems. The tilted pulse front configuration is shown in Fig. 1.1.

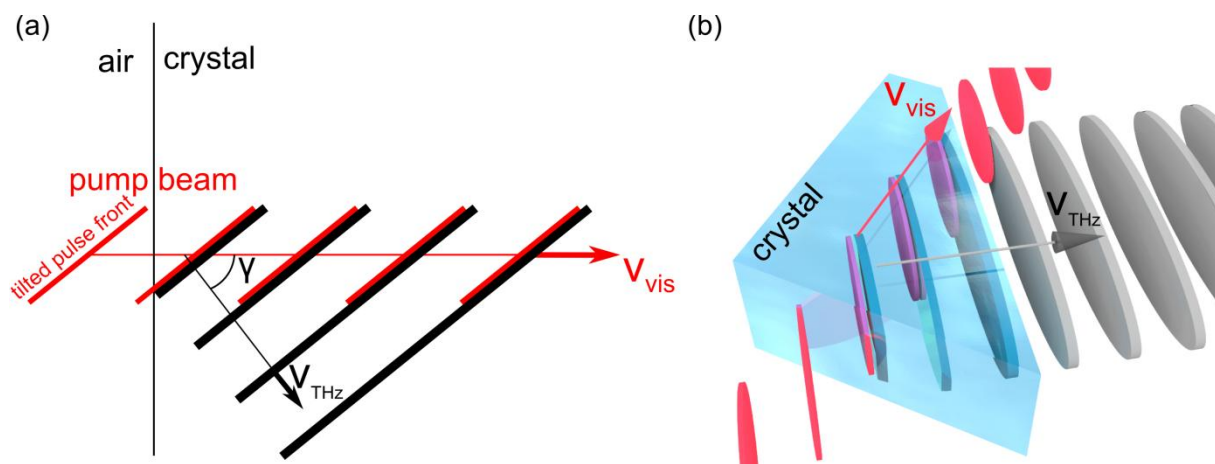


Figure 1.10: The tilted pulse front configuration. (a) the tilted pulse front of pump pulse (thick red line) enters the electro-optic crystal and generates the THz phase front (thick black line) with phase velocity v_{THz} . The direction of THz pulse is described by the angle γ . (b) spatial visualization of THz radiation generation by tilted pulse front configuration in electro-optic crystal.

One of the main advantages of tilted pulse front configuration shown in Fig. 1.1 is that it has no limit on the optical pump cross-section. By extending the cross-section one can use

extreme high power optical pulses without damaging the nonlinear crystal. Additionally the THz photons generated by tilted pulse front created at different times will interact with each other in the electro-optic crystal and result in higher conversion efficiency [49]. As for Cherenkov configuration the matching condition can be described by Eq. (1.8), where angles γ and θ_c are equal. In cases where $n_g(\omega) \leq n(\Omega)$ or consistently $v_g(\omega) \leq v(\Omega)$ in nonlinear crystal, which is the case for LiNbO₃ and LiTaO₃, a pulse front tilt angle γ can be found to fulfill the matching condition.

János Hebling *et al.* experimentally proved the concept of tilted pulse front by using gallium phosphide (GaP) as the nonlinear material [49]. The implementation of widely used nonlinear crystal, namely LiNbO₃, for THz pulse generation quickly followed. A year after in 2003 A. G. Stepanov *et al.* achieved 30 pJ THz pulses, with a conversion efficiency of 1.3×10^{-5} in LiNbO₃ at room temperature, while when cooling LiNbO₃ down to 77 K the conversion efficiency was increased to 4.3×10^{-5} (THz pulse energy 98 pJ) [50]. Following it has been reported that a tilt angle of 62° is optimal for highest conversion efficiency in LiNbO₃ and conversion efficiency can be additionally increased by reducing Mg (used to prevent photorefractive damage) doping concentration [51]. A few years later in 2007 K.-L. Yeh *et al.* reported generation of 10 μ J THz pulses with peak electrical signal of 250 kV/cm in a 0.6 % Mg doped LiNbO₃, using a 20 mJ pump pulse with a cross-section of 6 mm in diameter [52]. Recently an independent group has reported THz pulse energy of 125 μ J at room temperature [53] and 1.2 mJ with impressive conversion efficiency of approximately 3.4 % (at 150 K) [54].

1.4.2 Detection by electro-optical sampling

Another widely used detection scheme is called electro-optic (EO) sampling, which measures the electrical THz field in the time domain. EO sampling was first demonstrated in 1995-1996 by three independent groups, X.-C. Zhang's group [55], T. F. Heinz's group [56] and the group of P. U. Jepsen and M. Helm [57].

Chapter 1
Terahertz time domain spectroscopy

Fundamentally the free-space EO sampling utilizes Pockels effect in nonlinear crystal. The nature of Pockels effect is closely related to optical rectification process (Eq. (1.6)). The second-order nonlinear polarizations induced by Pockels effect is defined as

$$P_i^{(2)}(\omega) = \sum_j \varepsilon_0 \chi_{ij}^{(2)}(\omega) E_j(\omega), \quad (1.9)$$

where ε_0 is the permittivity of free space, $E_j(\omega)$ is the electrical field of the pump pulse and $\chi_{ij}^{(2)}$ is the field induced susceptibility tensor ($\chi_{ij}^{(2)}(\omega) = 2 \sum_k \chi_{ijk}^{(2)}(\omega, \omega, 0) E_k(0)$) [58]. As shown in Eq. (1.9) the electric field-induced birefringence in the nonlinear crystal is proportional to the amplitude of the applied field. Therefore it is possible to determine the THz field strength by directly measuring the field-induced birefringence. By implementing a delay stage it is possible to obtain the electrical field profile of THz pulse in time domain. The schematic illustration and optical image of free-space EO sampling is shown in Fig. 1.11.

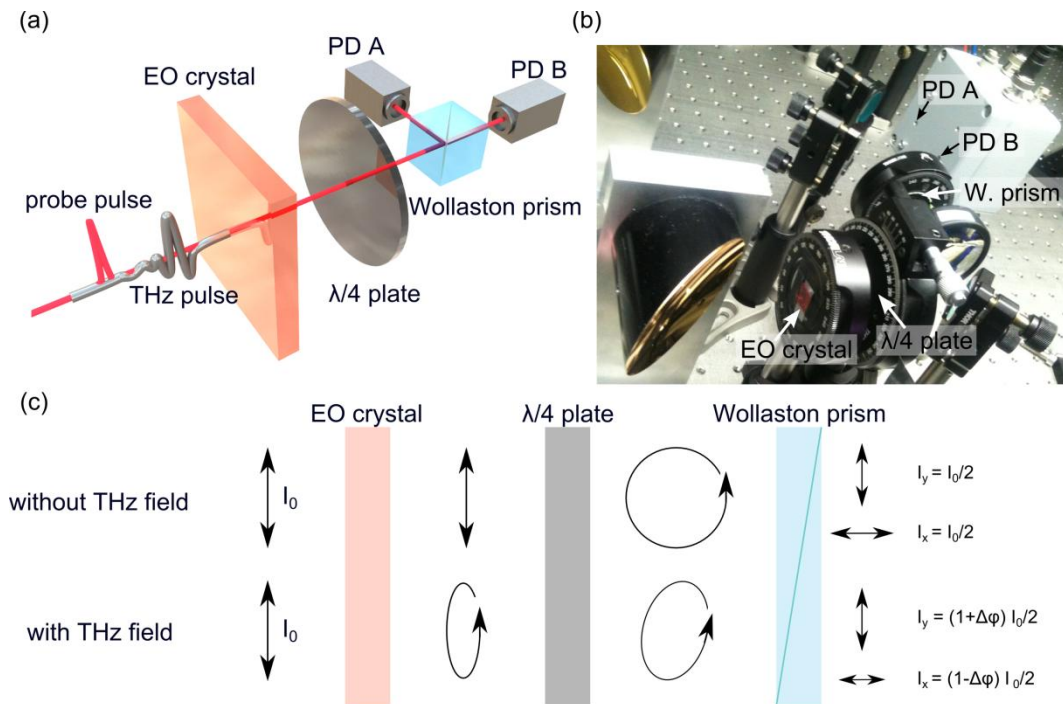


Figure 1.11: The free-space electro-optic (EO) sampling configuration. (a) schematic illustration of EO sampling configuration. (b) optical image of EO sampling setup at DTU Terahertz laboratory. (c) schematic diagram of the probe beam propagating through the optical components in EO sampling, (PD) photo detector, ($\Delta\phi$) differential phase retardation.

Chapter 1
Terahertz time domain spectroscopy

Figure 1.11a schematically illustrates the free-space EO sampling and Fig. 1.11b shows the real EO sampling setup at DTU Terahertz laboratory. The EO sampling consists of four main elements; EO crystal, $\lambda/4$ plate, Wollaston prism and a set of photodiodes. As illustrated in Fig. 1.11c in the absence of the THz field, the linearly polarized probe beam will propagate through the EO crystal unaffected, and will maintain the linear polarization after exiting the EO crystal. Passing through the $\lambda/4$ plate the linear polarized probe pulse will become circularly polarized. The circularly polarized probe beam will then pass through the Wollaston prism where it will be equally separated into two components, $I_y = I_x = I_0 / 2$, where I_0 is the initial intensity of the probe beam. The two components of the probe beam will as a final point be guided into two balanced photodiodes (PD A and PD B). Whereas in the presence of the THz pulse, the THz field-induced birefringence in EO crystal will produce a probe pulse with slightly elliptical polarization. When passing the $\lambda/4$ plate, the probe pulse will become elliptical polarized and after propagating through the Wollaston prism it will be separated into two uneven components ($I_y = (1 + \Delta\varphi) \cdot I_0 / 2$, $I_x = (1 - \Delta\varphi) \cdot I_0 / 2$), where $\Delta\varphi$ is the differential phase retardation induced by birefringence. The lock-in amplifier which is connected to two balanced photodiodes will record the amplitude of THz field strength by subtraction of the two components of the probe pulse, $I_{THz} = I_y - I_x$. The recorded signal by lock-in amplifier is directly proportional to the electric field of the THz pulse. The lock-in amplifier is locked to the optical chopper which modulates the THz beam with 500 Hz. In absence of THz pulse the two components of the probe beam are equal and therefore the signal recorded with lock-in amplifier will be zero. The differential phase retardation $\Delta\varphi$ of the probe beam when propagating through the EO crystal due to the Pockels effect can be written as [58]

$$\Delta\varphi = \frac{\omega L}{c} n_0^3 r_{41} E_{THz}, \quad (1.10)$$

where c is the speed of light, L is the propagation distance, r_{41} is the electro-optic coefficient, n_0 is the refractive index at the probe frequency and E_{THz} is the electrical field amplitude of THz pulse. The recorded THz field amplitude by balanced photodiodes can now be written as

Chapter 1 Terahertz time domain spectroscopy

$$I_s = I_y - I_x = I_0 \cdot \Delta\varphi = \frac{I_0 \omega L}{c} n_0^3 r_{41} E_{THz}, \quad (1.11)$$

which evidently shows that the recorded signal by EO sampling configuration is proportional to the electric field of the THz pulse, E_{THz} .

In an ideal case, the optical group velocity and THz phase velocity would be perfectly matched in the EO crystal, thus the probe pulse will experience a constant electric field of the THz pulse while propagating in the EO crystal. This is not the case for widely used EO crystal such as e.g. ZnTe ($n_g = 3.22$ at 835 nm [59] and 3.18 at 1 THz [22], [60]) and GaP ($n_g = 3.56$ at 835 nm [59] and approx. 3.7 at 1 THz [61]), which limits spectral resolution of THz pulses by EO sampling. Several other factors contribute to the limitation of spectral resolution. The duration of probe pulse and dispersion of nonlinear susceptibility will also influence the spectral resolution. Additionally the spectral bandwidth is limited by absorption of EO crystals in the THz region. The dominant THz absorption processes in EO crystals are the transverse-optical phonon resonances, which are located in the range span from approximately 5 to 10 THz [58]. Even though there are several limitation factors to be considered when choosing EO sampling as the detection mechanism, it is still a widely used configuration, especially for detection of narrowband high-power THz pulses.

1.4.3 Lithium niobate THz-TDS system located at DTU Terahertz laboratory

The lithium niobate (LiNbO_3) THz-TDS system at DTU Terahertz laboratory is run by a Ti:sapphire amplifier system from Spectra-Physics Spitfire described in chapter 1.3.3. The schematic illustration of the LiNbO_3 THz-TDS system is shown in Fig. 1.12.

Chapter 1
Terahertz time domain spectroscopy

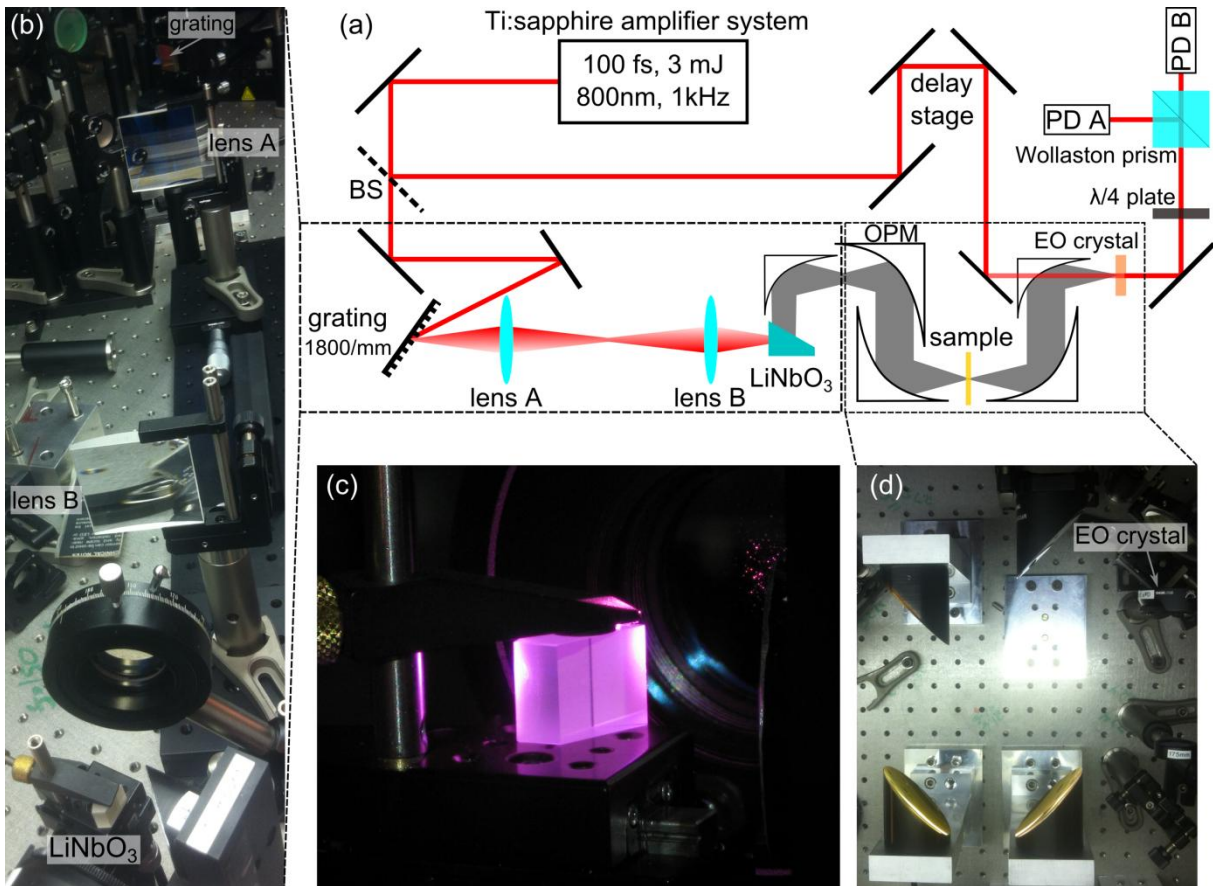


Figure 1.12: The LiNbO₃ THz-TDS setup. (a) Schematic illustration of LiNbO₃ THz-TDS setup. (BS) beam splitter, (PD) photodiode, (OPM) optical parabolic mirror, (EO) electro-optic. (b) optical image of generation path for tilted pulse front configuration including grating, lenses and LiNbO₃ crystal. (c) LiNbO₃ crystal exposed to femtosecond pulses (100 fs, 3.0 mJ, 800 nm). (d) optical path of THz pulses, including multiple parabolic mirrors.

As illustrated in Fig. 1.12a the tilted pulse front configuration is performed by a 1800/mm grating and focused on LiNbO₃ by a set of two cylindrical lenses (Fig. 1.12b). The two lens configuration has been inspired by previous work by H. Hirori et al. [62]. The LiNbO₃ crystal is cut at 62° to satisfy the optimal conditions for tilted pulse front configuration. The THz pulse generated in LiNbO₃ crystal (Fig. 1.12c) is collected by a 1 inch optical parabolic mirror (OPM) and thereafter passes through a set of four OPMs, with a sample spot (focus) between second and third OPM (Fig. 1.12d). The THz pulse is detected by electro-optical sampling technique, where both GaP and ZnTe crystals have been used as EO medium. The THz pulse generated by LiNbO₃ THz-TDS system is shown in Fig. 1.13, both in time and frequency domain.

Chapter 1

Terahertz time domain spectroscopy

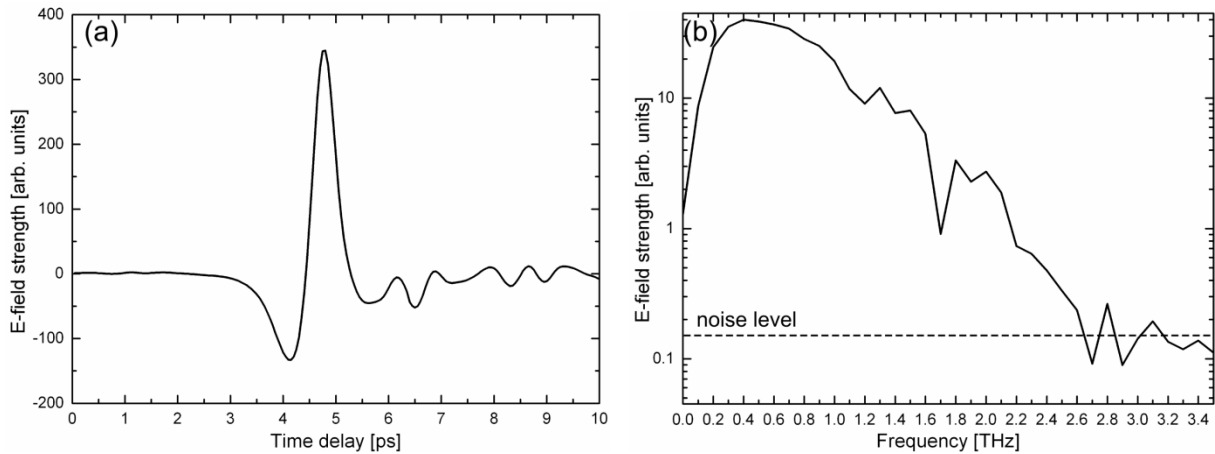


Figure 1.13: THz pulse generated by a LiNbO_3 THz-TDS system. (a) time and (b) frequency domain.

As seen in Fig. 1.13 the high-power THz pulse generated by LiNbO_3 THz-TDS system exhibits FWHM of approximately 0.6 picoseconds and has a frequency range span from 0.2 to 2.5 THz. Since the time domain waveform of THz pulse is achieved by a mechanical delay stage implemented for the probe beam it requires approximately 1-2 minutes to record a single THz pulse. THz pulse with the maximum electrical field of approximately 400 kV/cm has been measured at the sample position and been used for Kerr measurements of chalcogenide glasses described in section 2.4.

1.5 Conclusion

Table 1.1 summarizes the main parameters of different THz-TDS systems described in this chapter and used during this project.

THz TDS system	PC	ABCD	LiNbO ₃
Generation method	PC switch	FWMP in laser induced two-color air plasma	Optical rectification in LiNbO ₃ crystal with TPF configuration
Detection method	PC switch	ABCD	EO sampling
Optical source	Ti:sapphire fs laser	Ti:sapphire amplifier system	Ti:sapphire amplifier system
Bandwidth	0.1 – 2.0 THz	0.2 – 30 THz	0.2 – 2.5 THz
Electrical maximum field strength	several V/cm	50-100 kV/cm	400 kV/cm
Scan rate	100 pulses / sec	1 pulse / 5 min	1 pulse / 2 min

Table 1.1: Main parameters of three different THz-TDS systems. (FWMP) four-wave mixing process, (ABCD) air-biased-coherent-detection, (TPF) tilted pulse front, (EO) electro-optic.

Every THz-TDS system has their pros and cons. While THz-TDS system based on PC switches have an incredible scan rate of 100 pulses / sec and are easy to operate, it has very low electrical field strength and narrow bandwidth, which limits its usage for broadband spectroscopy and investigation of nonlinear response of materials. For broadband spectroscopy measurements ABCD THz-TDS is preferred. For nonlinear investigation of THz-radiation/matter interaction the LiNbO₃ THz-TDS is used with electrical maximum field strength of approximately 400 kV/cm.

During this project the THz-TDS system based on PC switches have been used to characterize behavior of metamaterials (chapter 4) and perform linear spectroscopy measurements of chalcogenide glasses (section 2.2). To achieve ultrabroadband linear spectroscopy measurements of chalcogenide glasses (section 2.3) ABCD THz-TDS system have been used. LiNbO₃ THz-TDS have been utilized to determine the nonlinear behavior of chalcogenide glasses (section 2.4) and investigate the field enhancement properties of THz antennas (chapter 3).

2 Chapter

Chalcogenide glasses

2.1 Introduction to chalcogenide glasses

Chalcogenide glasses, first reported six decades ago [63], have attracted significant attention in recent years due to their unique properties, such as high refractive index, mid-infrared transparency, and very high third-order (Kerr) nonlinearity [64]. Furthermore their large nonlinearities in the optical, near- and mid-infrared regions have made them promising candidates for fast nonlinear optical devices [65]. Additionally the As_2S_3 and As_2Se_3 glasses have become a widely used material for many optical applications due to its flexibility towards micro- and nano-fabrication processes. Several groups working with chalcogenide glasses have shown that one can pattern As_2S_3 by means of nano-imprint lithography [66], etching [67] and direct laser writing [68].

2.2 Narrowband terahertz time domain spectroscopy investigation of linear properties of As_2S_3 and GaLaS.

In this chapter we describe the linear behavior of chalcogenide glasses (ChGs) As_2S_3 and 70% Ga_2S_3 /30% La_2S_3 (GaLaS), represented by the refractive index and absorption coefficient, at low terahertz frequencies (0.2 THz to 2.5 THz). Where As_2S_3 is a widely used glass, the GaLaS compound on the other hand, is not so exploited yet. It is a material which shows high stability and resistance to mechanical and chemical wear thus making it an interesting material to be used for devices operating in harsh environments.

At lower frequencies, ranging from 0.2 THz to 2.5 THz, we employ a terahertz time domain spectroscopy (THz-TDS) system as illustrated in Fig. 2.1 a. The THz radiation is generated by femtosecond excitation of a low temperature grown GaAs photoconductive switch (Menlo Systems) with 800 nm wavelength pulses from a femtosecond oscillator (Femto-Lasers Fusion Pro300). The detection of the terahertz pulses is performed by photoconductive

Chapter 2 Chalcogenide glasses

sampling in a similar antenna, gated by the same Ti:sapphire laser. The photocurrent is recorded with a lock-in amplifier locked to the frequency (13.2 kHz) of the modulation of the bias voltage on the THz emitter as function of the delay time and used to obtain the representation of the THz electric field. See section 1.2 for more details on THz-TDS based on photoconductive switches.

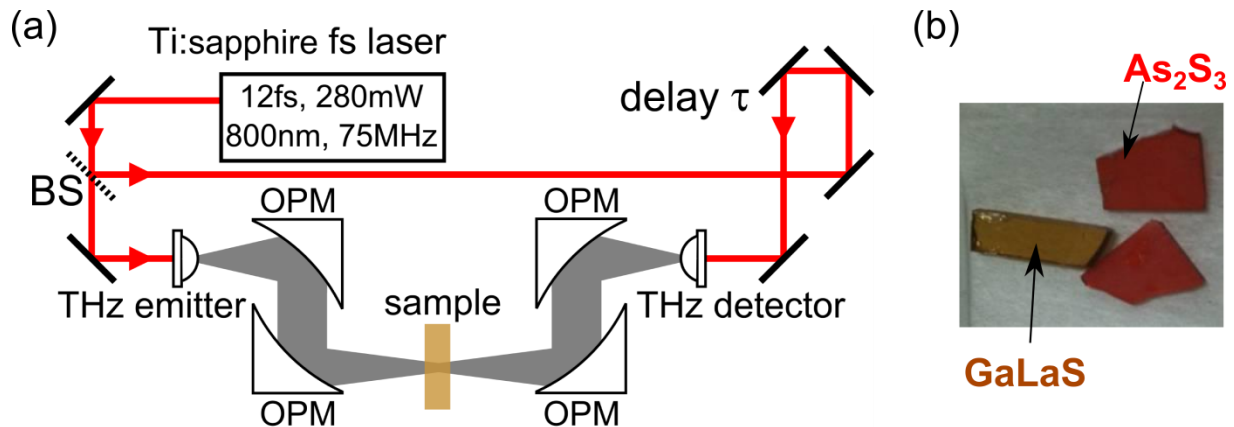


Figure 2.1: (a) The terahertz pulse is emitted by a photoconductive switch, which is able to generate terahertz radiation in a range of 0.2-2.5 THz. (b) Bulk As_2S_3 and GaLaS samples. OPM: off-axis parabolic mirror, BS: beam splitter.

Bulk samples of As_2S_3 and GaLaS with thicknesses of 0.85 mm and 1.40 mm respectively (see Fig 2.1b) were used to determine the optical parameters for a frequency span between 0.2 THz and 2.5 THz. The bulk samples were measured only at low frequencies because there were too absorptive for the broadband characterization with the broadband THz-TDS system.

Figure 2.2 display refractive index and absorption coefficient of bulk 0.85 mm thick As_2S_3 sample.

Chapter 2 Chalcogenide glasses

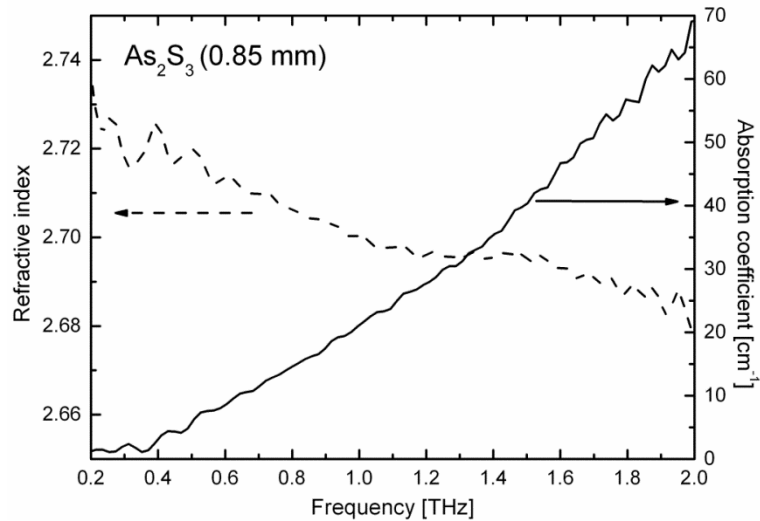


Figure 2.2: Refractive index (dashed line) and absorption coefficient (solid line) for bulk (0.85 mm) As_2S_3 sample.

As shown in Fig. 2.2 the refractive index of As_2S_3 for frequency span between 0.2 THz and 2.0 THz is situated between 2.69 and 2.73, while the absorption monotonously increases reaching 70 cm^{-1} at 2.0 THz. Similar values of As_2S_3 's optical parameters for frequency range from 0.5 THz to 2.0 THz were reported by Parrot *et al.* [69].

THz-TDS revealed huge values of absorption coefficient of GaLaS sample, reaching approximately 50 cm^{-1} for 0.8 THz. Consequently the 1.40 mm thick bulk GaLaS sample was totally opaque for frequencies higher than 0.8 THz. Therefore it was necessary to deposit a thinner sample. This was achieved by depositing $3.6 \mu\text{m}$ GaLaS on top of high resistivity silicon (HR Si) wafer. Optical parameters for bulk and thin film GaLaS samples are shown in Fig. 2.3.

Chapter 2 Chalcogenide glasses

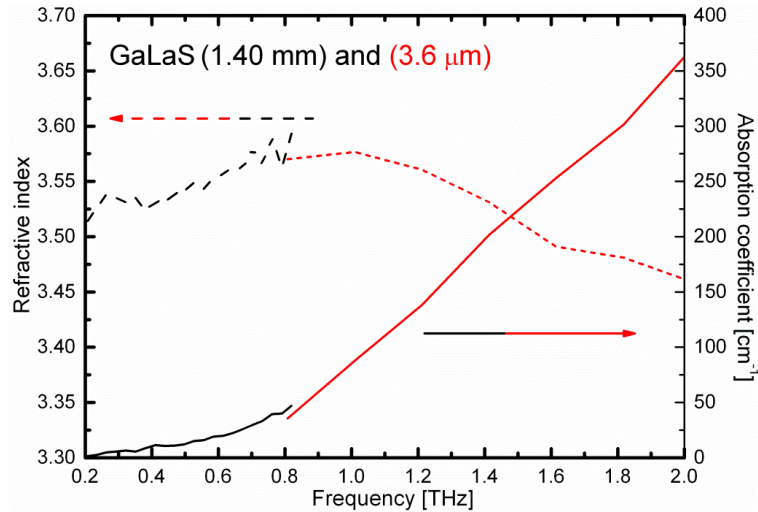


Figure 2.3: Refractive index (dashed line) and absorption coefficient (solid line) for bulk 1.40 mm thick (black curves) and thin film 3.6 μm (red curves) GaLaS samples.

THz-TDS have revealed huge refractive index of GaLaS sample, reaching approximately 3.55 at 1 THz. At the same time GaLaS sample exhibits much higher absorption than As_2S_3 . Absorption coefficient of GaLaS sample is approximately 360 cm^{-1} at 2 THz, whereas it is only 70 cm^{-1} for As_2S_3 at the same frequency.

2.3 Broadband terahertz time domain spectroscopy investigation of linear properties of As_2S_3 and GaLaS.

For the broadband (2–18 THz) spectroscopic analysis, it was necessary to fabricate thin samples of As_2S_3 and GaLaS due to high absorption coefficient of both glasses. This was achieved by thermal deposition of As_2S_3 and GaLaS on top of 528 μm thick high resistivity silicon (HR Si) wafer pieces with resistivity of 10000 Ωcm .

The As_2S_3 glasses were prepared by conventional melt-quenching techniques using arsenic and sulphur elements of high purity. The obtained bulk material was crumbled and put into a tantalum boat. The films were obtained by thermal evaporation technique in a vacuum of 5×10^{-6} Torr. The electric current which heats the tantalum evaporator was adjusted to obtain film deposition rate of 2.5–3.0 nm/s.

Chapter 2 Chalcogenide glasses

Lanthanum based glasses of composition 70% Ga_2S_3 and 30% La_2S_3 was prepared by a specially developed technique. The mixture of appropriate powdered components Ga_2S_3 and La_2S_3 is placed in a carbon glass crucible. The crucible is heated by RF induction at a frequency of 120 kHz. At high temperatures the melt becomes a conductor which contributes to material convection. Melting is done in a medium purged by argon gas. Thin films are obtained from the 70% Ga_2S_3 , 30% La_2S_3 vitreous target using pulse laser deposition in vacuum 2×10^{-6} Torr. The target is irradiated by 200 mJ / 10 ns pulses of the excimer laser with 248 nm wavelength. The silicon substrate is placed during ablation in an oven at a temperature of 100 °C, at a distance of 55 mm from the target.

One half of the HR Si piece was covered with glass, whereas the uncovered area was used for the reference measurement. Three samples with different thicknesses were prepared for each glass: 13.6 μm , 6.9 μm and 3.2 μm for As_2S_3 and 3.6 μm , 2.3 μm and 1.3 μm for GaLaS. The geometry and optical image of deposited samples are shown in Fig. 2.4.

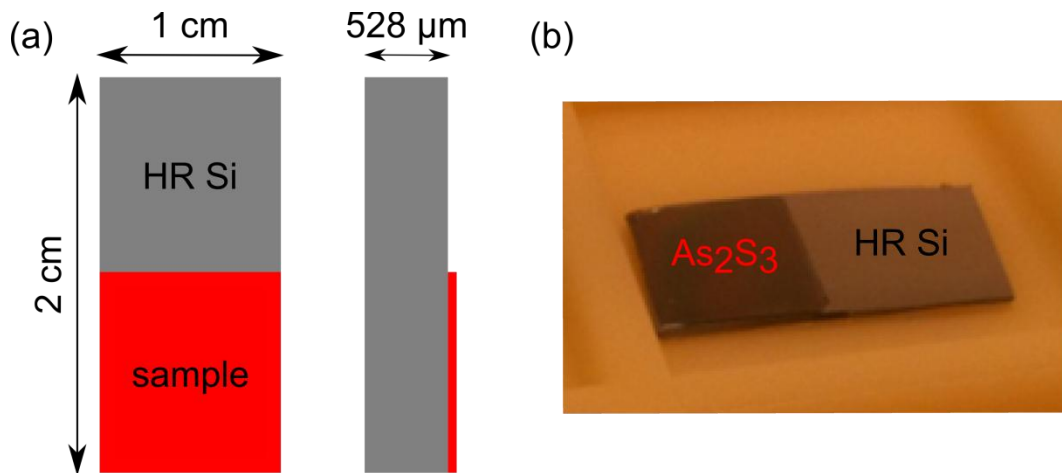


Figure 2.4: (a) Sketch of thin film sample deposited on HR Si 1 x 2 cm piece. (b) Optical image of As_2S_3 deposited on HR Si.

The broadband THz-TDS (ABCD THz-TDS) system ranging from 2 THz to 18 THz are generated by laser induced air plasma and detected in an air biased coherent detection (ABCD) setup. To generate gas plasma a laser pulse (frequency ω) of 35 fs, 800 nm, 1.5 mJ with a repetition rate of 1 kHz and its second harmonic (2ω), generated in a 100 μm thick β -barium borate (BBO) crystal, are focused collinearly by an off-axis paraboloidal mirror in a N_2 purged chamber. In the ABCD THz-TDS setup the THz field is detected by monitoring the THz-field-

induced second harmonic (2ω) of the 800 nm probe beam, focused in the detection region to intensity slightly below the plasma generation threshold. An AC bias field is applied to the interaction region to supply an optical bias to the second-harmonic generation, thus allowing field-resolved detection of the THz transient as function of the delay time. A schematic illustration of the ABCD THz-TDS setup is shown in Fig. 2.5. See section 1.3 for more details on ABCD THz-TDS setup.

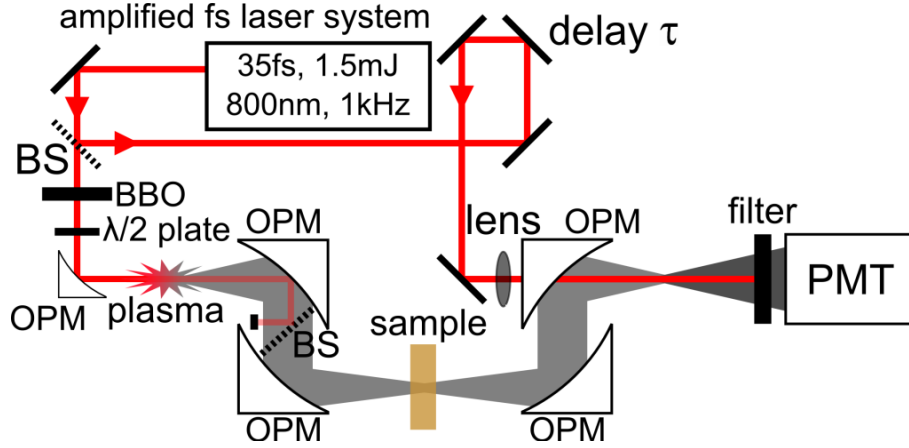


Figure 2.5: ABCD THz-TDS setup. OPM: off-axis parabolic mirror, BS: beam splitter, BBO: β -barium borate crystal, PMT: photomultiplier tube.

To extract material parameters from such thin glass samples one must take into account the Fabry-Pérot (FP) etalon effect inside the glass layer. We follow the extraction procedure described by Duvillaret et al. [70]. The complex refractive indices $\tilde{n} = n - i\kappa$ for the thin glass samples deposited on HR Si substrate is retrieved by inverting the amplitude transmission coefficient $\tilde{T}(\omega)$ expression

$$\tilde{T}(\omega) = \frac{\tilde{E}_{sam}(\omega)}{\tilde{E}_{ref}(\omega)} = \frac{2\tilde{n}(n_{Si} + n_{air})}{(\tilde{n} + n_{Si})(\tilde{n} + n_{air})} \cdot \exp\left(-i(\tilde{n} - n_{air})\frac{\omega \cdot d}{c}\right) \cdot \tilde{FP},$$

$$\tilde{FP} = \frac{1}{1 - \frac{(\tilde{n} - n_{Si})(\tilde{n} - n_{air})}{(\tilde{n} + n_{Si})(\tilde{n} + n_{air})} \cdot \exp\left(-2i\tilde{n}\frac{\omega \cdot d}{c}\right)}. \quad (2.1)$$

In Eq. (1.2) n_{Si} and n_{air} are refractive indices of HR Si wafer and air respectively, d is the thickness of the ChGs, c is the speed of light in vacuum and ω is the angular frequency. The thin film samples were characterized by both THz-TDS and ABCD THz-TDS systems in transmission configuration.

Chapter 2 Chalcogenide glasses

Figure 2.6 shows terahertz pulses after transmission through the reference and through the 13.6 μm thick As_2S_3 sample recorded in the ABCD THz-TDS setup.

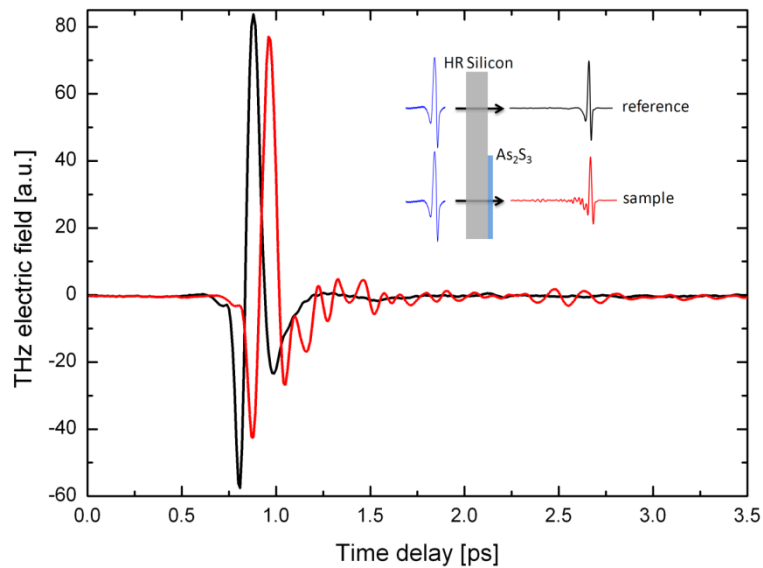


Figure 2.6: Measured terahertz pulses with ABCD THz-TDS system. Both reference (HR Si, black curve) and sample (HR Si with 13.6 μm As_2S_3 , red curve) are shown.

As seen in Fig. 2.6 the terahertz pulse that propagates through the sample has lower amplitude and is delayed with respect to the reference pulse. Significant ringing is observed on the trailing edge of the pulse propagating through the thin film of As_2S_3 , indicative of a resonant response of the sample. The lower amplitude is due to absorption in the As_2S_3 , while the additional delay is due to the longer optical path in As_2S_3 when compared with air. The amplitude spectra in the frequency domain (see Fig. 2.7) are then obtained by Fourier transformation of the time-domain data.

Chapter 2 Chalcogenide glasses

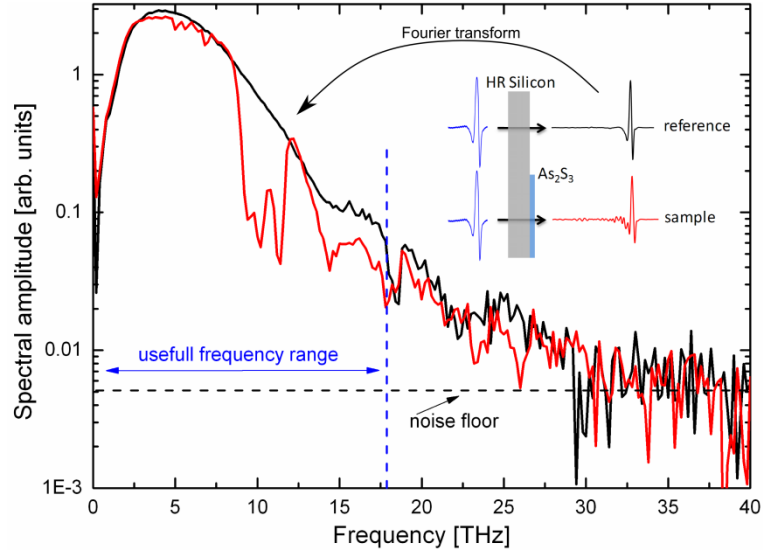


Figure 2.7: The amplitude spectra in the frequency domain obtained from the Fourier transformation of terahertz pulses in time domain shown in Fig. 2.6.

From frequency spectra presented in Fig. 2.7 it is easy to observe the absorption bands located around 7 and 10 THz. Even though the THz transients generated by air plasma in ABCD THz-TDS system contain frequency contents up to approximately 30 THz, we have chosen to extract the optical parameters of ChGs for the frequency up to 18 THz, due to the low signal to noise ratio for higher frequencies.

The ratio between the spectra recorded for the sample and reference $\tilde{E}_{sam}(\omega)/\tilde{E}_{ref}(\omega)$ is then used to determine the amplitude transmission coefficient $\tilde{T}(\omega)$. Knowing the transmission coefficient $\tilde{T}(\omega)$ the complex refractive index $\tilde{n} = n - i\kappa$ can be extracted, where the absorption coefficient $\alpha(\omega)$ is related to the imaginary part of the refractive index by $\alpha(\omega) = 2\omega\kappa/c$. The refractive index and absorption coefficient of As_2S_3 are shown in Fig. 2.8.

Chapter 2 Chalcogenide glasses

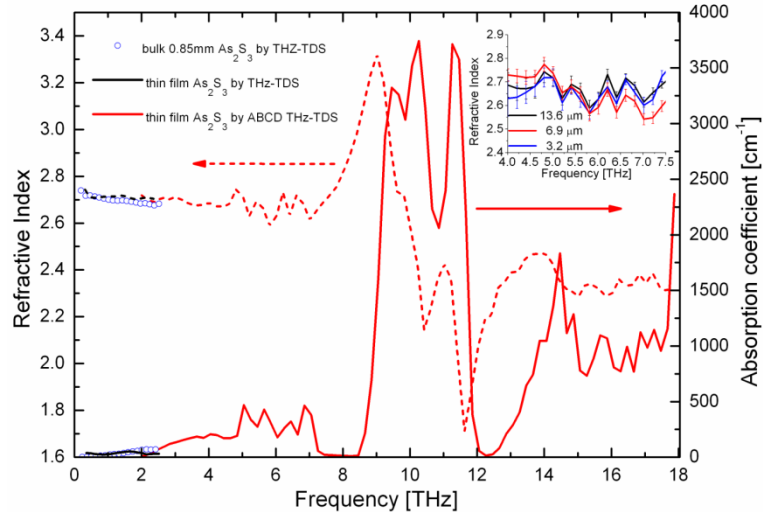


Figure 2.8: Refractive index (dashed line) and absorption coefficient (solid line) of As_2S_3 . The spectroscopy results by THz-TDS system on thin film samples (black) and on a 0.85 mm thick sample (blue circles). The higher frequencies are measured by ABCD THz-TDS system (red) for 13.6 μm thick sample. Upper right corner: Transition from relaxational dynamics to localized vibrational dynamics is shown for three different thicknesses (13.6, 6.9, and 3.2 μm). Error bars represent standard deviation based on three measurement sets.

The THz spectrum of As_2S_3 reveals several important features. At lower frequencies ranging from 0.2 THz to 4 THz monotonous decrease of the refractive index from 2.74 to 2.67 occurs. Such anomalous dispersion for the As_2S_3 glass (though with slightly higher values from approximately 2.83 to 2.78) in the frequency range from 0.5 THz to 2 THz were also reported by Parrott *et al.* [69]. The absorption coefficient increases monotonously from 1.2 cm^{-1} to 200 cm^{-1} in the same frequency range. The absorption in this region is expected to follow a universal scaling behavior [71], characterized by a power-law frequency dependence of the absorption coefficient. The universality of such a scaling law is, however, limited to frequencies below a point which sometimes is called the Ioffe-Regel transition [72]. The Ioffe-Regel transition occurs when the mean free path between scattering events of acoustic plane waves propagating in the material approaches the wavelength of the plane wave. At wavelengths longer than this length, scattering will be the dominant loss factor and result in a universal behavior of the absorption coefficient. At shorter wavelengths, plane-wave propagation dominates. Here we directly observe this transition from disorder-induced loss to a collective response mediated by medium- and long-range order of the glass. At intermediate frequencies, ranging from 4.5 to 7 THz, the As_2S_3 refractive index displays four pronounced resonances with refractive indices oscillating between 2.6 and 2.7. These dispersion resonances are constant with respect to

Chapter 2 Chalcogenide glasses

positions and amplitudes for samples with different thicknesses, as shown in the inset of Fig. 2.8. The vibrational modes in this frequency range have also been observed by others [73], [74], [75]. X-ray-absorption spectroscopy and Raman scattering study of As_2S_3 glass have revealed the existence of local order in form of As_4S_4 monomers and pyramidally coordinated $\text{As}(\text{S}_{1/2})_3$ units from As_2S_3 clusters [74], [76]. It has been previously reported that thermal vapor deposited As_2S_3 to contain a large fraction As_4S_4 molecular clusters [73]. Cluster models of As_4S_4 monomers and pyramidally coordinated $\text{As}(\text{S}_{1/2})_3$ units from As_2S_3 clusters are shown in Fig. 2.9.

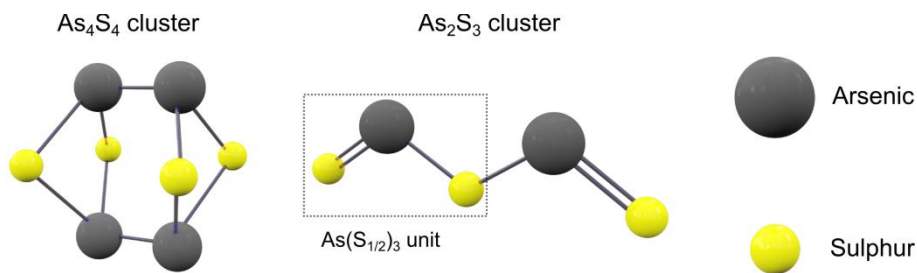


Figure 2.9: Structure of arsenic sulfide clusters, As_4S_4 and As_2S_3 .

The four vibrational modes that are observed at this frequency range are caused by S-As-S bending modes in As_4S_4 monomers [74], [75]. At still higher frequencies the refractive index dispersion exhibits three very strong resonances. The refractive index first increases to 3.3 at 9 THz, then abruptly drops to 1.7 at 11.6 THz, and finally settles at a value near 2.2 above 14 THz. Associated with the strong dispersion are three very strong absorption peaks in the region 8.5-12 THz with the highest absorption coefficient increasing up to $>3700 \text{ cm}^{-1}$. These resonances are local vibrational modes, specifically As-S stretching modes [75] in both As_4S_4 monomers and pyramidally coordinated $\text{As}(\text{S}_{1/2})_3$ units.

The very strong resonances are sandwiched between two transparency windows at 7.2-8.5 THz and 12-13 THz, where the absorption coefficient is measured to be as low as 10 cm^{-1} . This observation indicates that transmission windows exist in As_2S_3 , with a bandwidth of several hundred GHz. This, in combination with the high third-order nonlinearity that have been measured in As_2S_3 (see following section) in the material, opens up the possibility of compact devices for all-optical processing of ultrahigh-bandwidth signals encoded on THz waves near 8 and 12 THz. We observe good quantitative agreement between the spectra obtained with the two experimental setups on the various As_2S_3 samples (see Fig. 2.8.).

Chapter 2 Chalcogenide glasses

The broadband measurement of GaLaS samples has revealed a very high refractive index at low frequencies, as shown in Fig. 2.10.

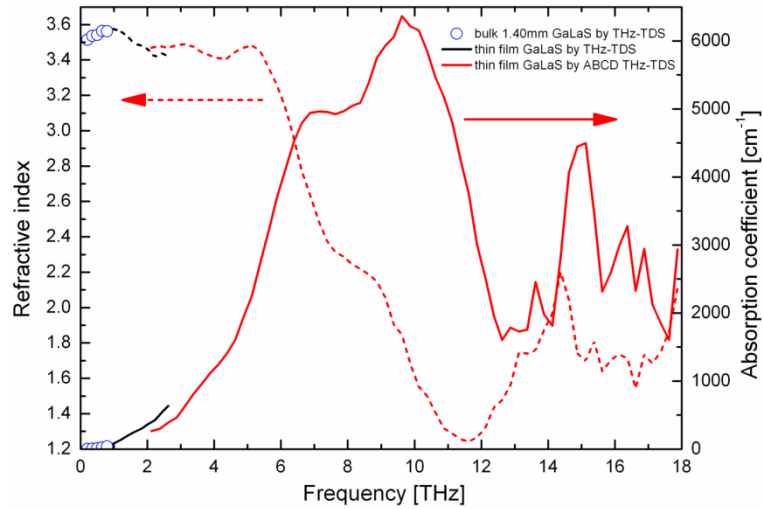


Figure 2.10: Refractive index (dashed line) and absorption coefficient (solid line) of GaLaS. The spectroscopy results by THz-TDS system on thin film samples (black) and on a 1.45 mm thick bulk sample (blue circles). The higher frequencies are measured by ABCD THz-TDS system (red) for 3.6 μm thick sample.

A refractive index in the range $n \approx 3.5 - 3.6$ is measured at frequencies from 0.2 to 5 THz. For higher frequencies the refractive index decreases dramatically, reaching a minimum value of approximately 1.25 at 11.5 THz and settles at a value of 1.7-1.8 at the highest measured frequencies. Following the dispersion trends, GaLaS experiences a very strong absorption band, reaching its maximum of $>6300 \text{ cm}^{-1}$ at 9.8 THz. The lowest absorption coefficient reaches approximately 1700 cm^{-1} at 13 THz. Again good matching between the spectra recorded with the two experimental setups on various samples is observed.

2.4 Kerr effect in As_2S_3 and As_2Se_3 glasses

We have performed high power THz spectroscopy investigation by LiNbO_3 THz-TDS system on two bulk chalcogenide glass samples, namely As_2S_3 and As_2Se_3 . Both samples are known for their very high third-order nonlinear coefficients at optical frequency ($n_{2,nir} = 2.5 \cdot 10^{-14} \text{ cm}^2/\text{W}$ cm^2/W for As_2S_3 and $n_{2,nir} = 11.4 \cdot 10^{-14} \text{ cm}^2/\text{W}$ cm^2/W for As_2Se_3) [64]. Furthermore in 2009 Matthias C. Hoffmann *et. al.* reported that the THz-induced third-order nonlinear coefficients of liquid solutions (CS_2 Benzene, CCl_4 , CHCl_3 and CH_2I_2) were generally on the same order of

Chapter 2 Chalcogenide glasses

magnitude as at optical frequencies [77]. Those results indicated that there was a good change, that we could observe THz-induced Kerr effect in our amorphous solid samples (As_2S_3 and As_2Se_3).

To perform investigation of nonlinear response in As_2S_3 and As_2Se_3 we slightly modified the LiNbO_3 THz-TDS system described in section 1.4.3. We utilized a similar configuration that was reported by Matthias C. Hoffmann *et. al.*, where the sample was placed in the main focus point and thereafter the THz-induced birefringence was detected by electro-optical sampling scheme [77]. The modified LiNbO_3 THz-TDS system is shown in Fig. 2.11.

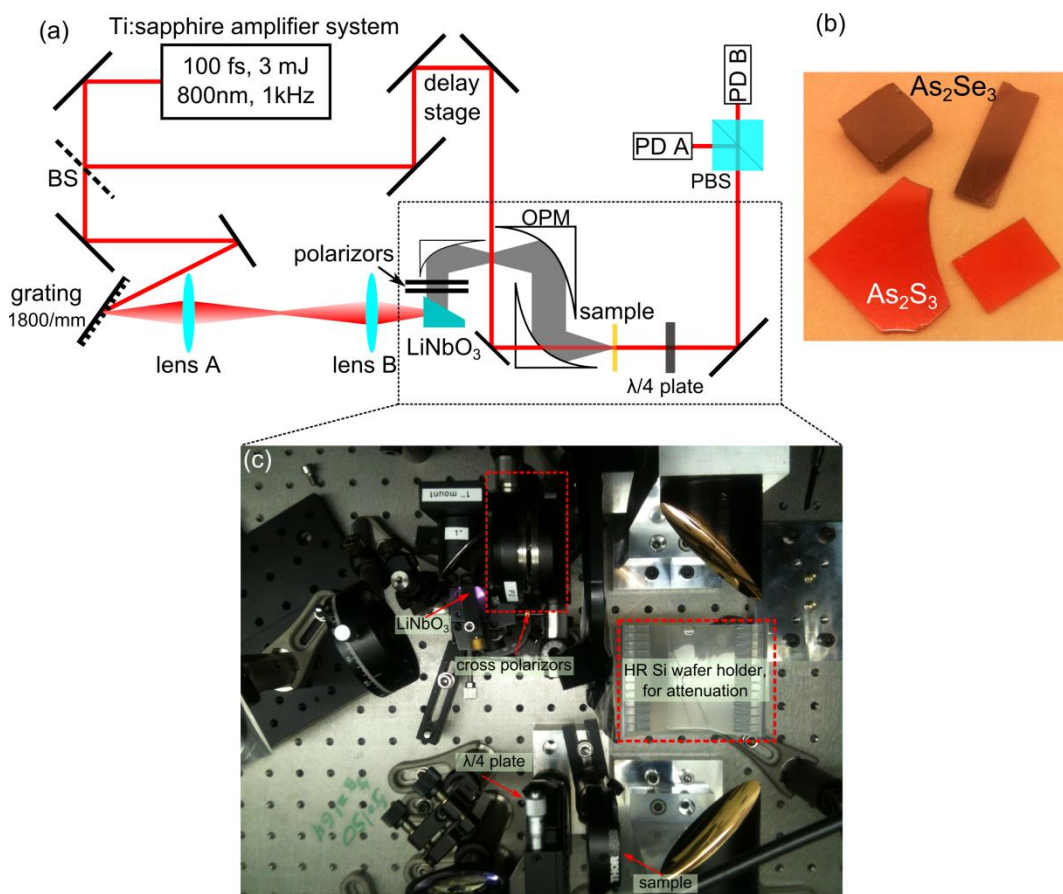


Figure 2.11: (a) Schematic illustration of modified LiNbO_3 THz-TDS system used for Kerr measurements. (b) Optical image of As_2S_3 and As_2Se_3 bulk glass samples. (c) Optical image of LiNbO_3 THz-TDS system showing the optical path of THz pulse, being generated in LiNbO_3 crystal and thereafter guided through two polarizers (used for attenuation of THz electrical field strength) and thereafter focused on the sample.

As illustrated in Fig. 2.11a the THz pulse was generated in LiNbO_3 crystal by tilted pulse front technique, described in section 1.4.1. The proper pulse front tilt was achieved with a

Chapter 2 Chalcogenide glasses

1800/mm grating and a set of optical parabolic lenses. The THz pulse is guided and focused on the sample by three parabolic mirrors. It is possible to attenuate THz radiation by a set of wire grid polarizers or by placing high resistivity wafers in the collimated path of THz pulse. The optical images of the bulk As_2S_3 and As_2Se_3 samples are shown in Fig. 2.11b. In order to determine the absolute field strength of the THz pulses and obtain a good spatial overlap of the THz pulse with the probe beam, the chalcogenide samples were replaced by an electro-optic gallium phosphide (GaP) crystal so that the temporal profile of the THz pulses could be measured by electro-optic sampling. The polarization configuration of probe beam with respect to THz pulse is shown in Fig. 2.12.

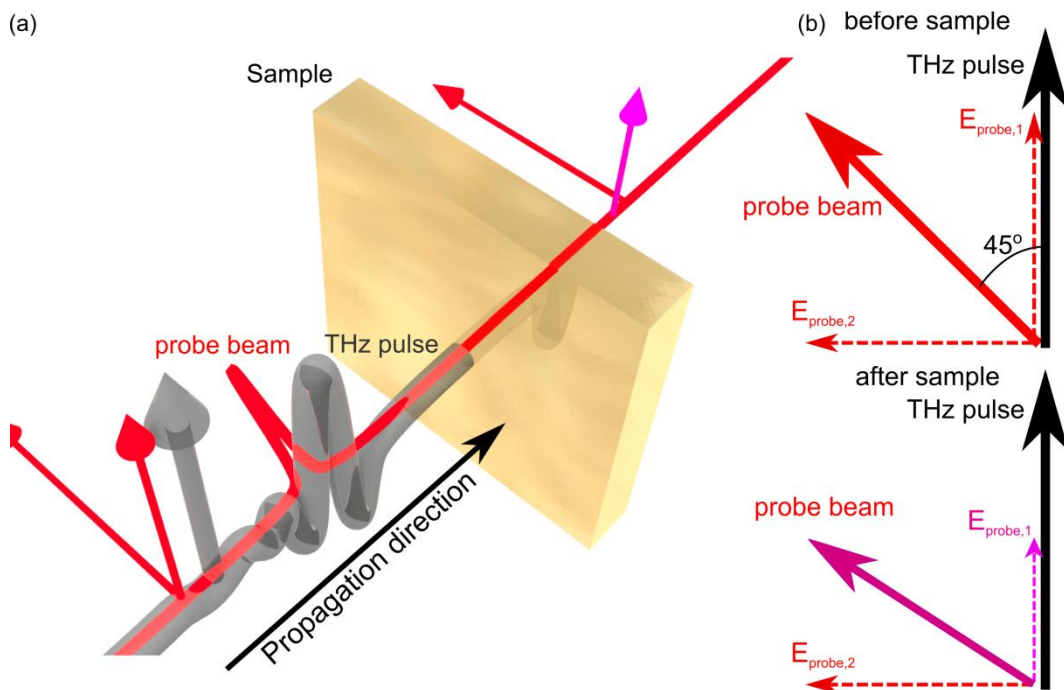


Figure 2.12: (a) Illustration of polarizations of probe and THz pulses before entering the sample, where the probe beam is polarized at an angle of 45° with respect to the THz pulse. (b) Showing the electric components of the probe beam (parallel ($E_{probe,1}$) and perpendicular ($E_{probe,2}$) to the THz pulse) before and after passing the sample.

As shown in Fig. 2.12a it is of high importance to spatially overlap the THz pulse together with the probe beam, to be able to measure the THz-induced changes in the sample. When the maximum THz signal is obtained (good spatial overlap between THz pulse and probe beam) and THz pulse in time-domain is recorded, then we are ready to exchange the GaP crystal back with the sample of interest. The alignment of generation and probe paths is kept unchanged during the Kerr characterization of the chalcogenide samples.

Chapter 2 Chalcogenide glasses

Before entering the probe beam is polarized at 45° with respect to the THz pulse and therefore it will equally split into parallel ($E_{probe,1}$) and perpendicular ($E_{probe,2}$) components as shown in Fig. 2.12b. The parallel component $E_{probe,1}$ will be influenced by the possible THz-induced birefringence, while $E_{probe,2}$ will propagate through the sample unaffected by the THz pulse. Resulting changes in components strengths are detected with a balanced photodiodes scheme (section 1.4.2).

The THz pulse generated in a LiNbO_3 crystal, and detected by a GaP crystal with electro-optical sampling configuration is shown in Fig. 2.13.

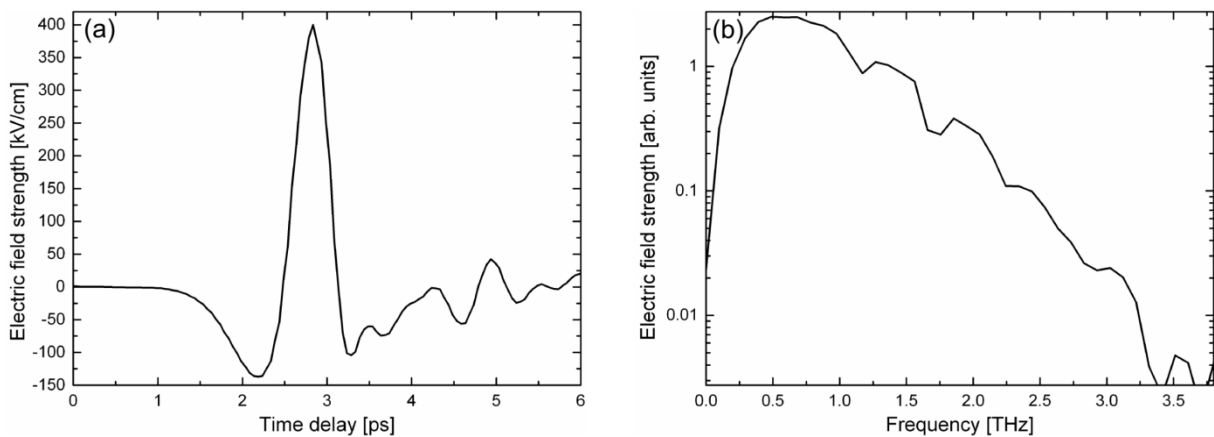


Figure 2.13: THz pulse generated by a LiNbO_3 crystal shown in (a) time and (b) frequency domain.

As shown in Fig. 2.13a it was possible to generate a THz pulse with a maximum electric field strength of 400 ± 10 kV/cm. The frequency content spans the 0.05 - 3 THz region, with 84% of the pulse energy concentrated within 0.2 - 1.0 THz (Fig. 2.13b).

After we successfully have recorded the THz pulse and determine its electrical strength, we exchanged the GaP crystal with a 0.716 mm thick As_2S_3 or 1.059 mm thick As_2Se_3 respectively. Recorded probe signals in As_2S_3 and As_2Se_3 at different THz field strength are presented Fig. 2.14.

Chapter 2 Chalcogenide glasses

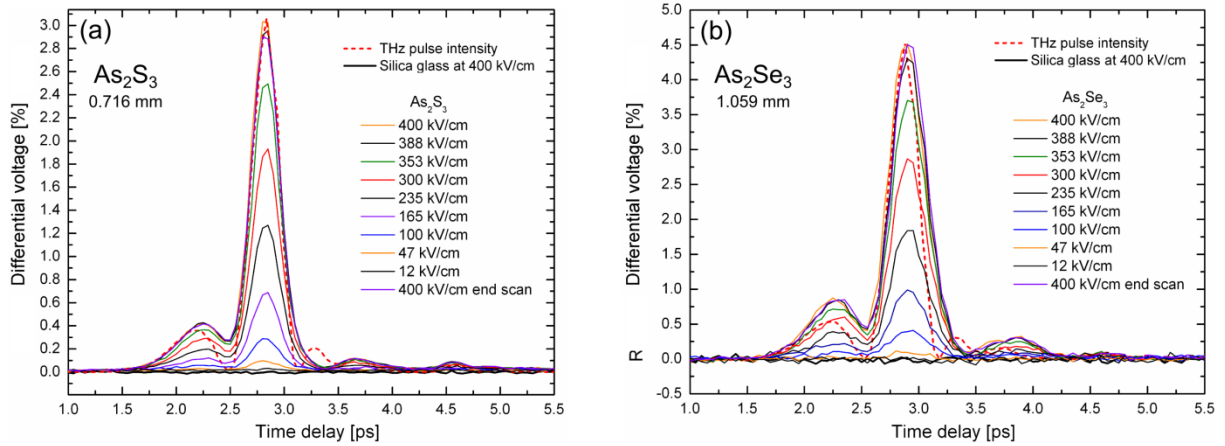


Figure 2.14: THz-induced birefringence in (a) As_2S_3 (0.716 mm) and (b) As_2Se_3 (1.059 mm) bulk samples. The electrical field intensity of THz pulse (dashed, red curve) normalized to the maximum signal is shown. Attenuation of THz pulse strength was achieved by cross polarizers (see Fig. 2.11.). 1 mm thick silica sample was measured with 400 kV/cm electric field strength for comparison (black curve).

The recorded probe signals in As_2S_3 and As_2Se_3 at varying THz field strengths are shown in Fig. 2.14. The field strength was attenuated by a pair of wire grid polarizers, placed immediately after the first paraboloidal mirror. For both samples the measurements at the highest field strength were performed twice, at the beginning and at the end of the measurement series to confirm repeatability of the measurements, and to confirm that the samples had not been damaged during the characterization. As expected the recorded signal increases with the THz pulse strength. At a field strength of 47 kV/cm, the THz-induced signal is barely noticeable but grows up at higher field strengths. The As_2Se_3 sample has revealed a larger THz-induced changes than As_2S_3 . This could have been foreseen since the third-order nonlinear coefficient of As_2Se_3 is significantly larger than that for As_2S_3 in optical range [64]. We used a 1 mm thick bulk silica glass sample as a reference. Even with the full field strength (400 kV/cm), no THz-induced birefringence was observed due to the very small third-order nonlinearity of silica compared to As_2S_3 and As_2Se_3 . Though this wasn't unexpected, since it was previously reported that the third order nonlinear response in silica is 260 times lower than in As_2S_3 and 1200 times lower than in As_2Se_3 [78].

For both chalcogenide glasses we observe that the temporal shape of the THz-induced Kerr signal closely follows the intensity profile of the THz pulse (dashed, red curve). This is indicative of a very fast nonlinear response of the two glasses, and is typical for nonresonant

Chapter 2 Chalcogenide glasses

excitation. There are no rotational dynamics of molecules in solid glasses in contrast to some liquid samples where the relaxation time can be rather long, for instance as long as 13 picoseconds for liquid CH_2I_2 [77]. As can be seen in Fig. 2.14 in the case of As_2S_3 the THz-induced signal instantly responds to the changes in the intensity profile of a THz pulse, as there is good phase matching between the THz wave and probe beam in the glass, while a minor delay is observed for As_2Se_3 .

The analysis of the peak values of the THz-induced signal in glasses has revealed a straight third-order nonlinear behavior, shown in Fig. 2.15.

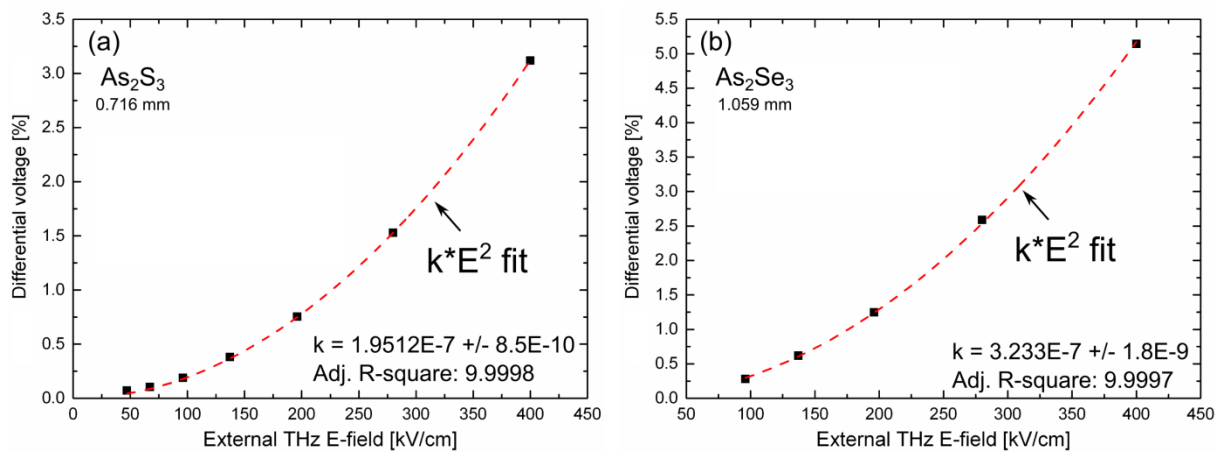


Figure 2.15: The peak values (squares) of THz-induced signal for (a) As_2S_3 and (b) As_2Se_3 . Quadratic fit $k \cdot E^2$ is shown (red dashed curve). Attenuation was performed by high-resistivity silicon wafers (see Fig. 2.11).

The analysis of the peak values of the THz-induced signal in glasses reveals a standard third-order nonlinear behavior, shown in Fig. 2.15. For the small values of the phase retardation observed here, the recorded values are accurately fitted by a quadratic fit $\Delta V / V_0 \approx \Delta \phi = k \cdot E^2$, where k is a constant and E is the electrical field strength. This demonstrates that the observed THz-induced signals in the chalcogenide samples are due to the Kerr effect ($\Delta n = \lambda K E^2$), where Δn is the change in the refractive index, λ is the wavelength and K is the Kerr constant. The nonlinear refractive index can be written as $n_2 = \Delta n / I$, where I is the intensity of the THz pulse averaged over the propagation length in the glass or the physical length of the sample.

Chapter 2 Chalcogenide glasses

As described in chapter 2.3 the chalcogenide glasses behave as an amorphous system at lower terahertz frequencies, which can be seen from the monotonies increase in the absorption coefficient, in absence of sharp fixtures. To verify that bulk samples are truly amorphous, we performed the Kerr measurements with the full electrical THz field strength at different orientation angles of the sample with full electrical THz field strength (400 kV/cm) at different rotation angle of the sample. The results are presented in Fig. 2.16.

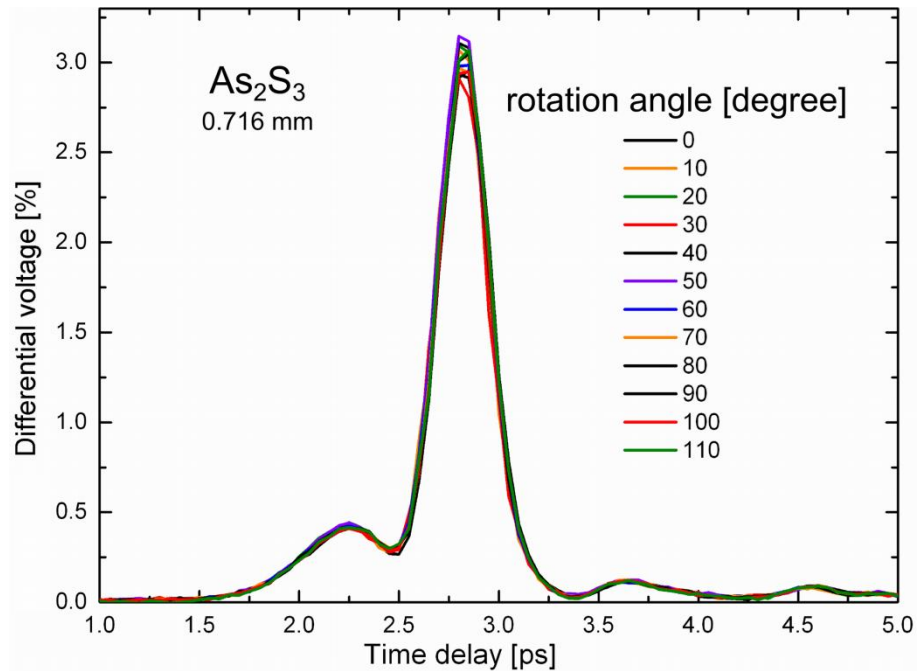


Figure 2.16: Kerr signal as a function of rotation angle of As₂S₃ with a maximum electric field strength of 400 kV/cm. Span range from 0° to 110° in steps of 10° was performed.

No change in the Kerr signal is observed when the As₂S₃ sample was rotated from 0° to 110° as shown in Fig. 2.16. This observation definitely concludes that our As₂S₃ bulk sample is truly amorphous. To determine the magnitude of the Kerr effect (Δn_2) we measured both the refractive index and absorption coefficient of chalcogenide glasses in the terahertz range by the Picometrix T-Ray 4000 THz-TDS system. Results for both samples are shown in Fig. 2.17.

Chapter 2 Chalcogenide glasses

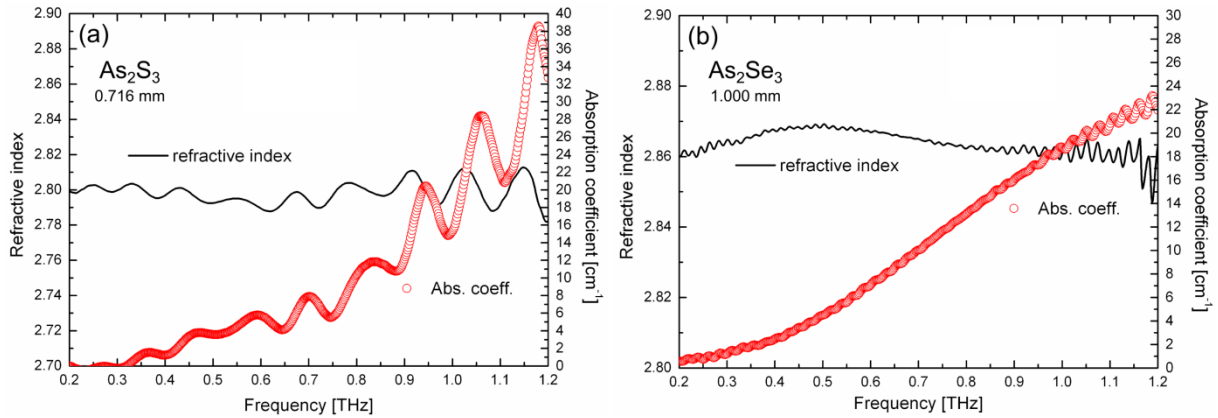


Figure 2.17: Refractive index (black curves) and absorption coefficient (red circles) for (a) As_2S_3 and (b) As_2Se_3 bulk samples, measured by THz-TDS (Picometrix T-Ray 4000) system.

The spectroscopy result shown in Fig. 2.17 displays nearly constant refractive indices for both glasses in the frequency range 0.2 THz - 1.0 THz (2.80 for As_2S_3 and 2.86 for As_2Se_3). A marginally higher As_2Se_3 refractive index can be explained by the higher density of As_2Se_3 (4.75 g/cm^3) when compared to As_2S_3 (3.42 g/cm^3). The absorption coefficient monotonously increases from nearly zero to approximately 20 cm^{-1} for both samples between 0.2 THz and 1.0 THz. This behavior is universal for a wide range of glasses, and confirms the amorphous nature of chalcogenide glasses at low THz frequencies [71], [79]. For further analysis we calculated the weighted average of the absorption coefficient over the pulse spectrum in the range 0.2 - 1.0 THz. This range contains 84 % of the total intensity of the THz pulse. Averaged absorption coefficients $\alpha = 6.2 \text{ cm}^{-1}$ and 10.8 cm^{-1} are found for As_2S_3 and As_2Se_3 respectively. The characteristic penetration depth of the THz field ($L_{abs} = 1/\alpha$) is thus 1.61 mm and 0.93 mm for As_2S_3 and As_2Se_3 , respectively. We use these values to calculate the local THz field inside the bulk sample taking absorption and Fresnel transmission coefficients into account.

The minor oscillations observed both in refractive index and absorption coefficient for As_2S_3 sample (see Fig. 2.17a) is linked to the fact that the THz pulse in time domain is not able to reach the noise level before the first echo from Fabry-Perot reflection in the sample arrives as shown in Fig. 2.18. The echoes from Fabry-Perot can be analytically treated, though in this case it is necessary to know the exact thickness of the sample.

Chapter 2
Chalcogenide glasses

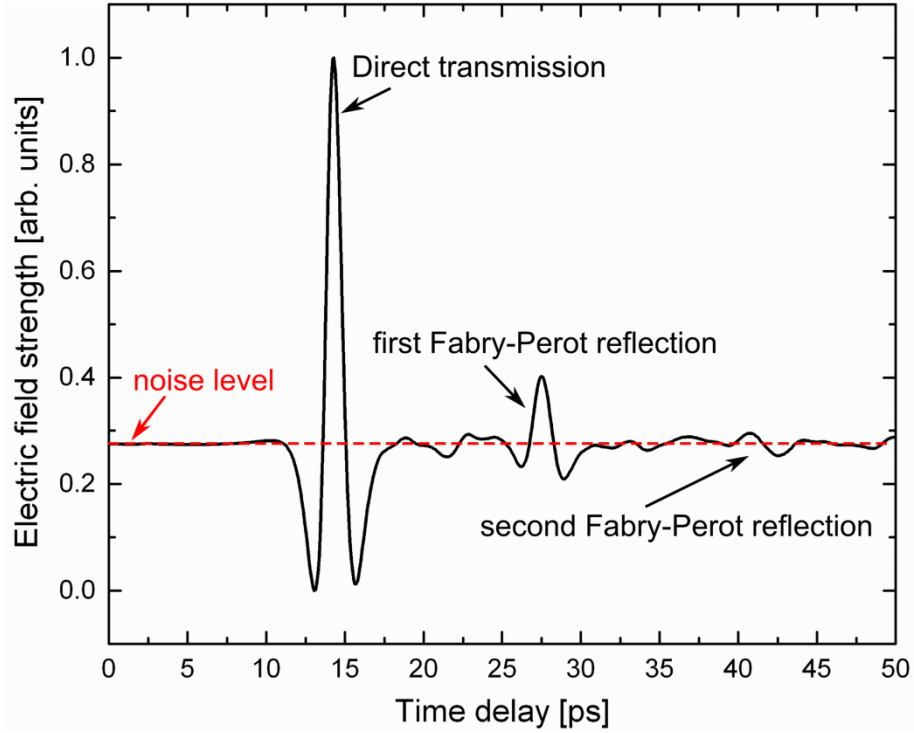


Figure 2.18: THz pulse in time domain recorded after passing a 0.716 mm thick As_2S_3 bulk sample. The first Fabry-Perot reflection is observed approximately 13.2 ps after the main pulse.

We determined the nonlinear refractive indices $n_2 = 1.746 \cdot 10^{-14} \text{ cm}^2/\text{W}$ and $n_2 = 3.440 \cdot 10^{-14} \text{ cm}^2/\text{W}$ for As_2S_3 and As_2Se_3 respectively, see Table 2.1

	As_2S_3	As_2Se_3
$\Delta n [10^{-6}]$	5.34	6.30
$n_2 [10^{-14} \text{ cm}^2/\text{W}]$	1.75 ± 0.09	3.44 ± 0.17
$\chi^{(3)} [10^{-20} \text{ m}^2/\text{V}^2]$	4.84 ± 0.24	9.96 ± 0.50
$I_{ave} [10^8 \text{ W}/\text{cm}^2]$	3.06 ± 0.15	1.83 ± 0.09

Table 2.1: THz-induced optical parameters of As_2S_3 and As_2Se_3 glasses. Δn modulation of the refractive index, n_2 nonlinear refractive index, $\chi^{(3)}$ nonlinear susceptibility ($\chi^{(3)} = \frac{4}{3} \cdot \epsilon_0 c \cdot n_0^2 n_2$, where n_0 is linear refractive index), I_{ave} averaged intensity through samples.

Chapter 2 Chalcogenide glasses

The measured nonlinear refractive index of As_2S_3 comparable with the values that have previously been reported by several groups at optical frequencies, while the nonlinear refractive index of As_2Se_3 is approximately 3-7 times lower than what has been measured at optical frequencies. Figure 2.19 compares our results with previously reported values of nonlinear refractive indices for As_2S_3 and As_2Se_3 measured at optical/near infrared range.

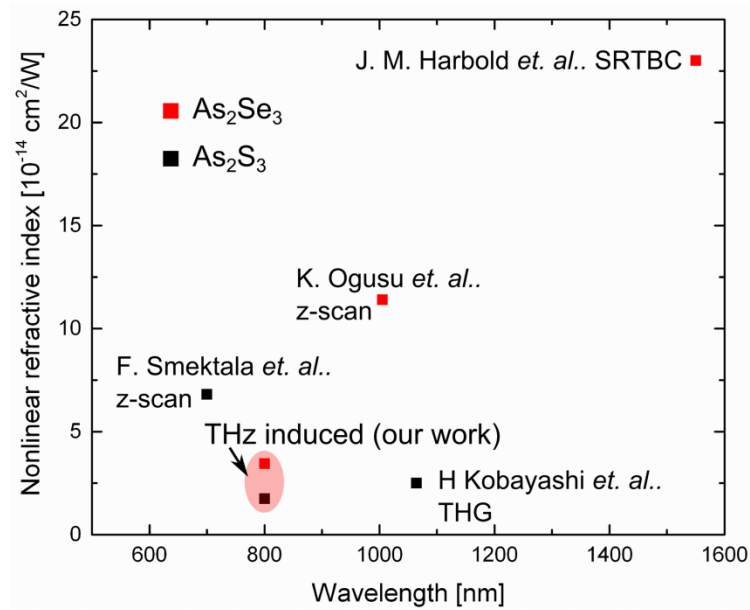


Figure 2.19: Nonlinear refractive index of As_2S_3 and As_2Se_3 . J. M. Harbold *et al.* [78], K. Ogusu *et al.* [80], F. Smektala *et al.* [81] and H. Kobayashi *et al.* [82]. (SRTBC) spectrally resolved two-beam coupling, (THG) third-harmonic generation.

2.5 Conclusion

In conclusion, we have measured the linear refractive index and absorption coefficient of As_2S_3 and GaLaS glasses in the broad frequency range extending from 0.2 to 18 THz. This broad band frequency range was covered by two different THz-TDS setups, and the measured spectra are well matched at the bordering spectral region between the frequency coverage of the two spectrometers. We observe that chalcogenide glasses possess highly complex dispersion profiles. In As_2S_3 we observe the Ioffe-Regel transition in the 4-5 THz region, followed by a rich vibrational behavior between 4.5-7 THz, indicative of medium-range order, and strong, phonon-like vibrational modes in the 8.5-12 THz, indicative of local order in the glass. In addition, two transparency windows have been identified in As_2S_3 at frequencies 7.2-8.5 and 12-13 THz. The spectroscopy of GaLaS has revealed a high refractive index of 3.5 at lower frequencies, whereas at frequencies higher than 5 THz the refractive index decreases reaching its minimum of 1.25 at 11.5 THz. The strong index variations are accompanied by a high absorption over the whole THz range.

Furthermore we have performed nonlinear investigation of two bulk chalcogenide glasses (As_2S_3 and As_2Se_3). We used high power THz-TDS setup, where THz pulse is generated in a LiNbO_3 crystal by a tilted pulse front technique. The generated THz pulses had a electrical field of 400 ± 10 kV/cm. By electro-optical sampling scheme we have measured a high Kerr response in both chalcogenide samples ($n_2 = 1.746 \cdot 10^{-14} \text{ cm}^2/\text{W}$ for As_2S_3 and $n_2 = 3.440 \cdot 10^{-14} \text{ cm}^2/\text{W}$ for As_2Se_3), whereas bulk silica glass sample haven't respond to the influence of THz pulse at full power. Additionally we have confirmed by a rotation scan that the As_2S_3 sample as expected is truly amorphous.

We believe that our observation of two transparency windows for As_2S_3 sample at frequencies 7.2-8.5 and 12-13 THz, together with our findings of existing THz-induced Kerr effect in As_2S_3 , will be of high importance when considering As_2S_3 for future applications in ultrafast nonlinear THz devices.

Chapter 2

Chalcogenide glasses

3 Chapter

Terahertz field enhancement

3.1 Introduction

Recently in 2009 the strong field enhancement of a THz wave impinging on a nanoslit made in a thin (in comparison with the skin depth) metal slab has been reported by M. A. Seo et al. [83]. The electric field in the nanoslit ($\lambda / 30.000$) appears to be much stronger (by up to a thousand times) than the incident one. It is important that the enhancement is achieved for a single slit in a broad spectral range providing non-resonant behavior of the structure. Therefore, the slit strongly focuses the electromagnetic radiation acting as an optical antenna [84]. The field enhancement strongly depends on the slit width and is inversely proportional to the frequency of the incident THz pulse. That is why the field enhancement is greater for the lower frequencies [85].

3.2 Numerical-, fabrication- and characterization results of THz antennas

3.2.1 Numerical simulation of THz antennas

THz dipole antennas with a gap size from 0.5 μm to 2.5 μm have been numerically simulated with CST microwave studio. They are optimized to have the maximum field at 0.9 THz, which is matched with the maximum amplitude of a THz pulse in the LiNbO_3 THz-TDS system. The geometry of the simulated structure is shown in Fig. 3.1.

Chapter 3 Terahertz field enhancement

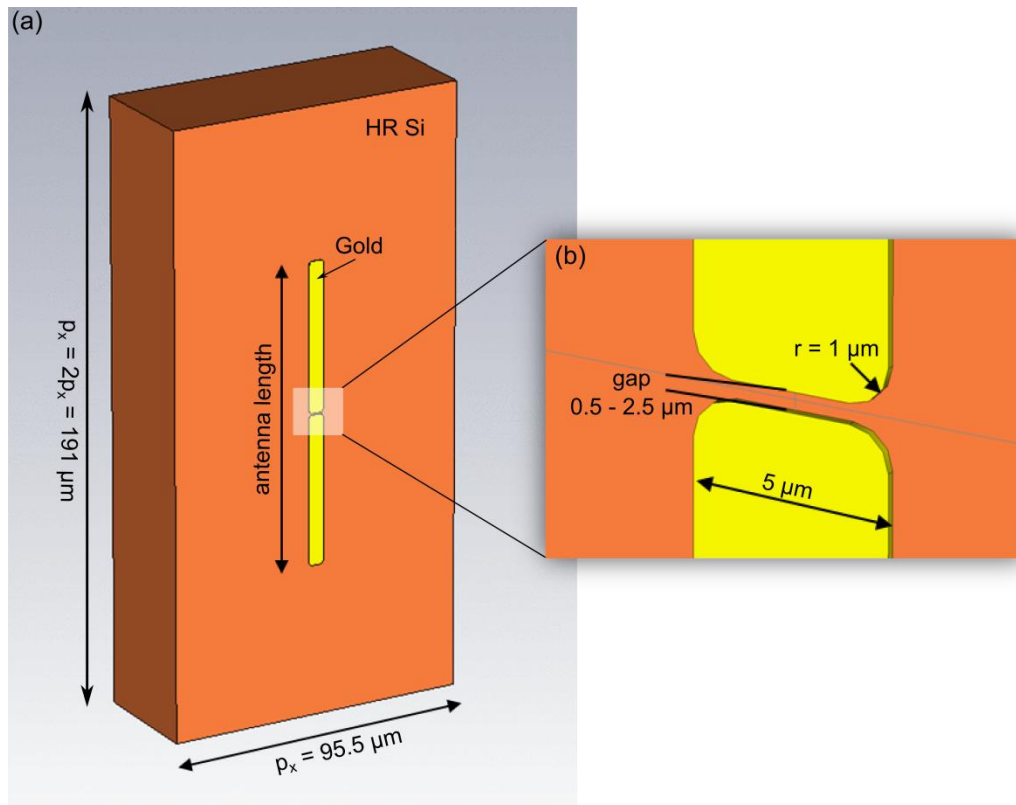


Figure 3.1: (a) Schematic illustration of numerically simulated THz antenna with various gap sizes. (b) Zoom-in on the gap area. HR Si stands for high resistivity silicon.

Figure 3.1 displays the main parameters for THz antennas with optimal electric field enhancement at 0.9 THz. The period of a THz antenna array is held constant (95.5 μm in x -direction and 191 μm in y -direction) for various gap sizes. 200 nm thick gold is used, consistent with the fabricated structures. The width of THz antennas is held constant (5 μm), while the optimal length of the whole antenna varies slightly as the gap size changes. The map of the electric field enhancement for a single THz antenna with 0.6 μm gap is shown in Fig. 3.2.

Chapter 3 Terahertz field enhancement

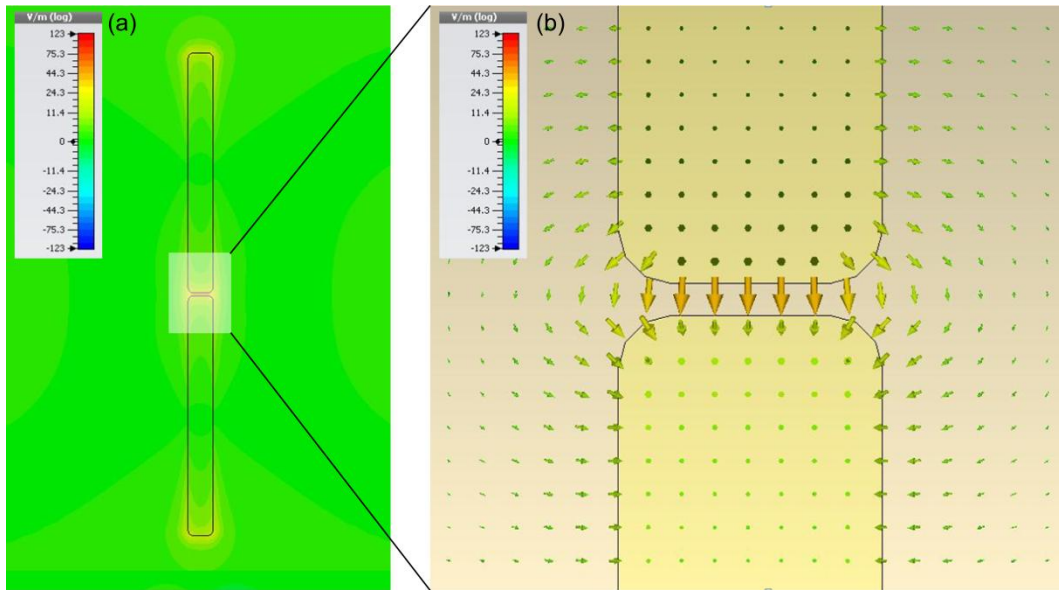


Figure 3.2: (a) Electric field distribution for a THz antenna with a gap size of $0.6 \mu\text{m}$. (b) Zoom-in at the gap.

The profile of electric field enhancement in the gap obtained by numerical simulations with CST microwave studio is shown in Fig 3.2b. The electric field enhancement is highest in the center of the gap, while it decreases slightly further away from the center. It mimics the field obtained by microscopic analytical model described by Dr. Andrey Novitsky in [85]. Table 3.1 summarizes the results of numerically simulated THz antennas. Gap size span between $0.5 \mu\text{m}$ and $2.5 \mu\text{m}$ were chosen, since the highest resolution that can be achieved with UV-lithography is around $1.0 \mu\text{m}$.

Chapter 3
Terahertz field enhancement

Gap size (μm)	Antenna length (μm)	E-field enhancement (at 0.9 THz)
0.5	95.33	134
0.6	96.70	115
0.7	97.79	101
0.8	98.66	90
0.9	99.44	81
1.0	100.13	75
1.25	101.45	61
1.50	102.56	52
1.75	103.44	46
2.0	104.21	41
2.25	104.90	37
2.50	105.54	33

Table 3.1: Field enhancement for various geometrical parameters of THz antennas calculated using CST microwave studio. Optimized for highest electric field enhancement at 0.9 THz. Thickness (200 nm) and width (5 μm) of gold structures are kept constant, as well as the period of the whole THz antenna array $p_y = 2p_x = 95.5 \mu\text{m}$ (see Fig. 3.1).

3.2.2 Fabrication of THz antennas

The THz antennas were fabricated at cleanroom facilities placed at DTU Danchip. The optimized geometrical parameters presented in table 3.1 and Fig. 3.1 were used during fabrication. Gold was chosen as the material for THz antennas, though any other metals as e.g. nickel, aluminum and silver would also be suited. The main fabrication steps are presented in Fig. 3.3.

Chapter 3 Terahertz field enhancement

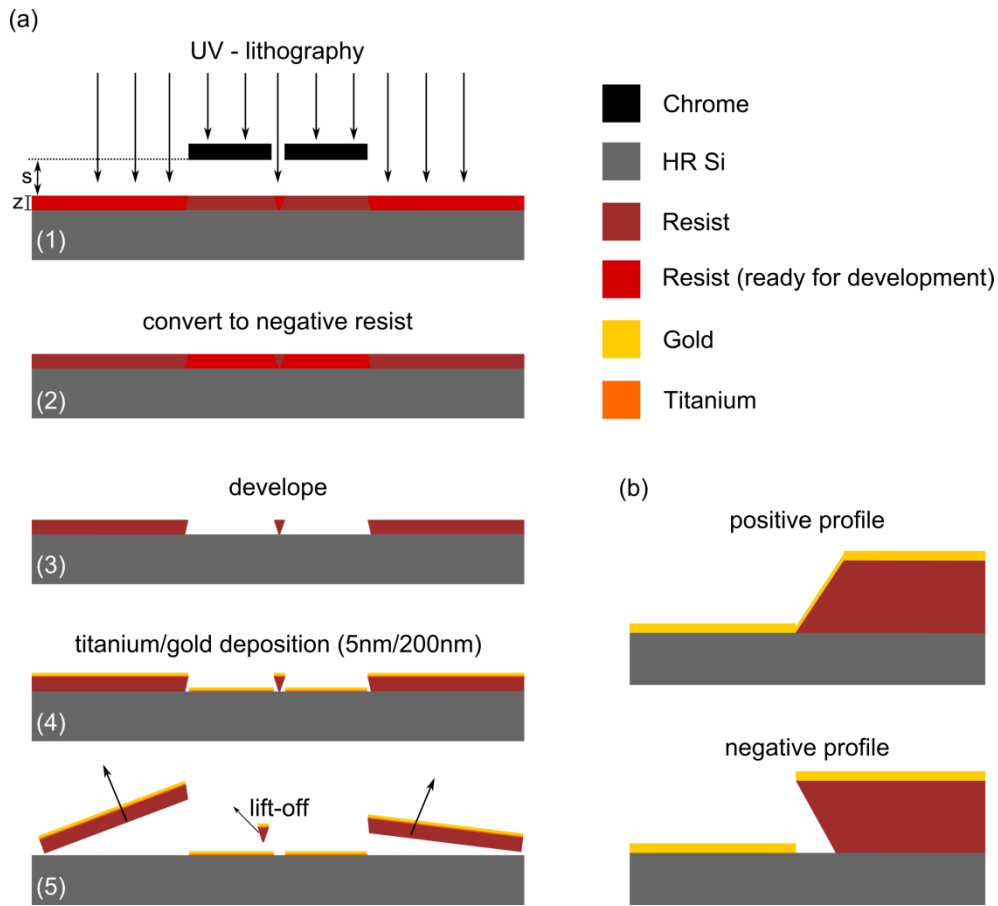


Figure 3.3: (a) Fabrication flow of THz antennas. (b) Difference between positive and negative slope profile of photoresist. (UV) ultraviolet.

The critical dimension of the fabricated THz antennas is the narrow sub-micrometer gap size. As presented in Fig. 3.3a we have chosen the ultraviolet (UV) lithography as the patterning technique due to the possibility of patterning full wafer in a single 3.5 second exposure. It is simultaneously a fast, cheap and widely used technique for mass production, though the resolution that can be obtained by UV lithography is not optimally suited for sub-micrometer dimensions.

The resolution depends on three parameters:

- (1) wavelength λ of the ultraviolet radiation. It is of high importance for the resolution: smaller wavelength, higher resolution. At DTU Danchip a wavelength of 365 nm is used for UV lithography which is capable of approximately 1 μm resolution in the contact mode;
- (2) distance between the mask and photoresist s (see, Fig. 3.3a) should be kept as small as possible to minimize the degree of diffraction of UV light;

Chapter 3 Terahertz field enhancement

(3) thickness of the resist z (see, Fig. 3.3a) and its properties such as sensitivity and contrast. Increase in thickness of the resist worsens the resolution mainly because of the diffraction. An approximate expression for the highest resolution w_{min} that can be defined with UV lithography is given by [86]

$$w_{min} \approx \frac{3}{2} \sqrt{\lambda(z+s)}. \quad (3.1)$$

We used 1.5 μm thick photoresist and performed UV lithography in contact mode, which results in a highest possible resolution of 1.1 μm . Though by slightly over-develop it was possible to achieve gap sizes of approximately 0.8 μm .

Figure 3.3b shows the difference of resist's slope profile for positive and negative processes. The slope profile of negative photoresist is more suitable for lift-off processing, because the contact between the gold on the substrate and the photoresist is minimized. While the slight contact between the two gold layers, as in the case of positive slope profile, can result in an unsuccessful lift-off process.

Photoresist AZ 5214E was used for all UV-lithography processes during this project. It is a positive photoresist and has a spectral sensitivity of 310 – 420 nm. During the baking at approximately 90°C AZ 5214E crosslinks and becomes insoluble in the developer. Under UV exposure (3.5 seconds) the crosslinks are broken and the exposed regions can be developed (Fig. 3.3a, step 1). Though for negative conversion, additional two steps are required before the development: secondary bake at 120°C for 2 min followed by a flood UV exposure for 30 seconds (Fig. 3.3a, step 2). The negatively converted photoresist was thereafter developed in AZ 351B for 75 seconds and thereafter rinsed in water for 2 minutes (Fig. 3.3a, step 3).

To improve the adhesion of gold to high resistivity silicon (HR Si) substrate, 5 nm thick layer of titanium have been evaporated as the initial deposition step. A 200 nm thick gold layer was then deposited by e-beam evaporation (Alcatel SCM 600) at pressure 2×10^{-6} mbar (Fig. 3.3a, step 4). Thereafter it is ready for the final step, namely lift-off. Lift-off is performed in acetone, which dissolves the maintaining of the resist that have been cross-linked during the UV lithography (Fig. 3.3a, step 5). As a result the gold that has been evaporated on top of the

Chapter 3 Terahertz field enhancement

resist will detach from the substrate (HR Si) as the resist gets dissolved and only gold deposited on the substrate will remain. Ultrasound was used during the lift-off to stimulate the process. The total time of lift-off in acetone was approximately 10-15 minutes, where after the samples were rinsed in water for 2 minutes. Figure 3.4 shows the final result of the golden THz antennas on a HR Si wafer.

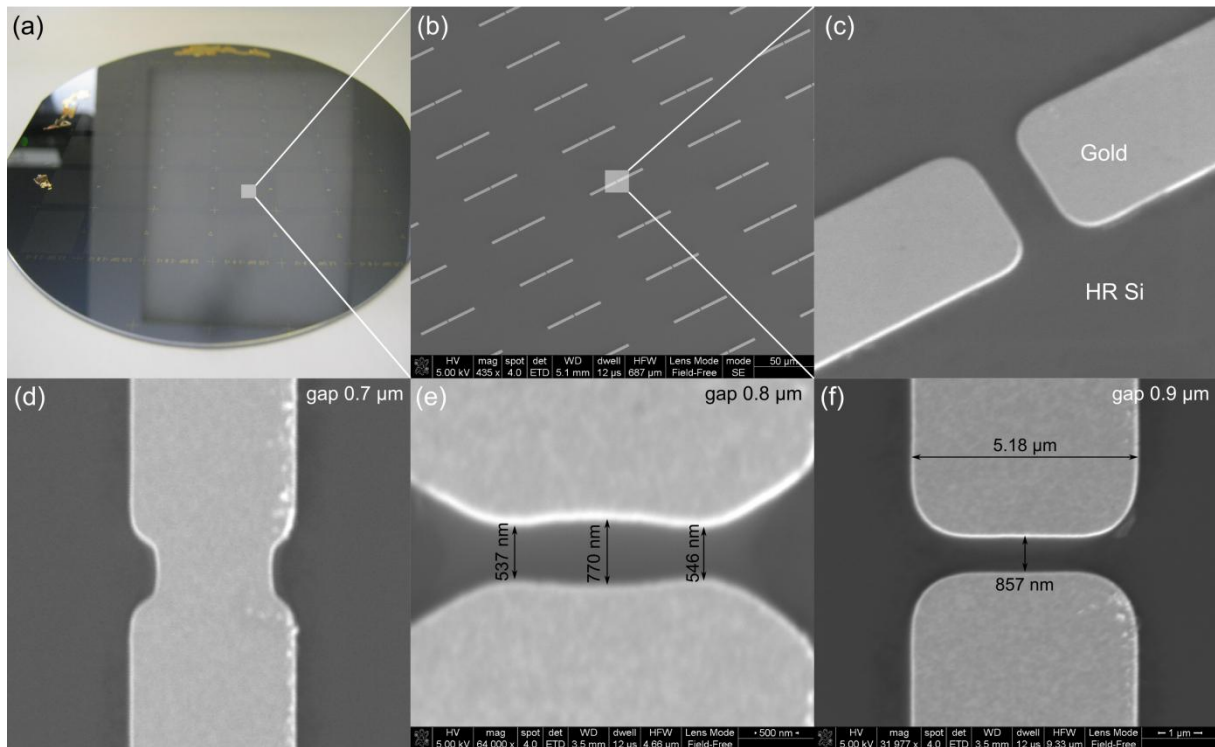


Figure 3.4: THz antennas. (a) Optical image of a 4 inch wafer with 36 samples of THz antenna arrays. (b) SEM image of THz antenna array. (c) Zoom-in on gap area. (d-f) Gap profiles for different initial gap width (defined by UV mask): (d) 0.7 μm , (e) 0.8 μm and (f) 0.9 μm .

As shown in Fig. 3.4a a single 4 inch wafer can easily support 36 samples with an area of 1 x 1 cm. All samples are defined with a single 3.5 second UV exposure, which truly shows the advantages of using UV lithography for mass production purposes. Figures 3.4b,c show a zoom-in SEM images of THz antennas made of gold on a HR Si wafer. During SEM investigation of samples, no local defects as e.g. missing antennas or clusters of gold were seen at the array areas. Figures 3.4d-f show three different gap profiles that have been observed. THz antennas with gap sizes 0.5, 0.6 and 0.7 μm were all intact as shown in Fig. 3.4d (for 0.7 μm). Those sizes did exceed the resolution limitation of UV-lithography performed on a 1.5 μm thick photoresist. The smallest open gap was observed for 0.8 μm sample, though the gap profile exhibits an unexpected shape, with actual gap size going

from 537 nm to 770 nm in a wave-like matter (Fig. 3.4e). The THz antennas with gap sizes span from 0.9 to 2.5 μm had all resulted in expected shaped gap profiles. Figure 3.4f shows the gap profile of a 0.9 μm sample. Though the actual gap size is slightly smaller, namely 857 nm, the width of the antennas is somewhat bigger: 5.18 μm and not 5.0 μm as was defined with the UV mask. The tendency of narrower gap sizes and broader antenna structures than initially defined by the UV mask was observed for all structures. This can be explained by the fact that we slightly over-developing the resist to overcome the resolution limitation of UV lithography. Thus over-developing leads to a larger metallic structures and which resulted in a broader antennas and consequently in narrower gap sizes. This can be corrected by optimizing the pattern of the UV mask.

3.2.3 Characterization of THz antennas

The properties of THz antennas and the influence of electric field enhancements in the order of 30-90 times in the gap region were tested with LiNbO_3 THz-TDS system (section 15), where THz antennas were placed in the sample area (focus spot), see Fig. 2.11. The THz pulses that are generated by LiNbO_3 THz-TDS system have maximum electrical field strength of approximately 400 kV/cm. Our initial measurement of THz antennas produced unexpected and shocking results. The huge electric field enhancement in the gap region together with a very powerful THz source has resulted in damaging the golden structures. Figure 3.5 shows the dramatic damage of gold in the gap region caused by a THz exposure.

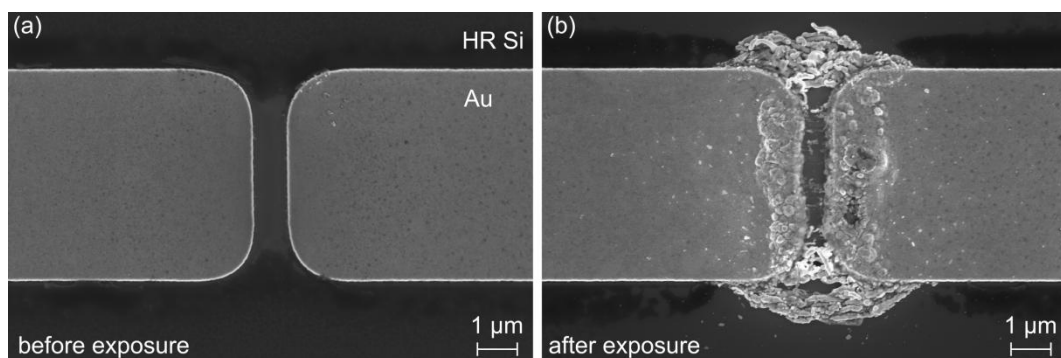


Figure 3.5: SEM images of THz antenna (a) before and (b) after the exposure with a high power THz pulse.

As shown in Fig. 3.5 the THz pulses with maximum field strength of approximately 400 kV/cm focused on the array of the THz antennas causes damaging to the antenna samples in

the gap region, where the electric field is further enhanced. The damage observed in the gap area is caused by well-known effect, namely electromigration. It has had a huge impact on the research concerning electronic devices and is the most challenging problem in reliability of submicron metallic electric circuits [87]. Electromigration is caused by the momentum transfer from the motion of electrons when a strong electrical field is applied. Figure 3.6 illustrates the mechanism of electromigration.

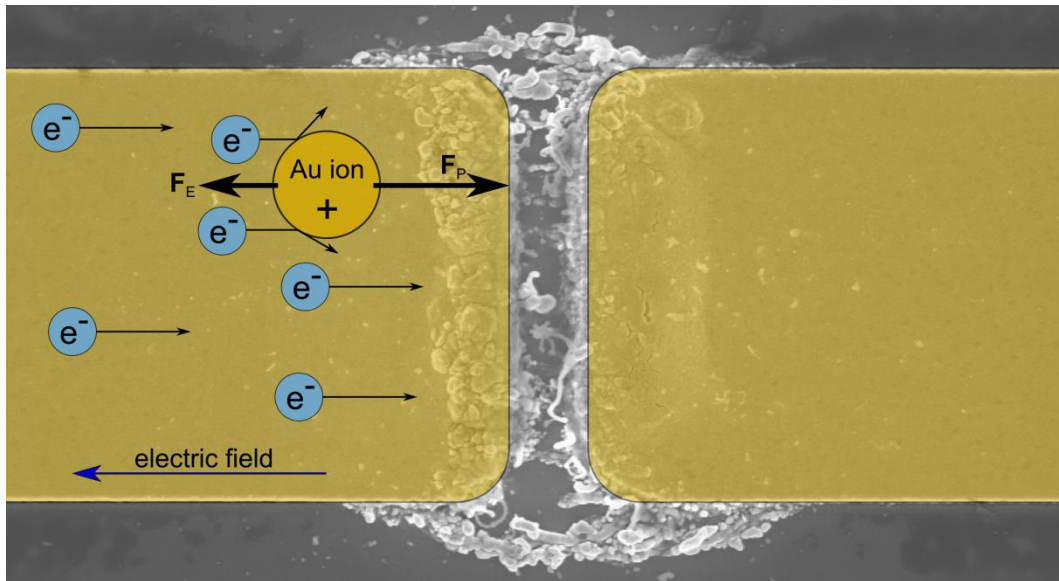


Figure 3.6: Illustration of electromigration combined with a SEM image of an exposed THz antenna (zoom-in on gap area). F_E is the electrostatic force due to the presence of the electric field. F_p is the force from the exchange of momentum during the collision with electrons.

As illustrated in Fig. 3.6 the force from the exchange of momentum during the collision with electrons F_p acting on a gold ion is pointing towards the flow of electron. Such a flow of electrons in metals are also referred to as “electron wind” [88]. Besides the electron wind force F_p , the gold ions will also experience electrostatic force F_E caused by the electric field. The electrostatic force F_E points in the same direction as the electrical field. The direction of gold ions is therefore depends on the balance between electron wind force F_p and electrostatic force F_E . The total force F_T acting on the gold ions in the presence of the electric field can be written as [89]

Chapter 3
Terahertz field enhancement

$$\mathbf{F}_T = \mathbf{F}_E - \mathbf{F}_p = eEZ - eEZ^* = eE(Z - Z^*), \quad (3.2)$$

where E is the amplitude of the electric field, Z is the valence charge of the ion and eEZ^* is the electron wind force. As seen from Eq. (3.2) the total force \mathbf{F}_T acting on the gold ion is proportional to the amplitude of the electric field. The influence of the electric field strength on electromigration in THz antennas has been observed during the SEM investigation and shown in Fig. 3.7.

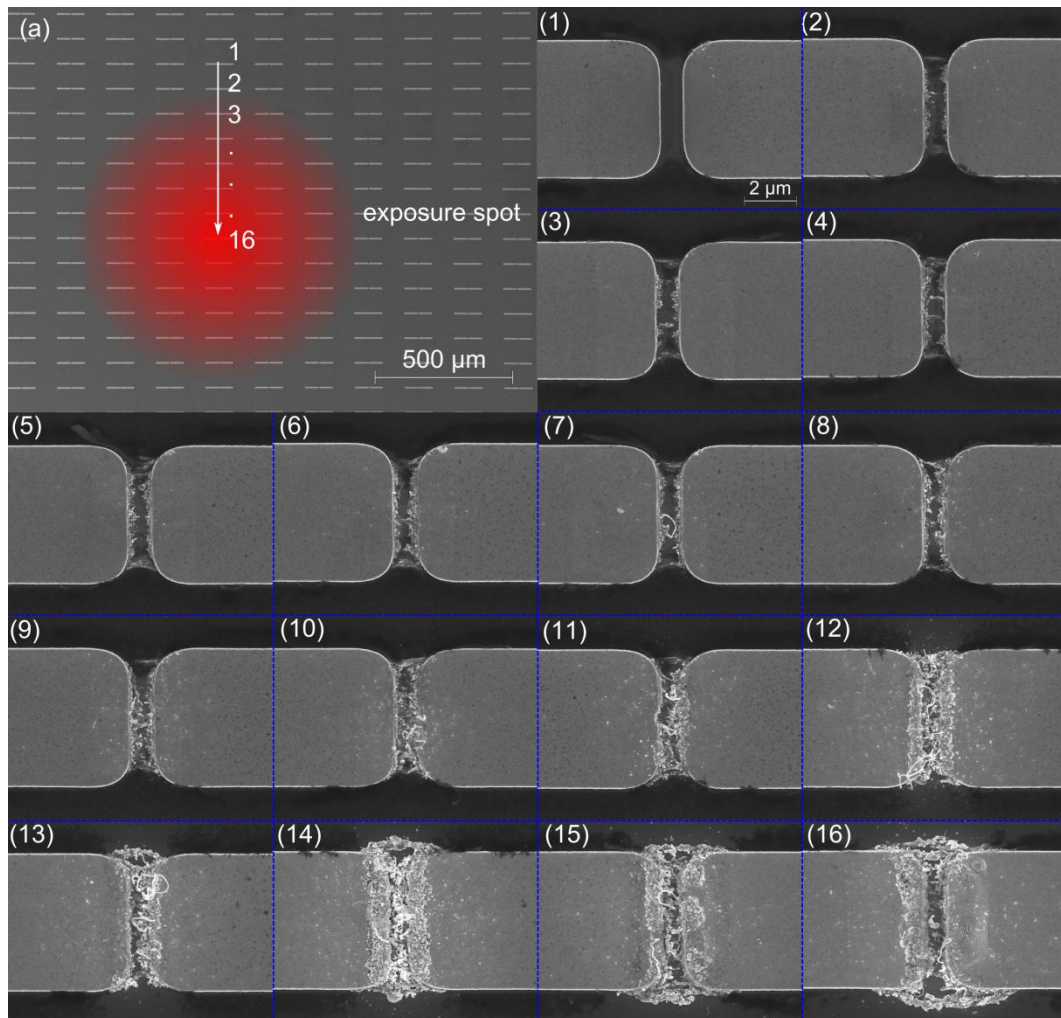


Figure 3.7: SEM images of electromigration at different electrical field strengths of THz radiation. (a) Illustrates the exposure area of the THz antenna array. (1-16) Zoom-in on the sub-micrometer gaps of THz antennas, spanning from (1) none-exposed to (16) located at the maximum electric field.

Figure 3.7 illustrates the dramatic damage of gold structures caused by a high power THz exposure. It is clearly seen that the intensity of electric field has a huge influence on the rate

Chapter 3 Terahertz field enhancement

of electromigration. It was also observed that the electromigration profile did change, when going from low to high electric fields. At lower electric field (Fig. 3.7(1-12)), the electromigration mainly takes place in the gap area, where the electric field enhancement is largest. Whereas at high electrical fields (Fig. 3.7(13-16)), the electromigration pattern has a tendency to take place somewhere away from the gap, where the electric enhancement is lower. We believe that the extremely strong electron wind is able to blow the gold clusters away from the gap area, where the electric field is highest. The two different electromigration patterns together with the numerically simulated pattern of the electric field enhancement are shown in Fig. 3.8.

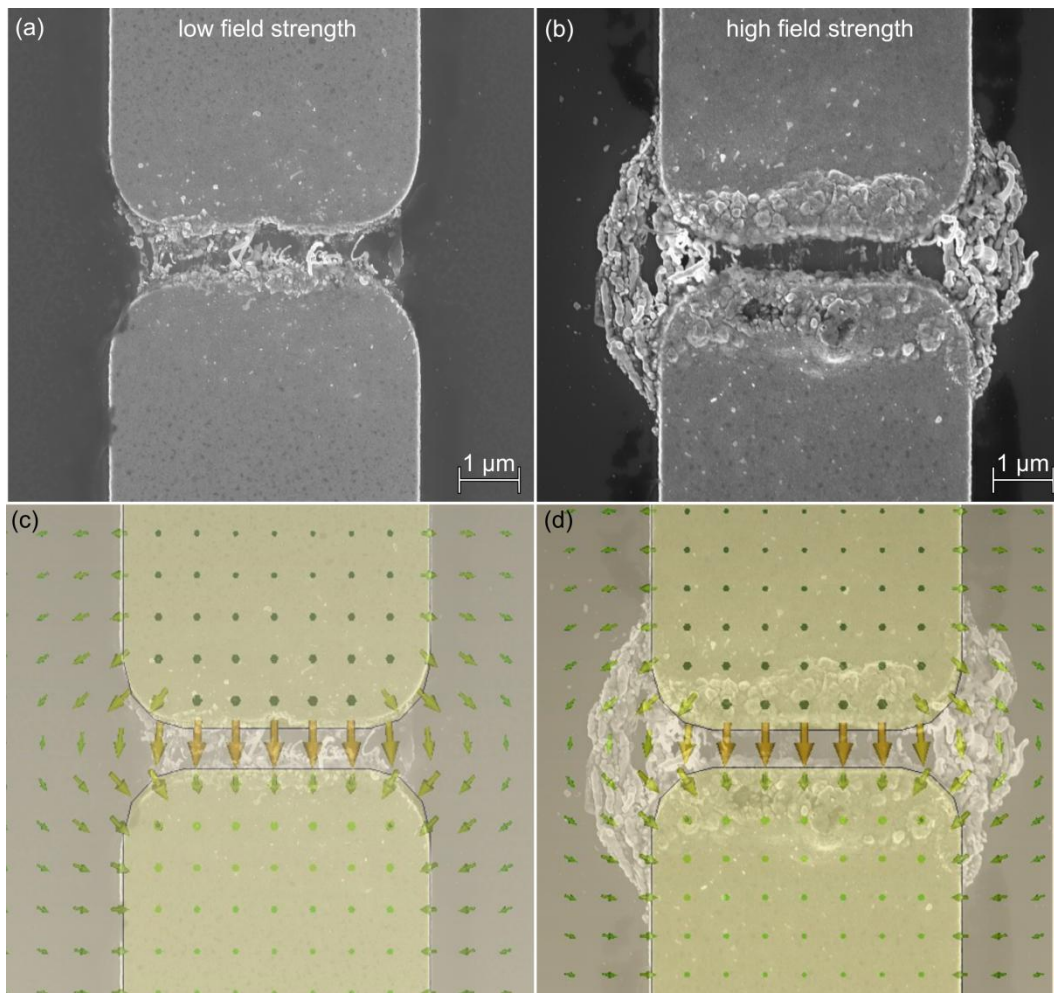


Figure 3.8: SEM images of electromigration profiles at different electrical field strengths together with numerical simulation of electric field enhancement pattern. (a,b) Different electromigration profiles obtained for (a) low and (b) high electric field strength. (c,d) SEM images of electromigration together with numerical simulation of electric field enhancement pattern.

Chapter 3

Terahertz field enhancement

Two electromigration profiles at different THz electric field strengths are clearly seen in Fig. 3.8. Besides the higher rate of electromigration at the high electric field strength (Fig. 3.8b) in comparison with the low electric field strength (Fig. 3.8a), we also observed that there is very low content of electromigrated gold in the gap area when the THz antennas were exposed with the high THz electric field strength. We believe that the lack of gold in the gap can be caused by the intense electron wind, blowing the gold nano-pieces away from the gap area. Figures 3.8c,d illustrate the numerical simulation of the electric field enhancement pattern together with SEM images of the exposed THz antennas.

Besides the high ratio of electromigration in the gap areas of THz antennas, SEM investigation have also surprisingly revealed, that it was possible to visualize the absolute value of the THz antenna's electric field profile, due to the residual layer of photoresist. Figure 3.9 shows the absolute value of the electric field patterns visualized by the residual layer of photoresist, which wasn't fully removed during the lift-off process (see, Fig. 3.3a).

Chapter 3 Terahertz field enhancement

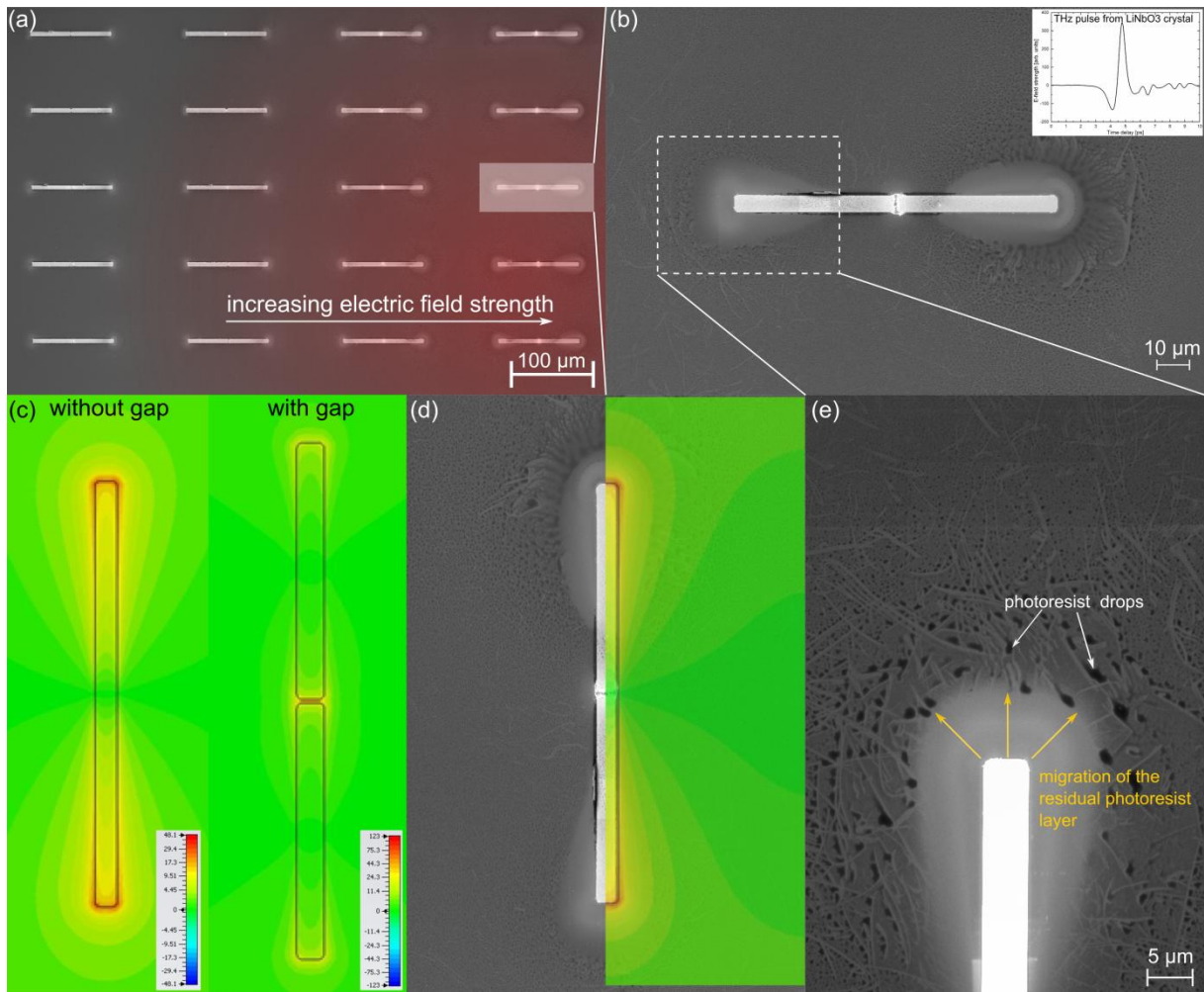


Figure 3.9: Mapping of the electric field profile of an excited THz antenna. (a) SEM image of THz antenna array with increasing electric field strength towards right-low corner. (b) Zoom-in on a single exposed THz antenna (insert: THz pulse in time domain from LiNbO₃ crystal). (c) Numerical simulation of field enhancement map of a single THz antenna. (d) Combined SEM image with numerical simulation. (e) Zoom-in on one end of the THz antenna.

The change in the field pattern of THz antenna as a function of the THz electric field strength has been observed and shown in Fig. 3.9a. By comparing the absolute value of field pattern caused by low electric field strength (Fig. 3.9a, upper left corner) and high electric field strength (Fig. 3.9a, lower right corner) it is clearly seen that the field pattern of THz antennas changes. As expected the electric field pattern is more dominant at higher field strengths.

The electric field pattern of a single THz antenna at high electric field strength is shown in Fig. 3.9b. Besides the visualization of electric field pattern of THz antenna, few other observations can be made. A THz antenna with sub-micrometer gap actually almost behaves as there was no gap. This is the result of extreme rate of electromigration that connects both

Chapter 3 Terahertz field enhancement

metallic structures together (Fig. 3.9b and Fig. 3.8) and therefore the THz antennas behave as a single rod antenna with no gap. There is a little indication of field enhancement close to the gap area, which has most probably taken place just before the electromigration connected the golden structures. The electric field patterns for THz antennas with and without gap are shown in Fig. 3.9c. In Fig. 3.9d, the absolute value simulation of electric field pattern of a numerically simulated THz antenna without a gap is overlapped with a SEM image of THz antenna with a gap. A striking match of the field patterns is seen. Furthermore it is clearly seen in Fig. 3.9b that the electric field pattern of THz antenna is nonsymmetrical. One end of the THz antenna (left side) experience lower field enhancement, than the other end (right side, where the electric field pattern is more pronounced). This is caused by the nonsymmetrical nature of the THz pulse, shown in insert of Fig. 3.9b. The orientation of the nonsymmetrical THz pulse with respect to THz antenna, will determine the direction where the current density will be largest. Based on the pattern of the residual layer of photoresist after the exposure (Fig. 3.9e) it is desired to conclude that the resist is migrated away from the areas where the electric field of THz antenna is very strong. During the migration, the photoresist has the tendency to form droplets as shown in Fig. 3.9e.

3.3 Conclusion

We have fabricated THz antennas with a gap size span from approximately 800 nm to 2.5 μm . The THz antennas were made of gold on top of a high-resistivity silicon wafer. At the resolution limitation of ultraviolet lithography, three different profiles of the gap area were observed (Fig. 3.4). Gaps with the sizes broader than approximately 850 nm possessed the desired profile. Numerical simulations by CST microwave studio have shown that a gap size of 0.8 – 2 μm has a field enhancement of approximately 40 – 90 times. Exposure of THz antennas with high power THz source from LiNbO_3 THz-TDS system have resulted in high ratio of electromigration of gold in the gap area (Figure 3.5). Additionally due to the residual layer of photoresist, it was possible to visualize by SEM the absolute value of the electric field pattern of THz antennas. These field patterns have revealed that THz antennas with a narrow gap behave similar to the ones with no gap. This is caused by the high ratio of electromigration that connects the two metallic structures together.

Chapter 4
Terahertz Metamaterials

4 Chapter

Terahertz Metamaterials

4.1 Introduction

Terahertz (THz) radiation is widely employed in a broad range of fields, e.g. in biology, medicine, communication, security, chemistry, and spectroscopy. To expand the application of terahertz radiation in the aforementioned fields new device designs and fabrication methods are needed. One of the main advantages of the metamaterial (MM) based devices is given by the possibility of broadening photonic component functionalities. The ability of MMs to manipulate the electromagnetic waves makes them natural candidates for THz optical components [90].

In the following sections we will describe three different THz devices based on MMs: (a) polarization sensitive fractal planar metamaterial (PMM), (b) optically active PMMs for polarization manipulation and (c) optically transparent metallic electrodes based on MMs.

4.2 Fractal metamaterials

In this section we present a THz fractal PMM design that shows very high transmission in the desired frequency range as well as a clear differentiation between one polarization and another. An original fabrication method to produce large area (up to several cm^2) freely suspended flexible metallic membranes is implemented to fabricate the fractal metamaterial. Based on numerical predictions we fabricated and characterized a fractal based THz PMM that shows more than 60 % field transmission at around 1 THz for TE polarized light while the TM waves have almost 80 % field transmission peak at 0.6 THz. One of the main characteristics of this design is its tunability by design: by simply changing the length of the fractal elements one can choose the operating frequency window. We show that such PMMs present a clear polarization-dependent behavior. Such structures were initially investigated theoretically in the microwave region [91], this work represents a direct

extension towards shorter wavelengths. The fabrication method presented in this work has great potential for exploitation in terahertz optics. The modeling, fabrication and characterization results will be presented in following chapters.

4.2.1 Numerical simulations of fractal metamaterial

The electromagnetic wave properties of the THz fractal PMMs were studied by finite-difference-time-domain (FDTD) simulations. Fig. 4.1 shows schematically a unit cell of the PMM structure that we studied, which is a set of slits arranged in certain hierarchy as the 5-level fractal.

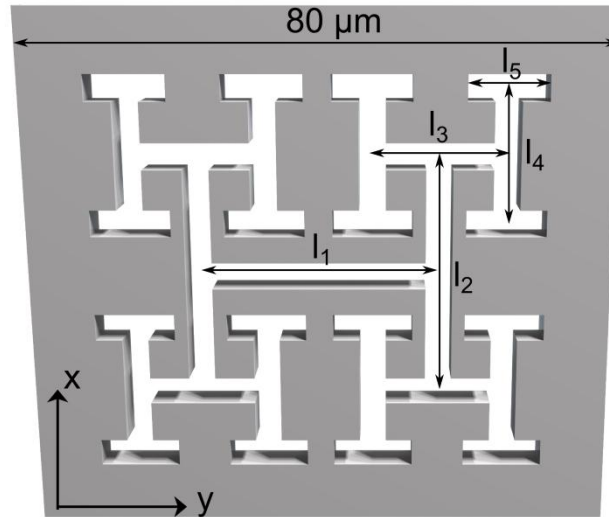


Figure 4.1: Show schematic pictures of the simulated unit cell structure. (a) the lattice constant of the PMM is $a = 80 \mu\text{m}$, other geometrical parameters are given by $l_1 = l_2 = 40 \mu\text{m}$, $l_3 = l_4 = 20 \mu\text{m}$, $l_5 = 14 \mu\text{m}$, and the slit width is $1.2 \mu\text{m}$. Here, the x axis is perpendicular to l_1 , and the thickness of the nickel layer is $2 \mu\text{m}$.

We first employed the FDTD simulations to study the transmission/reflection properties of the structure. In our simulations, we assumed nickel as perfect electric conductor, which is reasonable for most of metals in the THz frequency region. We also defined the x-y axes with respect to the unit cell orientation such that the x-axis is perpendicular to the major fractal slit – the first level fractal, l_1 (see Fig. 4.1a).

The FDTD-calculated normal-incidence transmission and reflection spectra (amplitude and phase) are shown in Fig. 4.2 for $E||y$ and $E||x$ polarizations.

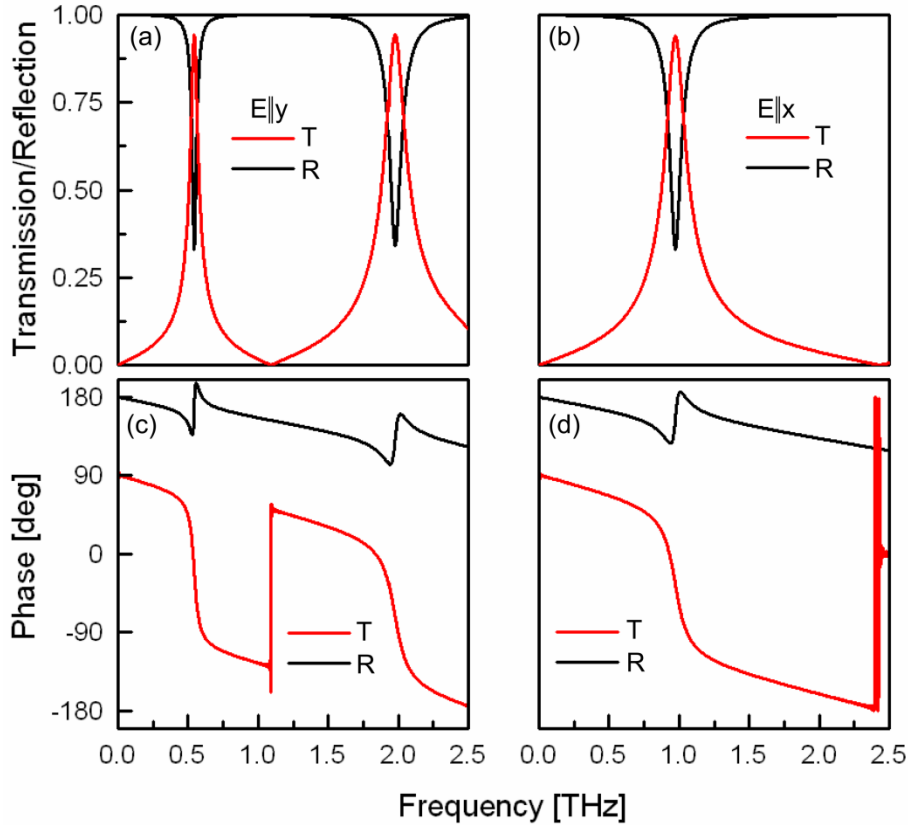


Figure 4.2: (a-d) show FDTD calculated normal incidence transmission/reflection spectra (amplitude and phase) of the fractal PMM for the $E||y$ (a,c) and for $E||x$ (b,d) polarizations.

For the $E||y$ polarization, we found two transmission peaks (with transmittance approaching 100%) at 0.6 THz and 2 THz (Fig. 4.2a), identified as the first and third resonances of the 5-level fractal structure. These resonances can also be clearly observed as characteristic acute 180-degree jumps in the transmission and reflection phases, as seen from Fig. 4.2c. The minimum transmittance observed at 1.1 THz is due to an anti-resonance formed by the interplay of the two resonances at 0.6 and 2 THz, and thus associated with a sharp π phase shift. On the other hand, a transmission peak at 0.96 THz is identified for the $E||x$ polarization, which is the second resonance of the fractal structure (Fig. 4.2b). Again this transmission enhancement is accompanied by a distinct resonance in the transmission and reflection phases (Fig. 4.2d).

These high transmission phenomena are rather intriguing at first sight, since one may notice that the metal filling fraction is of about 90-95 % making most areas of the PMM covered with metal, which is opaque at THz frequencies. To explore the inherent physics behind such anomalous high transmission behavior, the electric field distributions inside the fractal slits

at two high transmission frequencies 0.6 THz and 0.96 THz (see Fig. 4.2a,b) were calculated. FDTD simulations revealed that electric field in the slits is significantly enhanced at these high transmission frequencies, as shown in Fig 4.3.

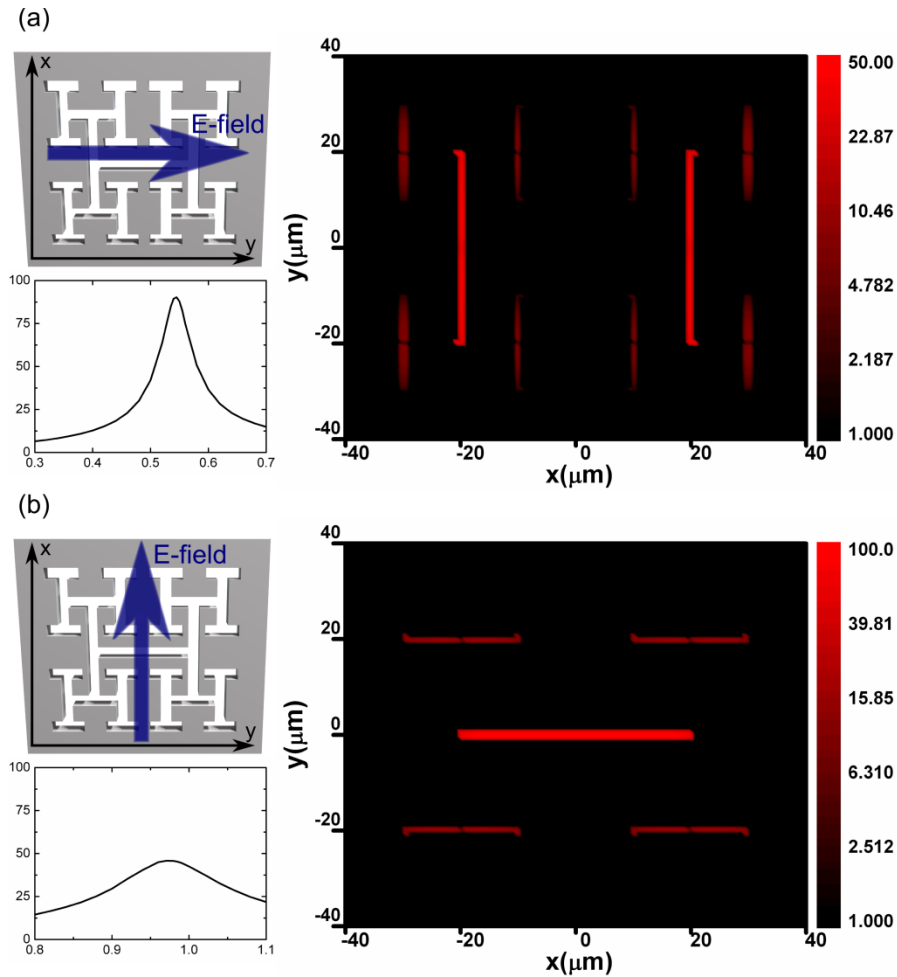


Figure 4.3: The FDTD calculated electric field distributions inside the fractal slits for two resonance transmissions at (a) 0.6 THz and (b) 0.96 THz, calculated by FDTD simulations with input electric field polarized such that (a) $E \parallel y$ and (b) $E \parallel x$.

It is interesting to note that the local field enhancement mainly occurs at the lowest-level slits perpendicular to the electric field orientation of the fractal structure. The local electric field is enhanced by over 80 times for the resonance at 0.6 THz, and 40 times at 0.96 THz.

Investigation of transmission behavior as a function of the incident angles φ or θ was performed and presented in Fig. 4.4.

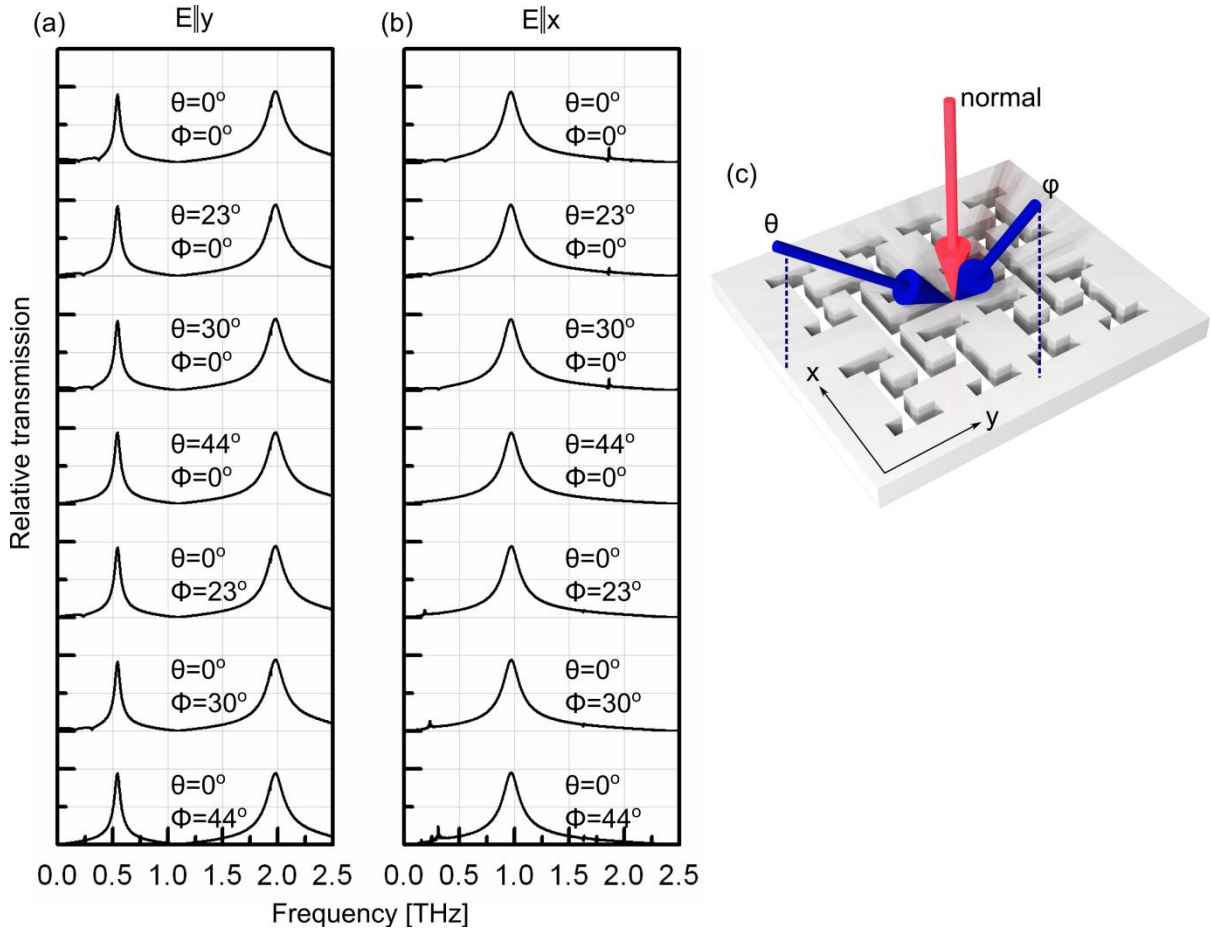


Figure 4.4: FDTD calculated transmission spectra through the fractal PMM as a function of the incident angle (φ/θ) for (a) polarization $E \parallel y$ and for (b) $E \parallel x$. (c) angles φ and θ are shown with the respect to the normal incidence (perpendicular to the surface).

Keeping electric field parallel to the y or x axis, we varied the incidence angles to calculate the transmission spectra Fig. 4.4a. The definition of angles φ and θ with respect to normal incidence is shown in Fig. 4.4c. For all three transmission peaks, the center frequencies are robust against varying the incident angles, which are the typical behaviors of local resonances.

4.2.2 Fabrication of fractal metamaterial

We have developed a fabrication process to grow at least $2 \mu\text{m}$ thick nickel (Ni) PMM membranes with areas from $1 \times 1 \text{ cm}^2$. The thickness of the Ni PMM film is limited primarily by the thickness of the photoresist used to define the surface structures. The dimensions which can be reached with our process are difficult to achieve by traditional lift-off processes due to the following factors. The deposition of metals on the photoresist sidewalls

Chapter 4 Terahertz Metamaterials

during the evaporation process is critical to avoid for the lift-off. This is because the overall shape of the metallic structures depends on the amount of metal deposited on the sidewalls, and this cannot be accurately controlled with such a thick photoresist. Additionally, one needs a rather high ratio, on the order of at least 5:1, between the thickness of the photoresist itself and the metal deposited on top of it, and it is difficult to perform precise UV-lithography on a very thick photoresist with sufficient final resolution of the pattern, see section 3.2.2. Our process clears away these limitations. Additionally our fabrication process leads to free-standing membranes, thus eliminating substrate influences such as increased reflection losses and Fabry-Perot interference effects.

The fractal PMM structures were thin metallic membranes suspended in air. Due to the THz beam spot size, we choose to fabricate membranes of 1 x 1 cm in area. In the same time, the thickness of these membranes is 2 μm , making them extremely fragile and thus extra care when handling them had to be taken. In Fig 4.5 the main process steps are shown.

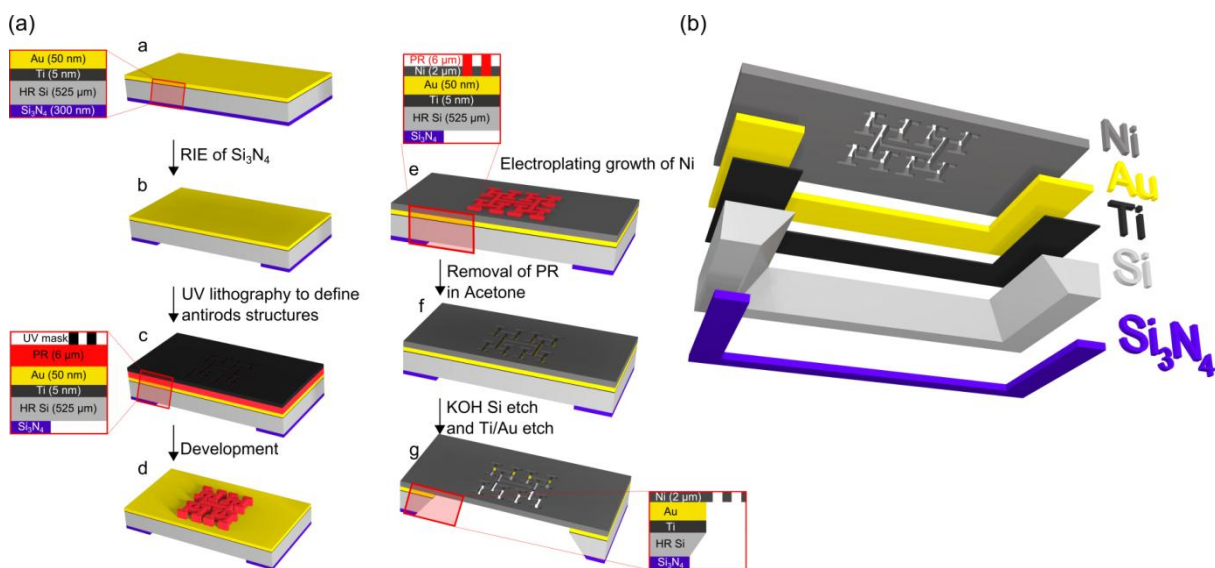


Figure 4.5: (a) Main fabrication steps and (b) schematic overview of the structure. Not drawn to scale.

In the fabrication flow, we start with a double-side polished 525 μm -thick Si wafer. On the front side we evaporate a double layer of Ti/Au. The 5 nm thin Ti layer is used to promote the adhesion of gold to the substrate, while the 50 nm of Au is the seed layer for the electrochemical growth of the Ni membrane. On the backside of the substrate, 300 nm of Si_3N_4 is deposited by plasma-enhanced chemical vapor deposition (Fig. 4.5a,a). The bottom

Chapter 4

Terahertz Metamaterials

layer of Si_3N_4 is needed to protect the edges of the Si wafer from etching with KOH, depicted in the step between (Fig 4.5a,f) and (Fig 4.5a,g). After these initial steps (Fig. 4.5a,a), the membrane aperture is defined through standard UV-lithography exposure on the backside of the substrate. The next step is the removal of the Si_3N_4 by reactive ion etching using the PR as a mask. The result can be seen schematically in (Fig. 4.5a,b). Once the membrane aperture position is defined, the rest of the process steps are performed relative to it. We then spin a thick (approximately 6 μm) PR on the top side of the wafer and, using aligned exposure with the substrate backside, define the structures on top of the Si_3N_4 aperture (Fig. 4.5a,c). After the development of the photoresist (Fig. 4.5a,d) we grow 2 μm of Ni using electroplating (Fig. 4.5a,e). The nickel electroplating electrolyte is of the sulphamate type, and is optimized for low internal stress, small grain size, and zero defects. The electrolyte is operated at a relatively low temperature of 32 °C, using mild agitation with purified compressed air and continuous monitoring of internal stress and pH value. The nickel is deposited at a current density of 1.38 A/dm² corresponding to a deposition rate of 0.25 $\mu\text{m}/\text{min}$. The next step is the removal of the remaining photoresist in acetone, resulting in the desired Ni structure on the Si/Au substrate (Fig. 4.5a,f). The Si wafer is then back-etched in an 80 °C KOH bath. Here, the Si_3N_4 layer acts as the etch mask. The etching rate is approximately 1.3 $\mu\text{m}/\text{min}$, and therefore this is the longest step in the fabrication process, with duration of approximately 6-7 hours. The KOH etch is easily controllable and is not aggressive to the Ni membrane (Ni is passive in most high pH solutions), so the structure definition is preserved throughout the etch process. The last step in the process is the selective removal of the Ti/Au layer using a commercial etching solution, Entreat 100, from Engelhard, NJ, USA (Fig. 4.5a,g). A schematic overview of the completed structure can be seen in Fig. 4.5b.

In Fig. 4.6 SEM images of the obtained structures are shown.

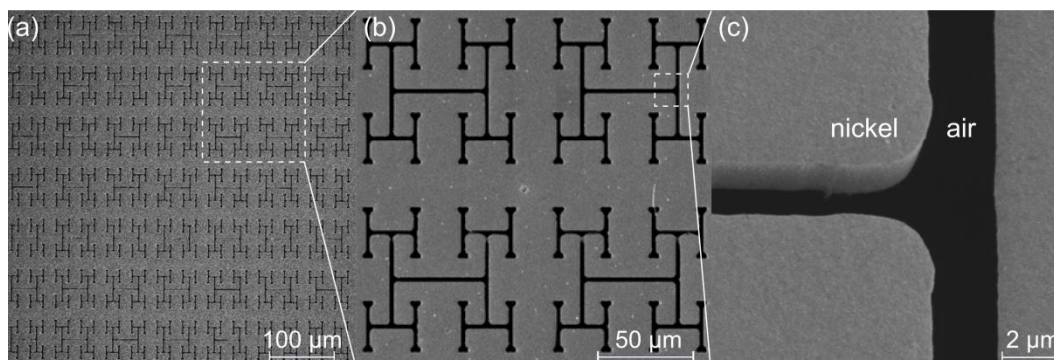


Figure 4.6: SEM images of the fractal PMM. (a) overview of the periodic array showing high uniformity over the exposed area; the total sample area was 1 x 1 cm. (b) zoom-in on four unit cells of the structure. (c) zoom-in on the nickel/air interface showing the quality of the structures. In both figures, the grey areas represent the Ni while the black ones are the air slits

4.2.3 Characterization of fractal metamaterial

The fabricated fractal samples were characterized by THz time-domain spectroscopy (THz-TDS) based on photoconductor switches. In brief, we used photoconductive switches excited by femtosecond laser pulses to generate and detect THz pulses with a frequency content spanning the 0.2-3.0 THz range. This technique allows precise sampling of the electric field of the THz transient. The THz pulse is detected after transmission through the sample, and compared to the THz pulse transmitted through an empty aperture. By measuring the electric field in the time domain both the amplitude and phase are obtained and used to calculate transmission amplitude. For more detailed description of THz-TDS based on photoconductive switches, see section 1.2. The results of the transmission measurements are summarized in Fig. 4.7.

Chapter 4 Terahertz Metamaterials

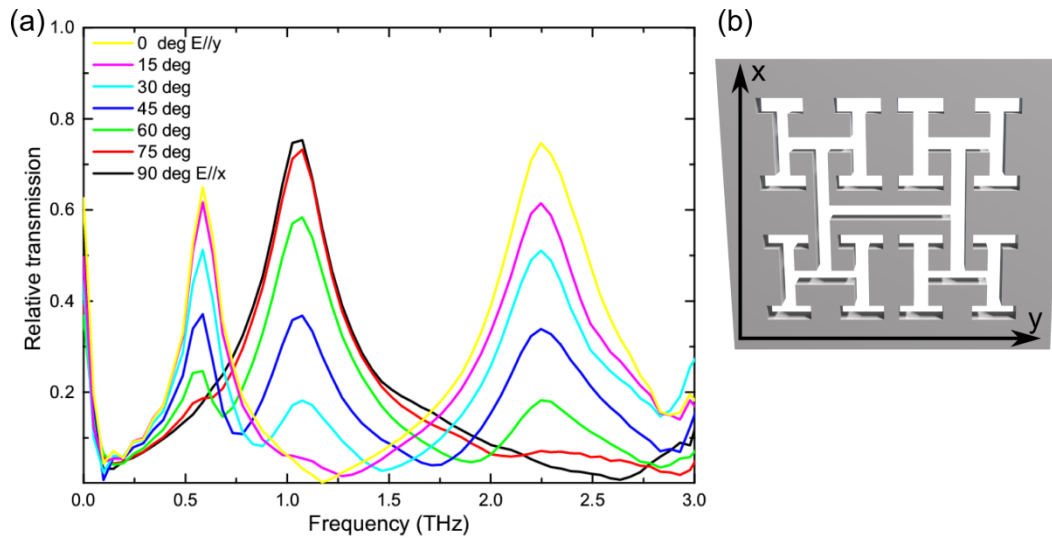


Figure 4.7: Measured relative transmission amplitude normalized to air. The THz beam was at normal incidence. (a) the polarization angle is gradually changed from $E||y$ (yellow line) to $E||x$ (black line) in steps of 15 degrees. (b) unit cell of fractal PMM with the orientation of y and x axes.

The measurements were carried out with the linearly polarized THz beam normally incident onto the fractal PMM. Polarization of the beam was varying from $E||y$ (yellow line) to $E||x$ (black line). In very close agreement with the simulation results we observe distinct resonances in the transmission amplitude at 0.55 THz and 2.55 THz for the $E||y$ polarization (see Fig. 4.2). The anti-resonance behavior of the fractal structure is also clearly seen between the first and the third resonances at 1.05 THz. For the $E||x$ polarization of the incident THz light we observe a broader resonance at 1.1 THz and an anti-resonance at 2.7 THz. Polarization changes make the transmission pictures evolve from one extreme case to another. At 45° polarizations all three resonances are visible in the transmission spectrum, being almost identical in height (blue line in Fig. 4.7).

To confirm the angle independence on the behavior of the fractal material as was numerically shown in Fig. 4.4, transmission measurements were carried out at normal incidence (0°) and at 20° incidence angle. The results of the transmission measurements at 0° and 20° degrees both for $E||y$ and $E||x$ polarizations are shown in Fig. 4.8.

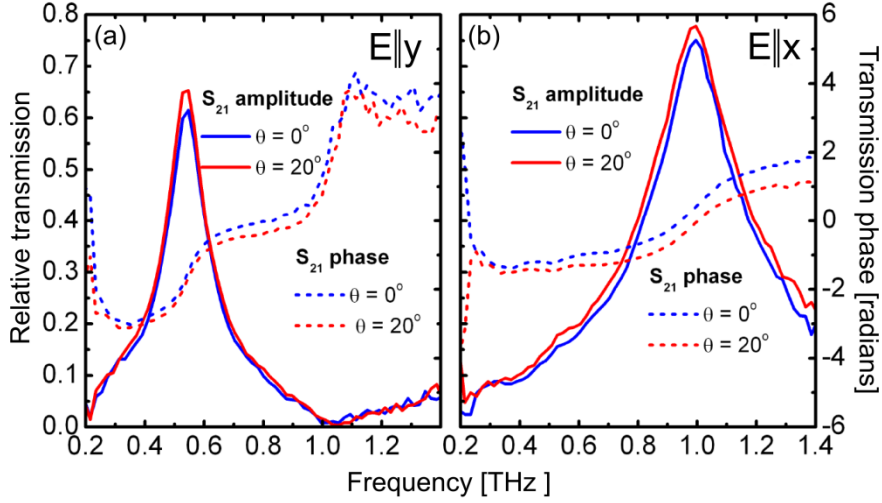


Figure 4.8: Measured transmission amplitude (solid curves) and transmission phase (dashed curves) of fractal PMM. (a) results for the $E||y$ polarization, and (b) results for the $E||x$ polarization. Results for two different incidence angles; normal incidence (blue curves) and 20° (red curves) are shown.

The results obtained at these two incidence angles are very similar, confirming the robustness of the resonance frequencies with respect to the incidence angle variations, as predicted by the numerical simulations (see Fig. 4.4). We note that the definition of the phase sign in the experimental data is opposite of that used in the simulations (see Fig. 4.2). This is of no importance, as is the direction of the sharp π phase shift. Thus we find excellent agreement between experimental and simulation results. The main differences between the simulation and experimental results are to be attributed to the experimental difficulties, both in fabrication and measuring.

4.3 Optical active metamaterials

Various chiral metamaterial designs have already been proposed and characterized [92], [93], [94], [95], [96], [97]. Many of the proposed designs are complex (e.g. consisting of multi-layer or truly three dimensional structures) making them hard to fabricate or integrate as a THz-optic component. On the other hand, the majority of metamaterials for the THz region are supported by either a bulk silicon wafer or thin layer of material such as polyimide, silicon nitride, silk or paper, which inevitably leads to increased optical losses [98], [99], [100], [101]. In this work, we used the fabrication method described in chapter

Chapter 4 Terahertz Metamaterials

4.2.2 to achieve large area, freestanding, micrometer thick flexible planar metamaterials (PMMs).

Within a simple geometric framework, PMMs can acquire pronounced optical activity relative to their thickness. We follow the concept of asymmetric nano-rod dimers with straight, non-parallel elements of different sizes, as theoretically described in [102]. This structure mimics the widely used asymmetric split ring geometry [93], though with straightened segments. It was shown that this structure possesses strong optical activity due to elliptical dichroism [102]. In our case, instead of having a metamaterial consisting of metallic rods, we chose its inverse (Babinet) counterpart, where the rods are substituted by hollow elements (antirods) in a metal membrane [103], as shown in Fig. 4.9.

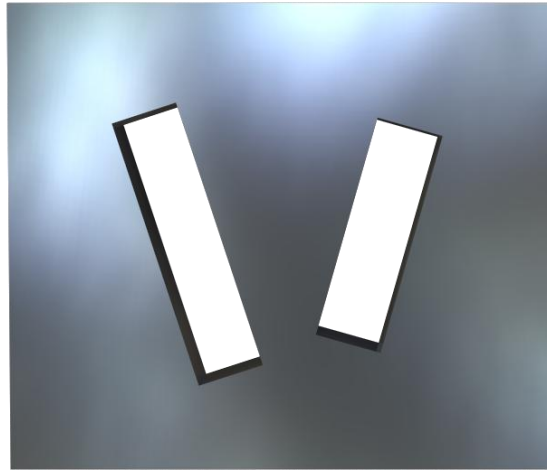


Figure 4.9: Unit cell of Babinet-inverted dimer MM, where two hollow elements are air.

According to the Babinet principle [104], [105], spectral properties of such mutually inverse structures (rods and slots) are predicted to be similar, but inverted. The metallic bars will normally have a resonance deep in transmission, while the inverted structure as shown in Fig. 4.9, will experience the opposite namely a transmission peak around the resonance frequency. To differentiate our PMM from that reported in [102], we refer to our design as the Babinet asymmetric dimer. The Babinet structure makes it possible to design and fabricate a freestanding PMM film consisting only of metal. Besides the advantages with respect to fabrication and mechanical properties, the Babinet design resonantly increases transmission near the frequencies where the PMM displays the highest optical activity.

In this chapter we describe a Babinet-inverted dimer metamaterial possessing strong optical activity. Its optical properties are characterized by terahertz time-domain spectroscopy, revealing anisotropic transmission with high optical activity. A simple coupled resonator model is applied to explain the principal optical features of the dimers, with predictive power of positions and number of resonances through a parametrical model.

4.3.1 Analytical and numerical model

The measurement results were compared with the result of full-wave numerical simulations performed using Ansys-HFSS, a commercial finite element electromagnetic field solver. The dielectric function of Ni was modeled using a 5-pole Drude-Lorentz model [106].

The power transmission T can be determined from numerical simulations as

$$T = \frac{\int \mathbf{S}_{tot} \cdot \hat{z} dA}{\int \mathbf{S}_{inc} \cdot \hat{z} dA} = \mu_0 c_0 \frac{\int \text{Re}[\mathbf{E} \times \mathbf{H}^*] \cdot \hat{z} dA}{AE_{inc}^2}, \quad (4.1)$$

using the total fields (\mathbf{E}, \mathbf{H}) on the detector surface A below and parallel to the Ni membrane. Here μ_0, c_0 and E_{inc} denote the vacuum permeability, vacuum speed of light, and electric field amplitude of the incident plane wave, respectively.

The amplitude linear-polarization transmission coefficients τ_{ij} for an \hat{x}_j -polarized incident wave are calculated as

$$\tau_{ij} = \frac{\int \mathbf{E} \cdot \hat{x}_i dA}{\int \mathbf{E}_{inc} \cdot \hat{x}_j dA}, \quad (4.2)$$

To obtain a deeper physical understanding of spectral properties of the Babinet PMM we employ a coupled-dipole theory developed previously for plasmonic nanorod dimer metamaterials [102], [107]. Making note of the fact that a nanoslot antenna can be described by a bound-charge oscillator model similar to a nanorod antenna [108] by virtue of the Babinet principle, we can assume that each individual slot responds to the incident

Chapter 4
Terahertz Metamaterials

harmonically oscillating electric field \mathbf{E}_0 with an induced dipole moment $\mathbf{d}_{1,2} = \boldsymbol{\alpha}_{1,2}\mathbf{E}_0$, where the polarizabilities $\boldsymbol{\alpha}_{1,2}$ are tensors of the form

$$\boldsymbol{\alpha}_{j=1,2} = \frac{f_j}{\omega_j^2 - \omega^2 - i\omega(\gamma_j + \delta_j\omega^2)} \hat{\boldsymbol{\mu}}_j \otimes \hat{\boldsymbol{\mu}}_j = \alpha_j(\omega) \hat{\boldsymbol{\mu}}_j \otimes \hat{\boldsymbol{\mu}}_j, \quad (4.3)$$

Here the expression $\hat{\boldsymbol{\mu}}_j \otimes \hat{\boldsymbol{\mu}}_j$ denotes the outer (dyadic) product of the unit vector pointing along the slot orientation with itself as shown in Fig. 4.10. The parameters f_j , ω_j , γ_j , and δ_j are determined by fitting the results of numerical simulations.

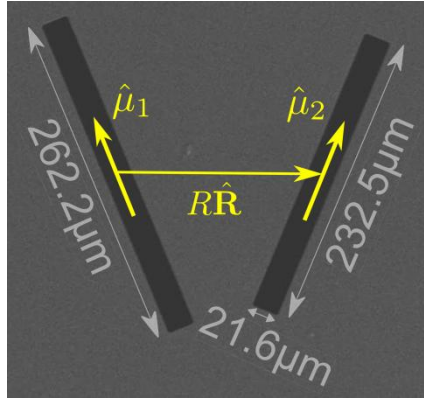


Figure 4.10: SEM image of unit cell showing the unit vectors defining the dimer geometry.

When two slots are coupled together in a dimer, their dipole moments are modified by the presence of each other. This can be accounted for by the Green function approach [107], resulting in a system of coupled equations for $\mathbf{d}_{1,2}$ and the following form of the total effective dipole polarizability of the dimer

$$\boldsymbol{\alpha}^{eff} = \frac{\alpha_1 \hat{\boldsymbol{\mu}}_1 \otimes \hat{\boldsymbol{\mu}}_1}{1 - \kappa^2 \alpha_1 \alpha_2} + \frac{\alpha_2 \hat{\boldsymbol{\mu}}_2 \otimes \hat{\boldsymbol{\mu}}_2}{1 - \kappa^2 \alpha_1 \alpha_2} + \frac{\kappa \alpha_1 \alpha_2}{1 - \kappa^2 \alpha_1 \alpha_2} (\hat{\boldsymbol{\mu}}_1 \otimes \hat{\boldsymbol{\mu}}_2 + \hat{\boldsymbol{\mu}}_2 \otimes \hat{\boldsymbol{\mu}}_1), \quad (4.4)$$

where κ is the coupling coefficient determined by the relative arrangement of the slot elements. The detailed procedure of its calculation can be found elsewhere [102]. Neglecting interaction between the neighboring dimers in the lattice, we can determine the effective permittivity tensor of the metamaterial as $\boldsymbol{\epsilon}^{eff} = 1 - (\epsilon_0 V_{cell})^{-1} \boldsymbol{\alpha}^{eff}$. Representing the actual

metamaterial as a slab of this effective material, we can then use the generalized transfer-matrix approach [109], [110] to determine the reflection and transmission spectra. Previous accounts demonstrate a good agreement of this approach with direct numerical simulations for rod dimers [102], [107].

Figure 4.11 compares the analytically calculated transmission spectra for the V-shaped (Fig. 4.11a) and parallel \parallel (Fig. 4.11b) dimer structures with the results of the full-wave simulations.

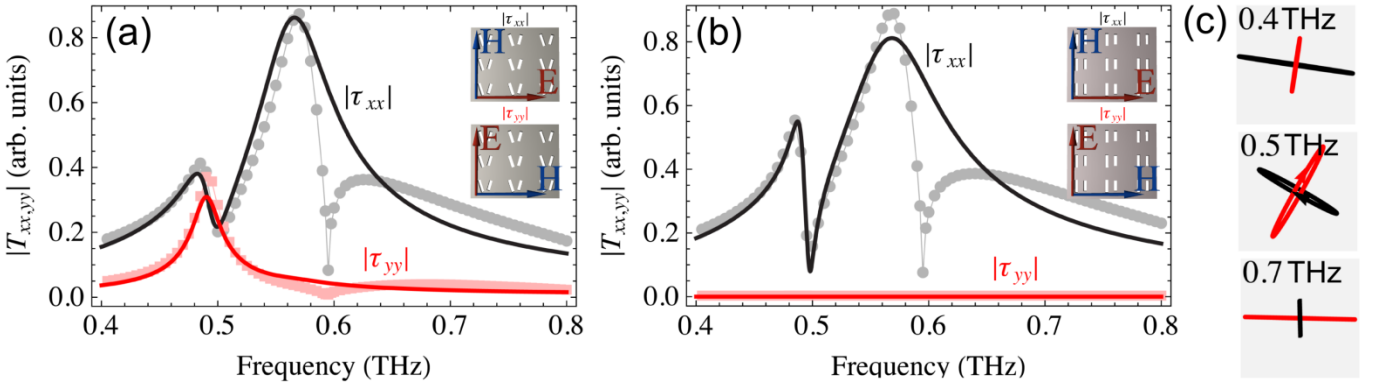


Figure 4.11: Transmission spectra τ_{xx} and τ_{yy} for (a) V-shaped and (b) parallel-shaped dimer metamaterials, analytically determined from the proposed theory (lines) compared to direct numerical simulations (dots). The dimer dimensions are shown in Fig. 4.1. (c) eigenpolarizations for three different frequencies (0.4, 0.5, and 0.7 THz).

We see that by properly choosing the parameters in Eq. (4.3), a very good qualitative agreement can be achieved, thus confirming that the coupled dipole model captures the underlying physics of wave interaction with the slot dimer metamaterials. The sharp dip seen at 0.6 THz in the simulated spectra results from lattice effects (the Rayleigh anomaly), when the wavelength of light equals the lattice period. In experiment, the PMM interacts with a finite-sized beam rather than an infinitely extended plane wave, therefore, this lattice-related dip is much less pronounced (but still visible) in the measured spectra. For the same reason, the second resonance (at 0.56 THz) is more pronounced in simulations than in measurements (see, Fig. 4.15).

We can now explain why there are two peaks in τ_{xx} and only one in τ_{yy} , for the V-shaped structures. From the analytical description given above, we can determine the polarization eigenstates [109] $\mathbf{e}_{1,2}$ of the PMM, i.e., polarization states that remain unchanged as a wave

Chapter 4
Terahertz Metamaterials

passes through the metamaterial. An arbitrarily polarized incident wave can be now obtained by its expansion in the eigenstates basis,

$$\mathbf{E}_\alpha(\omega) = C_\alpha^1(\omega)\mathbf{e}_1(\omega) + C_\alpha^2(\omega)\mathbf{e}_2(\omega), \quad \alpha = x, y, \quad (4.5)$$

where $C^{1,2}(\omega)$ are the expansion coefficients and leading to the following form of the transmission components $\tau_{\alpha\beta}$ of Eq. (4.2),

$$\tau_{\alpha\beta} = C_\beta^1(\omega)t_1(\omega)C_\alpha^1(\omega) + C_\beta^2(\omega)t_2(\omega)C_\alpha^2(\omega), \quad (4.6)$$

where $t_{1,2}(\omega)$ are transmission spectra of the eigenmodes. This finally results is

$$\tau_{xx} = [C_x^1(\omega)]^2 t_1(\omega) + [C_x^2(\omega)]^2 t_2(\omega), \quad \tau_{yy} = [C_y^1(\omega)]^2 t_1(\omega) + [C_y^2(\omega)]^2 t_2(\omega). \quad (4.7)$$

The result of Eq. (4.7) is presented in Fig. 4.12.

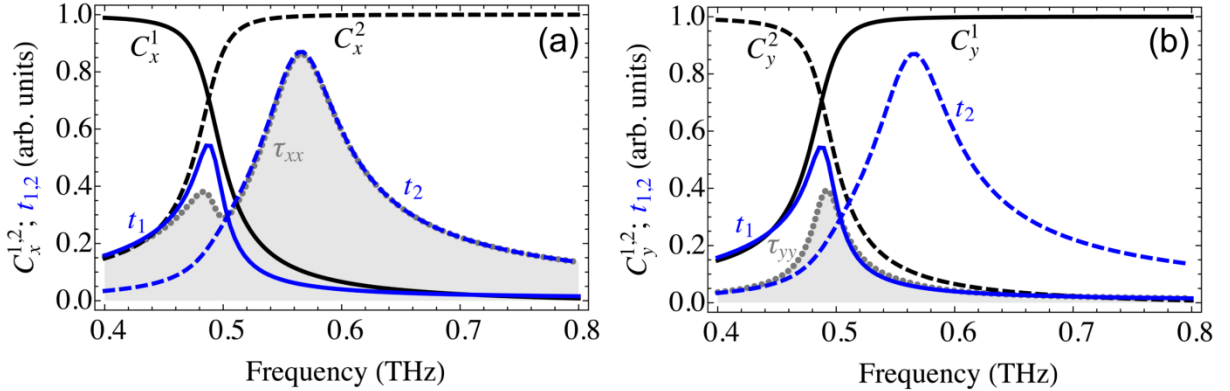


Figure 4.12: Eigenmode transmission coefficients $t_{1,2}(\omega)$ together with the eigenmode expansion coefficients for the incident light linearly polarized (a) along the x-axis: $C_x^{1,2}(\omega)$; (b) along the y-axis: $C_y^{1,2}(\omega)$. The dotted lines with shading denote the resulting transmission τ_{xx} and τ_{yy} given by Eq. (4.6).

As seen in Fig. 4.12, the transmission spectra for the two eigenmodes $t_1(\omega)$ and $t_2(\omega)$ have resonance peaks at respective frequencies, associated with the presence of two rods with different lengths (see Fig. 4.1). However, the expansion coefficients $C^{1,2}(\omega)$ are flipped near a certain frequency between these resonance peaks, so a linearly polarized incident wave

predominantly couples to the mode \mathbf{e}_1 at lower frequencies, and to the mode \mathbf{e}_2 for higher frequencies. This is a purely geometrical effect, resulting from a specific dependence of polarization eigenstates on frequency, $\mathbf{e}_{1,2}(\omega)$, as seen in the in Fig. 4.11c, and determined by the mutual orientation of the slots in the dimer.

When the incident wave polarization is rotated, the coupling coefficients in Eq. (4.5) are expectedly reversed, $C^1_x(\omega) = C^2_y(\omega)$, $C^1_y(\omega) = C^2_x(\omega)$. Hence, for one polarization the peaks in $t_{1,2}(\omega)$ coincide in frequency with regions where $C^{1,2}(\omega)$ are large. As a result, Eq. (4.6) gives a two-peak dependence that corresponds with the two eigenmode resonances. For the other polarization, strong $t_{1,2}(\omega)$ at the peaks is cancelled by weak $C^{1,2}(\omega)$ at those frequencies, so a significant response is only seen where the four quantities, $t_{1,2}(\omega)$ and $C^{1,2}(\omega)$, are all significantly non-zero. This is the case only in the overlap region between the eigenstate resonances, where the eigenpolarizations display sufficient ellipticity, resulting in a weaker response with only one peak.

In contrast to the V-shaped dimers, the parallel dimers can only have linearly polarized eigenmodes, which is seen from Eq. (4.4) since $\hat{\mu}_1 \parallel \hat{\mu}_2$. Therefore only one polarization of the incident light can couple to the resonant modes of the dimer in the first place, barring any significant response for the orthogonal polarization.

4.3.2 Fabrication of optical active metamaterials

The Babinet-inverted dimer metamaterial membranes were fabricated with an area of $8 \times 8 \text{ mm}^2$, and a thickness of $2 \text{ }\mu\text{m}$. Such a huge aspect ratio (1:4000) poses various challenges in the fabrication process. The thickness of $2 \text{ }\mu\text{m}$ was chosen for mechanical robustness of the sample.

The structure of the fabricated MMs is shown in Fig. 4.13, which was initially model with following dimension dimensions: the lengths $l_1 = 260 \text{ }\mu\text{m}$ and $l_2 = 230 \text{ }\mu\text{m}$, width $d = 20 \text{ }\mu\text{m}$, spacing $\Delta = 160 \text{ }\mu\text{m}$ of the two slots, angle $\alpha = 45^\circ$ between them, and periodicities $\Lambda_x = \Lambda_y = 500 \text{ }\mu\text{m}$.

Chapter 4 Terahertz Metamaterials

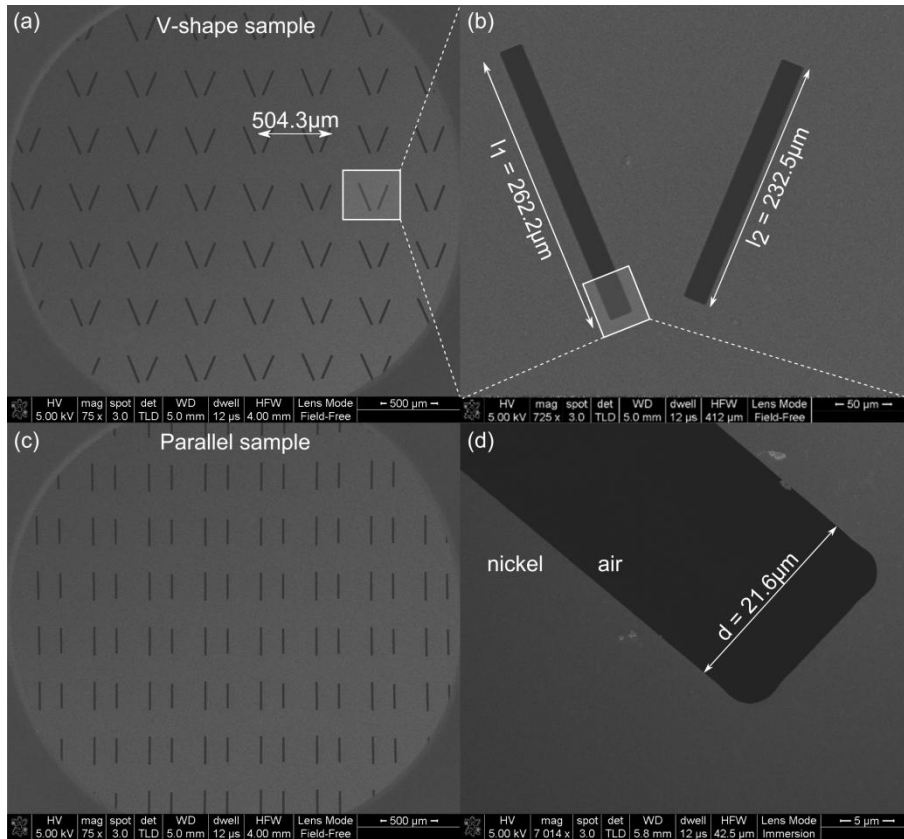


Figure 4.13: SEM images of (a) V-shape and (c) parallel samples with a period of 500 μm. (b) unit cell of a V-shape MM sample. (d) zoom-in on a single dimer's tip, showing the sharply defined border between nickel and air.

Figure 4.13a-d demonstrates that the features of fabricated MMs are sharply defined, with all critical design dimensions preserved. The dimensions of the dimers are slightly larger (2 μm) than initial design, though such small differences have no sufficient effect on the behavior of the MMs. No defects as missing dimers and cracks were detected during investigation by SEM and an optical microscope.

In Fig. 4.14 optical images of the Babinet-inverted dimer MMs are shown.

Chapter 4
Terahertz Metamaterials

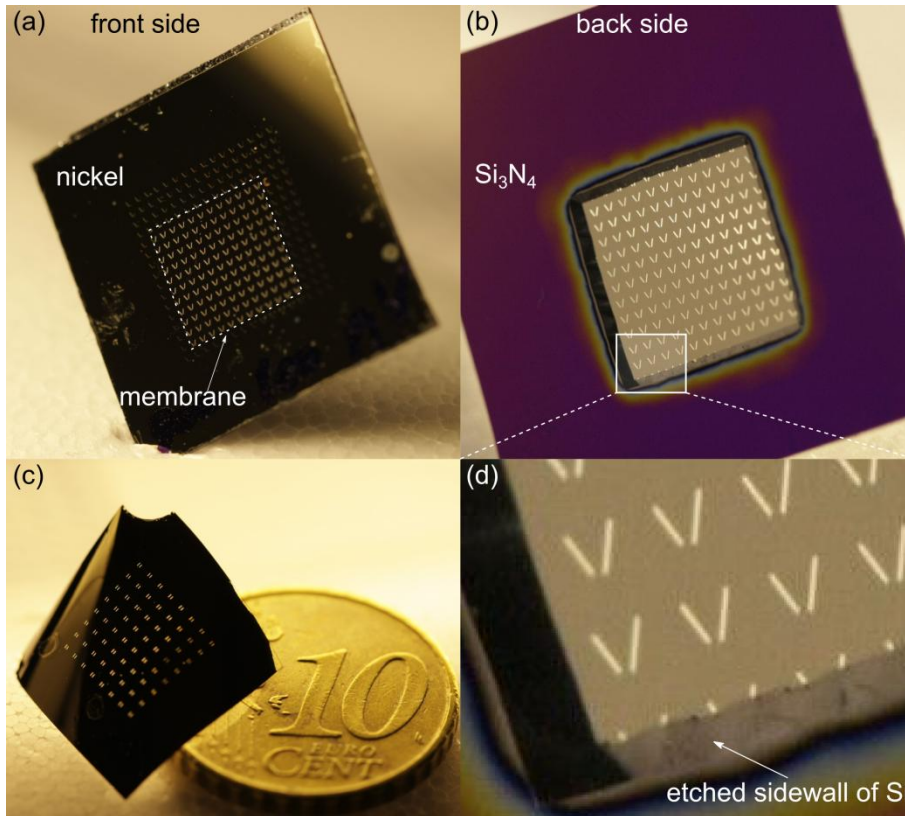


Figure 4.14: Optical images of Babinet-inverted dimer MMs. (a) front and (b) back side of the sample. Silicon is used as the frame to handle the sample during the measurements. (c) nickel membrane detached from the Si frame. The membrane, although very thin, is resistant enough to be removed from the Si frame and used as flexible THz MM. The 10 cent coin is used for size comparison. (d) zoom-in on sidewall of etched silicon wafer.

Figures 4.14a,b shows the MM sample. Both from the front and back side Si frame can be clearly seen and, at the same time, light passes through the dimer structures, showing that all other layers behind the membrane are removed. It should be mentioned that during the KOH etch of Si, the $\langle 111 \rangle$ crystallographic plane is inert, thus allowing for a very smooth and clean side of the frame as shown in Fig. 4.14d. Figure 4.14c shows the membrane completely detached from the frame. Apart from a slight defect in the top corner, the membrane is complete and the structures are intact. This demonstrates that the Ni layer is sufficiently mechanically robust to serve as a flexible structure and that membranes with larger dimensions can be fabricated.

4.3.3 Characterization of optical active metamaterial

Transmission spectra of the Babinet-inverted dimer MMs for linearly polarized light were measured by a commercial terahertz time-domain spectroscopy (THz-TDS) system (Picometrix T-Ray 4000). The system generates and records the THz transients using photoconductive switches that are fiber coupled to a femtosecond laser. The system operates at a scan rate of 100 Hz, and we record the average of 100.000 waveforms (time window 320 ps, total acquisition time 17 min) with spectroscopic information from 0.1 to 2.0 THz and an electric field dynamic range of 3200 at 0.5 THz (70 dB power dynamic range). Figure 4.15 displays the transmission spectra for the two orthogonal linear polarizations for both the V-shape and parallel slots dimer PMM. Linear polarization transmission coefficients are recovered by cross polarization measurements, where the transmission through air is used as a reference, $\tau_{ij}(\omega) = E_{ij}^{sample} / E_{ij}^{reference}$, where indices i and j can be either x or y . The incident polarization is controlled by rotation of the samples.

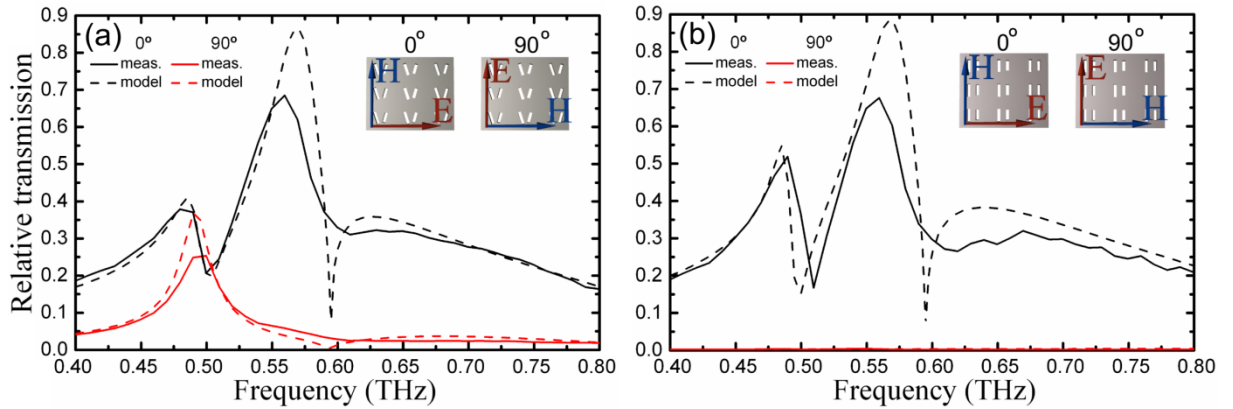


Figure 4.15: Relative amplitude transmission $|\tau|$ of (a) V-shaped and (b) parallel Babinet-inverted planar MM. Measurements (solid curves) and numerical simulation results (dashed curves) are shown for two different rotation positions of the sample, 0° ($|\tau_{xx}|$, black curves) and 90° ($|\tau_{yy}|$, red curves). The insets illustrate the sample orientation with respect to the incident electromagnetic fields.

At 0° incident polarization (see inset of Fig. 4.15a) two transmission resonances at 0.48 and 0.56 THz are observed for both samples. Even though the hollow elements cover only 4.3 % of the total Ni membrane area, an enhanced relative field transmission amplitude as high as 0.67 is observed for the resonance at 0.56 THz [111]. The two transmission resonances

Chapter 4 Terahertz Metamaterials

occur due to a favorable coupling between the incident field and the eigenmodes of the metamaterial structure. Since the dimensions of the slot are identical for both parallel and V-shape samples, the transmission peaks appear at the same frequencies, with similar strengths and widths. The relative strength of the two resonances (which can be individually suppressed or enhanced) is influenced by the distance between the hollow asymmetric elements [112]. A parallel slot dimer PMM is geometrically similar to a wire grid polarizer, so expectedly, the transmission coefficient drops to zero when the sample is rotated by 90° . In contrast to this, we observe a single transmission peak at 0.5 THz for the V-shape sample rotated by 90° (Fig. 4.15b). As described in chapter 4.3.1, this is the result of interplay between the coupling of the incident radiation to the PMM eigenmodes, and the corresponding transmission efficiencies of the eigenmodes themselves.

To discuss the optical activity properties of the MMs, it is useful to determine their optical response with respect to their circular polarization components. The components of the circular-polarization transmission matrix t are recovered from the linear-polarization coefficients τ_{ij} by the standard transformation

$$\begin{pmatrix} t_{++} & t_{+-} \\ t_{-+} & t_{--} \end{pmatrix} = \frac{1}{2} \begin{pmatrix} \tau_{xx} + \tau_{yy} + i(\tau_{xy} - \tau_{yx}) & \tau_{xx} - \tau_{yy} - i(\tau_{xy} + \tau_{yx}) \\ \tau_{xx} - \tau_{yy} + i(\tau_{xy} + \tau_{yx}) & \tau_{xx} + \tau_{yy} - i(\tau_{xy} - \tau_{yx}) \end{pmatrix}. \quad (4.8)$$

The resulting power transmittances ($T_{++} = |t_{++}|^2, T_{--} = |t_{--}|^2$) and circular polarization conversion coefficients ($T_{+-} = |t_{+-}|^2, T_{-+} = |t_{-+}|^2$) extracted from the measurements are presented in Fig. 4.16.

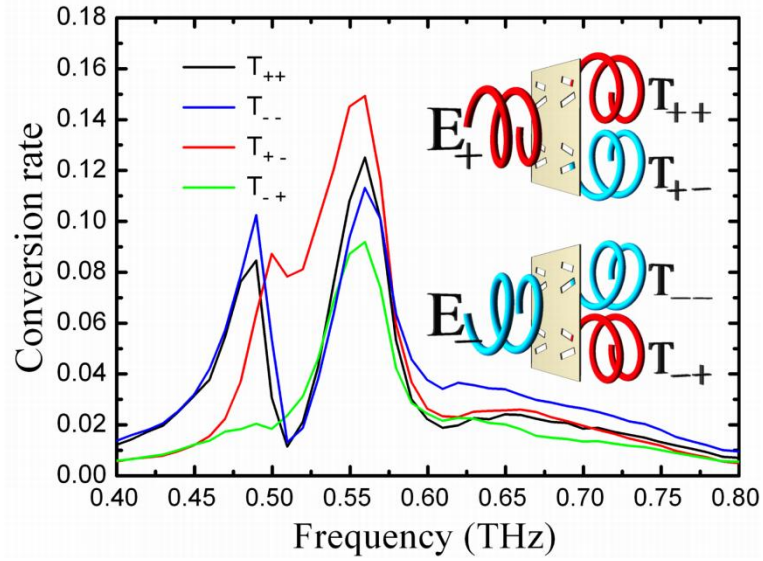


Figure 4.16: Relative transmission (T_{++} , T_{--}) and circular polarization conversion (T_{+-} , T_{-+}) in terms of power for V-shape slot planar metamaterial.

We observe a pronounced anisotropic transmission behavior for the V-shaped MMs. Although the transmission of the right-handed polarization component (T_{++}) is almost equal to the left-handed polarization component (T_{--}), the circular polarization conversion rates are significantly different. In the frequency range from 0.49 to 0.52 THz, the conversion difference between left-to-right (T_{+-}) and right-to-left (T_{-+}) circular polarizations is approximately 65 %, coinciding with the frequency band of high transmission.

Since no noticeable difference is observed for T_{++} and T_{--} we conclude that the V-shape antirod planar structure exhibits no sizable circular dichroism within a broad frequency band. However, the PMM has pronounced *elliptical* dichroism, which results in significant optical activity, shown in Fig. 4.17.

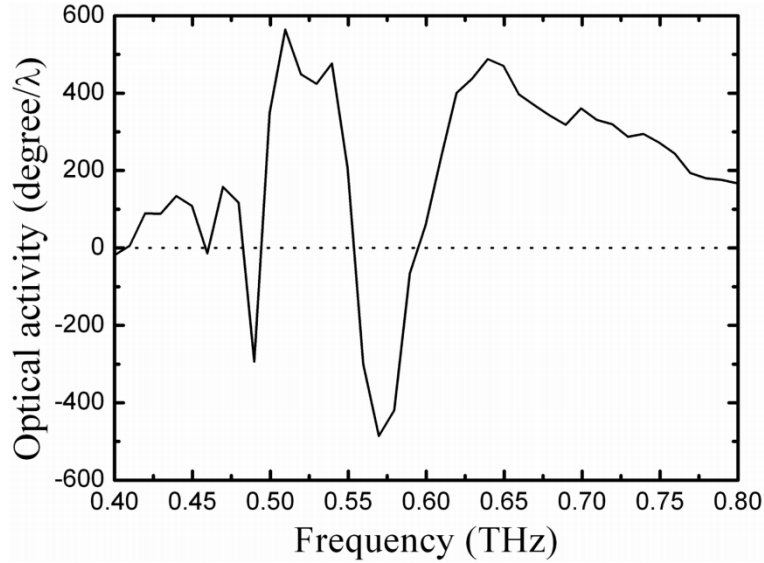


Figure 4.17: Optical activity for V-shape dimer MM.

As seen in Fig. 4.17 the optical activity reaches a maximum of the polarization plane rotation rate of approximately $500 \text{ }^\circ/\lambda$ at 0.53 THz. Such huge optical activity is comparable with performance of more complex (dual layer) designs reported previously [113], [114].

The corresponding parallel Babinet PMM does not exhibit any optical activity. This shows that the asymmetric design of the V-shaped slot dimers is crucial for the anisotropic transmission behavior.

4.4 Transparent metallic electrodes based on metamaterials

For developing the new generation of electronic devices, varying from solar cells to electronic paper, touch screens, and displays, there is a clear need for transparent contact electrodes (TCEs) [115]. We define such contacts by their possibility of allowing a certain portion of the electromagnetic spectra of interest to pass through the contacts while, in the same time, maintaining the electrical connections intact. The research in this field is developed mainly towards transparent conductive oxides, conjugated polymers, colloidal semiconductors, and carbon allotropes in order to obtain low-cost and large-scale compatible electrodes [116]. Nowadays, the most promising material for TCEs is Indium-Tin-Oxide (ITO) [117]. Although it shows clear advantages with respect to its competitors, ITO comes with the inherent limitations. On one side, the scarcity and continuous increase in the

price of indium, the main component of ITO is of great concern for an eventual implementation in the everyday devices. On the other, ITO is very brittle thus making devices like electronic paper or flexible screens difficult to achieve [118]. A different approach consists in using noble metals (such as Au, Ag etc.) to make TCEs. However, such materials are intrinsically opaque for light due to their high plasma frequency, and therefore, one has to structure these metals in various shapes to make them transparent within a certain frequency window [119], [120]. However, structuring may decrease the mechanical stability and electric conductivity of a metallic contact layer, what is undesired in practical applications. In addition, most previous efforts have been devoted to making free-standing TCEs, but in many real applications such as solar cells, the TCEs should function being deposited on a substrate, generally silicon (Si). In this case, the substrate itself having a high refractive index may induce substantial reflections, which should be avoided in applications. Therefore, it is highly desired to consider realistic geometry when designing TCEs.

In the following chapter we describe a simple scheme to make a metallic film on a semi-infinite substrate optically transparent, thus obtaining a completely transparent electrode in a desired frequency range.

4.4.1 Analytical and numerical model

Our scheme is inspired by early work [121] showing that an optically opaque layer (with a negative permittivity ε) can be perfectly transparent when sandwiched between two carefully designed MM layers. The physics behind obtaining the transparency is the cancellation of the scattering from the target opaque layer by carefully choosing the material and geometrical parameters of those two MM layers. In the present problem, considering a continuous metal film C (with negative relative permittivity ε_C) on top of a semi-infinite substrate with relative permittivity ε_{sub} , our aim is to transmit in the most effective way electromagnetic waves through the C layer inwards the semi-infinite substrate, as illustrated in Fig. 4.18.

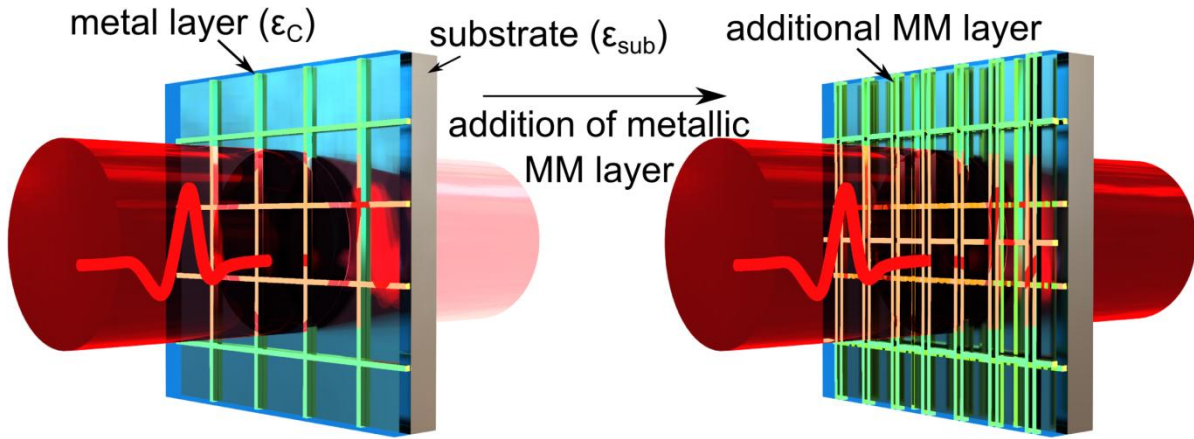


Figure 4.18: Transparent metallic electrode. Addition of a metallic MM layer on top of an opaque electrode, leads to a transparency of the whole structure.

To achieve a transparent metallic electrode we purposely placed a composite layer consisting of alternate A and B stripes (denoted as an AB layer) on top of the metallic C layer, as shown in Fig. 4.19.

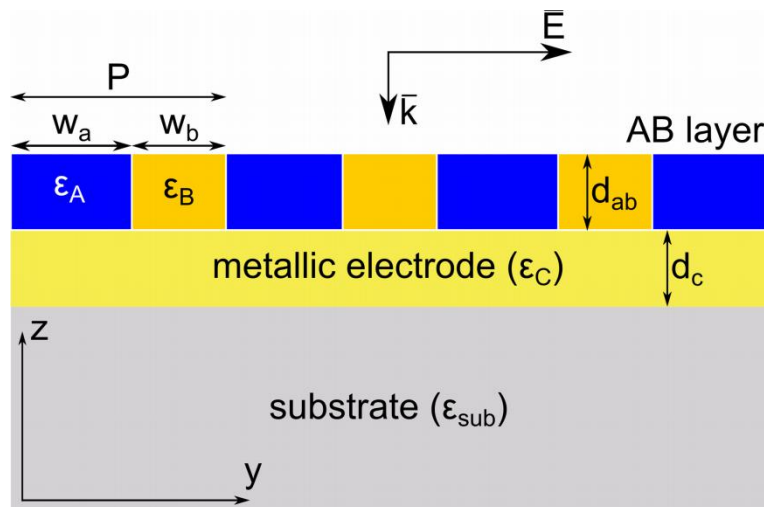


Figure 4.19: Schematic illustration of the proposed structure.

As shown in Fig. 4.19 the width of the strips A and B are respectively denoted by w_a and w_b , and the periodicity of layer AB is $P = w_a + w_b$. Meanwhile, the thicknesses of layers AB and C are respectively d_{ab} and d_c .

To illustrate how the idea works, we performed full-wave numerical simulations based on the finite element method with COMSOL (Multisphysics) to investigate the electromagnetic

wave transmittance as functions of ε_B and P/λ . The results are depicted in Fig. 4.20 with all other parameters fixed at the following values: $\varepsilon_A = \varepsilon_{sub} = 12$, $\varepsilon_C = -40$, $w_B = 0.1\lambda_0$, $d_{AB} = d_C = 0.02\lambda_0$, where λ_0 is the wavelength of incident light in free space. In our calculations we fixed w_B and vary w_A to change P .

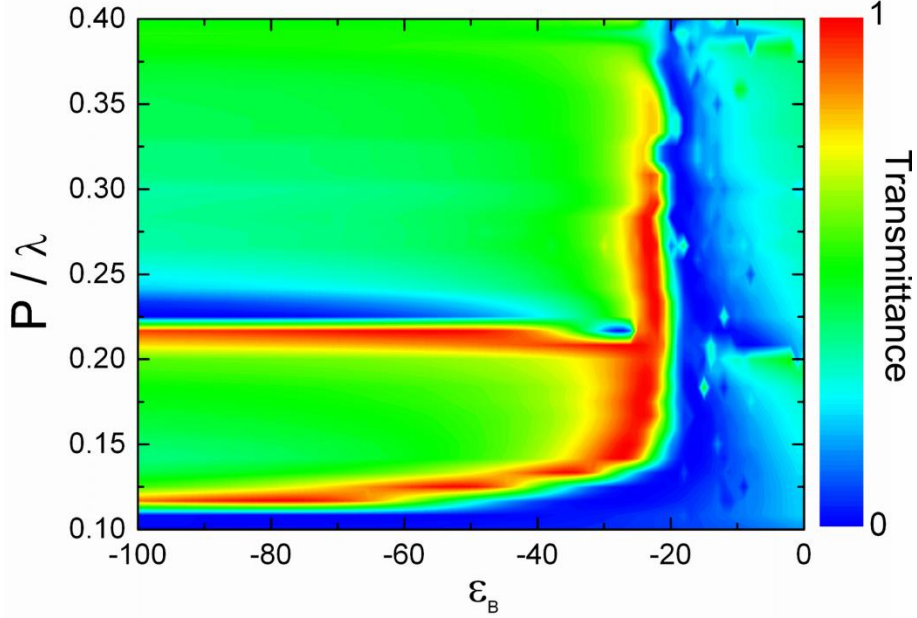


Figure 4.20: Transmittance as the function of ε_B and P/λ . All other parameters are fixed.

According to the transmittance diagram depicted in Fig. 4.20, we find that the entire system becomes perfectly transparent when the geometrical and material parameters satisfy certain conditions. This is quite surprising at first glance, since the transmittance of a standing-alone metallic C layer on the substrate is only $\sim 20\%$. However, with an additional AB layer put on its top, we can identify two main electromagnetic bands with transmittance values close to 100%.

We find that the discovered transparency phenomenon can be explained by the scattering cancellation mechanism in the same spirit as in [121]. Since the transparency region is where $P \ll \lambda_0$, we homogenize the composite AB layer based on the effective medium theory [122]. Such approximation greatly simplifies our considerations but helps capture the main physics. In the long wavelength limit, for the particular polarization $E \parallel y$ (see Fig. 4.19), the effective permittivity of the AB layer can be obtained by:

Chapter 4
Terahertz Metamaterials

$$\frac{1}{\varepsilon_{AB}} = \frac{1}{\varepsilon_A} \cdot \frac{w_A}{P} + \frac{1}{\varepsilon_B} \cdot \frac{w_B}{P}. \quad (4.9)$$

We can then employ the transfer-matrix-method to analytically calculate the transmittance/reflectance coefficients through the whole layered structure, e.g. air/AB/C/substrate.

$$\begin{pmatrix} t \\ 0 \end{pmatrix} = Q \begin{pmatrix} 1 \\ r \end{pmatrix}, \quad (4.10)$$

where $t = Q_{11} - Q_{12}Q_{21}/Q_{22}$ and $r = -Q_{21}/Q_{22}$ are respectively the transmittance and reflectance coefficients, and Q is the 2 x 2 scattering matrix of the system. In the ideal lossless case perfect transparency corresponds to zero reflectance, i.e., $Q_{21} = 0$. Therefore, analysis of function Q_{21} will give us some directions for achieving transparency. Through straightforward but tedious calculations, we found that:

$$\begin{aligned} Q_{21} = & \left(1 - \frac{1}{\sqrt{\varepsilon_{sub}}} \right) + i \left(\frac{1}{\sqrt{|\varepsilon_C|}} + \frac{\sqrt{|\varepsilon_C|}}{\sqrt{\varepsilon_{sub}}} \right) \tanh(\sqrt{|\varepsilon_C|}d_C/\lambda_0) \dots \quad (a) \\ & + i \left(\frac{1}{\sqrt{\varepsilon_{AB}}} - \frac{\sqrt{|\varepsilon_C|}}{\sqrt{\varepsilon_{AB}}\sqrt{\varepsilon_{sub}}} \right) \tan(\sqrt{\varepsilon_{AB}}d_{AB}/\lambda_0) \dots \quad (b) \\ & - \left(\frac{\sqrt{\varepsilon_{AB}}}{\sqrt{|\varepsilon_C|}} + \frac{\sqrt{|\varepsilon_C|}}{\sqrt{\varepsilon_{AB}}\sqrt{\varepsilon_{sub}}} \right) \tan(\sqrt{\varepsilon_{AB}}d_{AB}/\lambda_0) \tanh(\sqrt{|\varepsilon_C|}d_C/\lambda_0) \quad (c) \end{aligned} \quad (4.11)$$

All terms in Eq. (4.11) have clear physical interpretations. The first two terms (a) represent scattering from the semi-infinite substrate and the C layer, respectively. The third term (b) is contributed by the AB layer. Finally the forth term (c) results from multiple scattering in all layers. It is obvious from Eq. (4.11) that the presence of the AB layer can generate additional scattering terms (b,c) to cancel those contributed by the C layer and the semi-infinite substrate (a). Function Q_{21} is complex having both real and imaginary parts. Therefore, satisfying condition $Q_{21} = 0$ by tuning only one parameter ε_{AB} is not guaranteed. To

understand the transmittance diagram presented in Fig. 4.20, we relax the perfect transparency condition. Instead of solving equation $Q_{21} = 0$ accurately, we vary parameter w_A , while keeping all other parameters fixed, to find the solutions that minimize quantity $|Q_{21}/Q_{22}|$. In this analysis we can omit Q_{22} since it is a smooth function of w_A with very large values, so the important parameter determining the reflectance is apparently Q_{21} . The solutions obtained by the minimization procedure are depicted in Fig. 4.21 with the open circles.

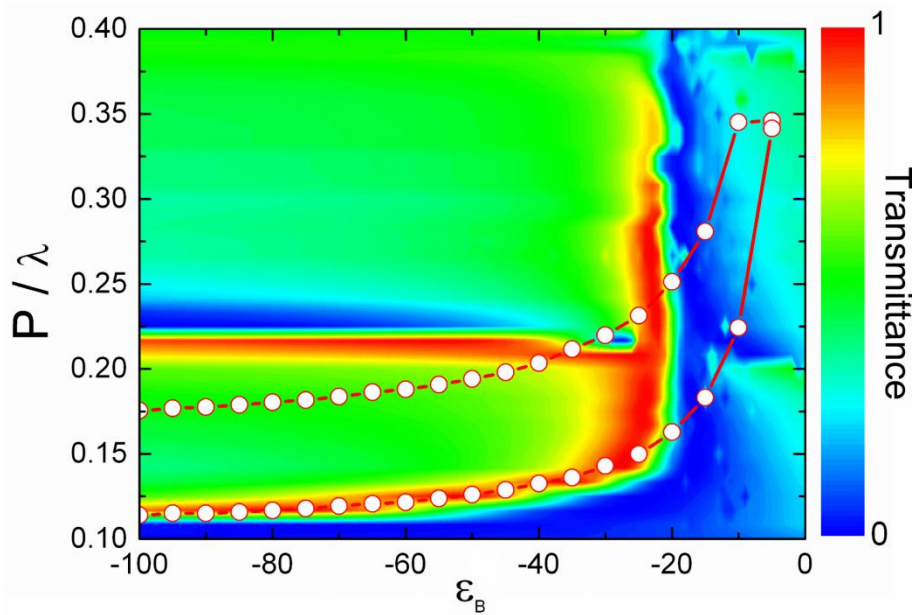


Figure 4.21: Transmittance as the function of ε_b and P/λ . (open circle) solutions of Eq. (4.11) obtained by the minimization procedure.

As shown in Fig. 4.21 we find that the finite element method simulated transparency bands match quite well with the minimization model results, indicating that the present discovered transparency is indeed governed by the scattering cancellation mechanism. Specifically, adjusting parameter w_A can efficiently modulate the scattering from the AB layer so that the reflectance from the system is minimized, leading to the significantly enhanced electromagnetic wave transmittance.

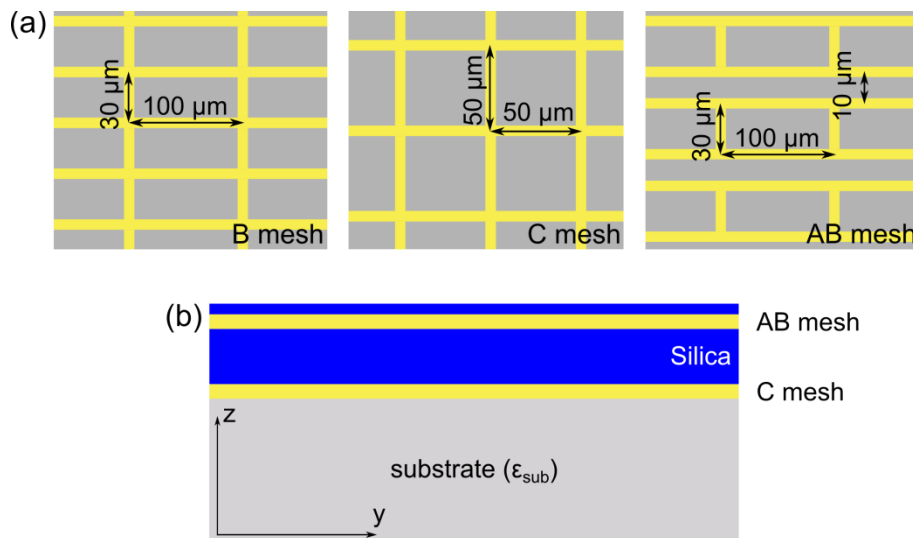
The discrepancies between the full-wave simulations and model results are found mainly for the upper branch and in the right part of the graph. It is easily understandable since in these regions the structure cannot be considered deeply sub-wavelength, so that the effective medium description (Eq. (4.9)) of the AB layer is not correct anymore. It is interesting to note

that, while the effective medium model considerations do not guarantee the existence of perfect transparency, the full-wave simulations on realistic structures show that the maximized transmittance in each case can indeed be almost 100 %.

4.4.2 Design

Although the illustrative example presented above is very particular, our approach can be expanded to any parameter set due to the generality of the involved formulae. Once the C layer properties are known, the AB-layer parameters can be deduced. Also, the concept is applicable to any electromagnetic frequency domain as long as the required material parameters can be realized. The most natural applications of our design are in the visible domain, where the permittivities of plasmonic metals are in the desired region (see Fig. 4.20). Nevertheless, to verify the concept experimentally we decided to apply it in the THz domain to avoid notorious fabrication challenges of nanophotonics.

In the low THz region metals can be considered as almost perfect electric conductors. Their negative permittivities are typically much bigger in the absolute values than requested in Fig. 4.20. Therefore, we exploited the approach from [123] and mimicked plasmonic metals by designed THz MMs based on sub-wavelength metallic meshes (as diluted metals). The detailed configurations of the THz MM samples mimicking plasmonic metals B and C are shown in Fig. 4.22a. Each metallic line has width $4\ \mu\text{m}$ and thickness $200\ \text{nm}$. The vertical cross-section of the sample is shown in Fig. 4.22b.



Chapter 4 Terahertz Metamaterials

Figure 4.22: (a) schematics of AB and C meshes in the xy plane. (b) proposed structure in the yz plane.

The semi-infinite substrate is assumed as Si with $\epsilon_{Si} = 11.7$. The 12 μm thick silica layer (with $\epsilon_{SiO_2} = 3.85$ [124]) is considered as a spacer between the two metallic meshes. A 200 nm thick silica layer is placed on the very top for protection.

Due to the presence of a non-terminated metallic mesh, we assume that such MMs can be assigned with a Drude-like behavior, similar to the diluted metal concept [123]. In order to retrieve their effective permittivities we first performed finite-difference time-domain simulations to get the transmittance spectra. Then we fitted the simulation results with the Drude model. It resulted that the permittivities of the C and B meshes can be respectively described by $\epsilon_C = 3.85 - (4.98/f)^2$ and $\epsilon_B = 3.85 - (4.98^2/f^2)$, with f denoting the frequency in THz. For the $f = 0.6$ THz these formulae give us $\epsilon_C \sim -65$ and $\epsilon_B \sim -22$, indicating that designed MMs can indeed mimic plasmonic metals with the negative values of permittivity being in the desired range.

The next step is to design the AB layer (Fig. 4.22a,b). Since the mesh B has the lattice constant of 30 μm along the y-axis, we must take the width w_B of stripe B as $n \times 30 \mu\text{m}$ with n as integer when designing the AB layer. Otherwise the stripes B may not have the same properties as the original B mesh. Taking material A as silica, we set the widths of stripes A and B as $w_A = 10 \mu\text{m}$ and $w_B = 30 \mu\text{m}$ (see Fig. 4.19). The AB layer thus obtained is placed on top of the C layer and we obtain the final design shown in Fig. 4.22b. Through comparing the transmission spectra calculated with a homogenous effective-medium slab and full-wave simulations on the realistic AB structure, we found that the effective permittivity of the AB layer can be given by $\epsilon_{AB} = 3.85 + 4.19/(0.74^2 - f^2)$. The resonance behavior of ϵ_{AB} ensures that there must be a frequency where it exhibits the desired value to make the whole structure transparent.

We performed FDTD simulations based on realistic material parameters to study the transmittance spectrum $T = |S_{21}|^2$ through the designed structure. In our calculations all materials are assumed to be non-magnetic ($\mu = \mu_0$), and the dielectric function of aluminum is described using the Drude model with parameters from [125]. The transmittance spectra

obtained by FDTD simulations of the silicon substrate with C layer and both C and AB layers (device) are presented in Fig. 4.23.

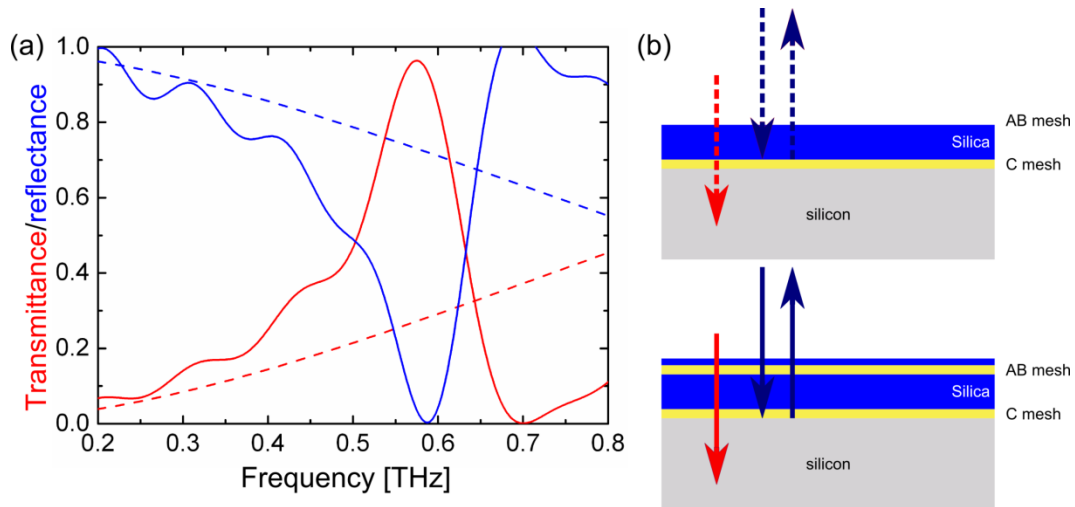


Figure 4.23: (a) simulated transmittance (red curves) and reflectance (blue curves) spectra of C-layer (dashed curves) and AB/C-layers (solid lines) deposited on the silicon substrate. (b) illustration of simulated geometries.

In the case of a bare silicon substrate of 530 μm thickness the calculated transmittance is $\sim 70\%$. As expected, the C layer greatly diminishes the transmittance down to $\sim 30\%$ at 0.57 THz. However, by putting the AB layer on top of the C layer we can reach almost 100% transmittance at 0.57 THz as shown in Fig. 4.23a. It is worth noting that the incident wavelength is roughly 40 times larger than the thickness of the AB layer + silica ($\sim 12.7\mu\text{m}$). Yet, by appropriately adjusting the material and geometric parameters of such thin AB/silica layer, we can make its scattering strong enough to completely compensate the scattering from the C layer, leading to nearly perfect transparency. The entire device thus combines high optical transmittance with good in-plane electric conductivity, which is highly desired in many optoelectronic applications.

4.4.3 Fabrication

The transparent electrodes were fabricated on top of a high-resistivity silicon wafer. The choice for this substrate was due to its high transmission at the low THz frequencies, thus allowing a good signal-to-noise ratio. The fabrication flow is presented schematically in Fig. 4.24.

Chapter 4 Terahertz Metamaterials

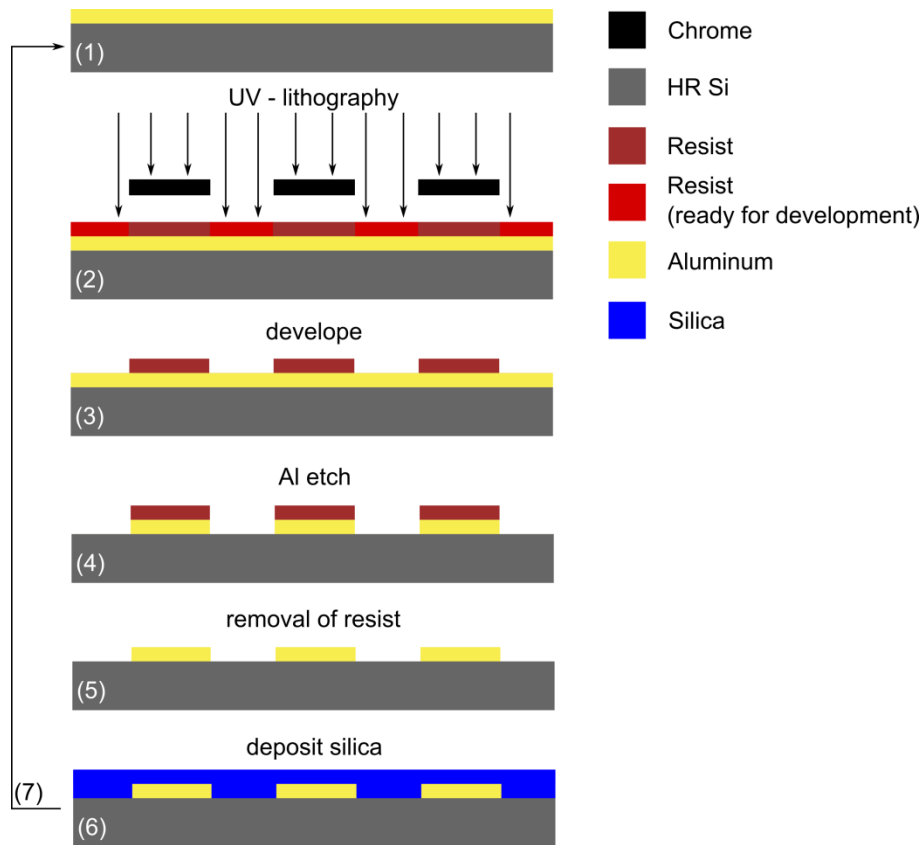


Figure 4.24: Schematic of the fabrication procedure of transparent electrodes.

The first step consists in depositing 200 nm of aluminum (Al) is deposited on top of the high resistivity silicon wafer (Fig. 4.24, step 1). This layer is the one where the metallic mesh will be etched in.

Next, the deposition, exposure and development of the photosensitive polymer that acts as an etching mask is performed. Since the resolution of the structure is in the order of microns, the optical lithography was the choice for exposing the structure (Fig. 4.24, steps 2,3). At this point, the mesh is defined in polymer and, using dry metal etching in plasma of HBr and Cl₂ we transferred the pattern to the metal beneath (Fig. 4.24, step 4). We decided to use the etching technique instead of the more widely spread lift-off one in order to have better control over the structures geometrical dimension. The dry etching was performed with an inductive coupled plasma reactive ion etching (ICP-RIE) machine. The etching starts with a 20 seconds breakthrough step for removing native Al₂O₃ made at a Cl₂ flow of 20 sccm with a platen power of 120 W and a coil power of 600 W. The next step, the etching of the Al layer, is made in a mixture of Cl₂/HBr 25/15 sccm with platen and coil powers of 100 W and

Chapter 4 Terahertz Metamaterials

500 W respectively. The etching time is 1 minute. After the etching of the Al layer, a 5 minutes O_2 plasma etching is performed in order to remove the photoresist mask (Fig. 4.24, step 5). At this point, the first layer is fabricated.

The next step is the deposition of silica using a plasma enhanced chemical vapor deposition (PECVD) machine. Using an atmosphere of $SiH_4/N_2O/N_2$ maintained by a constant flow of 12/1420/392 sccm respectively at 550 mtorr pressure and power of 60 W, we deposited 12.5 μm of silica on top of the mesh layer (Fig. 4.24, step 6 and Fig. 4.25a). In order to obtain as high transmission as possible, the thickness of silica needs to be very well controlled thus, before the deposition, several tests were made to ensure the correct reading of the deposition rate, uniformity and stability. The deposition rate was of 81 nm/min with less than 1 % uniformity thus making a deposition time of ca. 2h30min for the 12.5 μm thick silica layer.

Once the silica layer is deposited, the first steps are repeated with the only difference of having to align the second exposure to the first one (Fig. 4.24, step 7 and Fig. 4.25b). The last fabrication step consists in depositing a thin 200 nm silica layer on top of the structure using the same recipe as for the initial 12.5 μm spacer.

The fabrication results of the first C-layer and AB/C-layers are shown in Fig. 4.25.

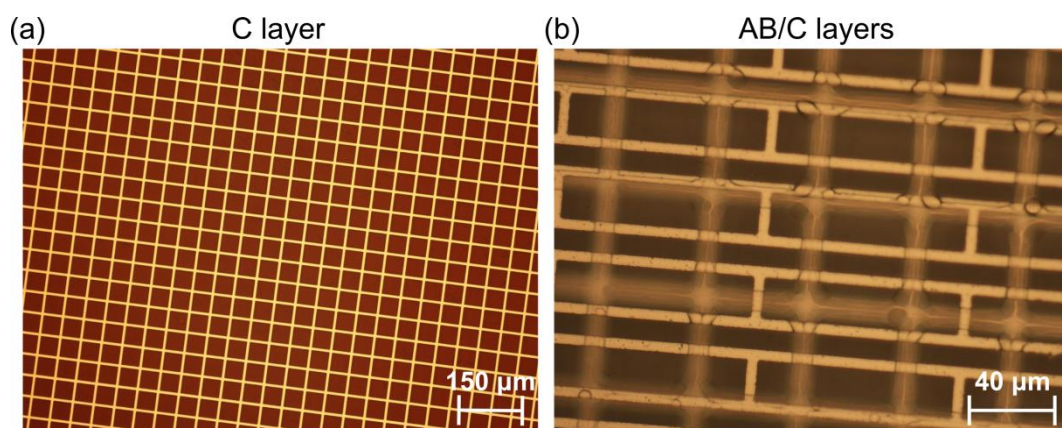


Figure 4.25: Optical images of fabrication results. (a) C-layer on top of high resistivity silicon wafer. (b) top AB-layer. The shadow of the bottom C-layer can be distinguished in the background.

As shown in Fig. 4.25 the metallic meshes for both layers were well defined on a large scale. No larger defects were observed during the inspection with an optical microscope.

4.4.4 Characterization

We characterized the fabricated samples using a T-Ray 4000 THz time-domain spectroscopy system. For every sample 10.000 waveforms were recorded with the scan rate of 100 Hz and the average of all the waveforms was then used for further investigation. For further details on T-Ray 4000 THz time-domain spectroscopy system see section 1.2.

Due to multiple reflections in the Si substrate the main pulse is closely followed by ripples from multiple reflections in the thin silica layer as shown in Fig. 4.26.

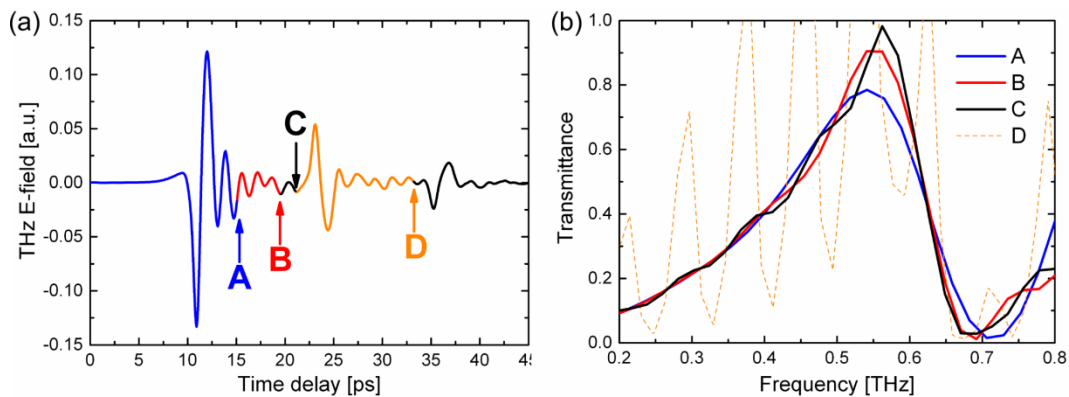


Figure 4.26: Measured transmittance of transparent electrodes by T-Ray 4000 THz-TDS system. (a) various pulse lengths and (b) their respective transmittance spectra, showing the importance of correctly defining the cutting time-point.

The THz transient signals were cut after careful analysis of the Fourier transformed spectra. A too short pulse cut leads to significant loss of transmitted intensity, see points A, B, C in Fig. 4.26a and corresponding transmittance spectra in Fig. 4.26b. On the other hand, in case of a too long pulse length (point D), the reflected signal from the back of the substrate causes huge Fabry-Perot oscillations that make the interpretation of the results difficult (see D line in Fig. 4.26b). Once the optimum cutting length was obtained, the reference signal is cut accordingly. The transmittance measurements were normalized to transmittance through the high resistivity silicon substrate with $12.5\ \mu\text{m}$ of silica characterized for referencing. The reflected signal was normalized to the one of an aluminum mirror, considered to be a perfect reflector ($|S_{11}|^2 \cong 100\%$) at THz wavelengths.

Figure 4.27 shows both normalized transmittance and reflectance spectra for the complete AB/C device and C mesh samples.

Chapter 4
Terahertz Metamaterials

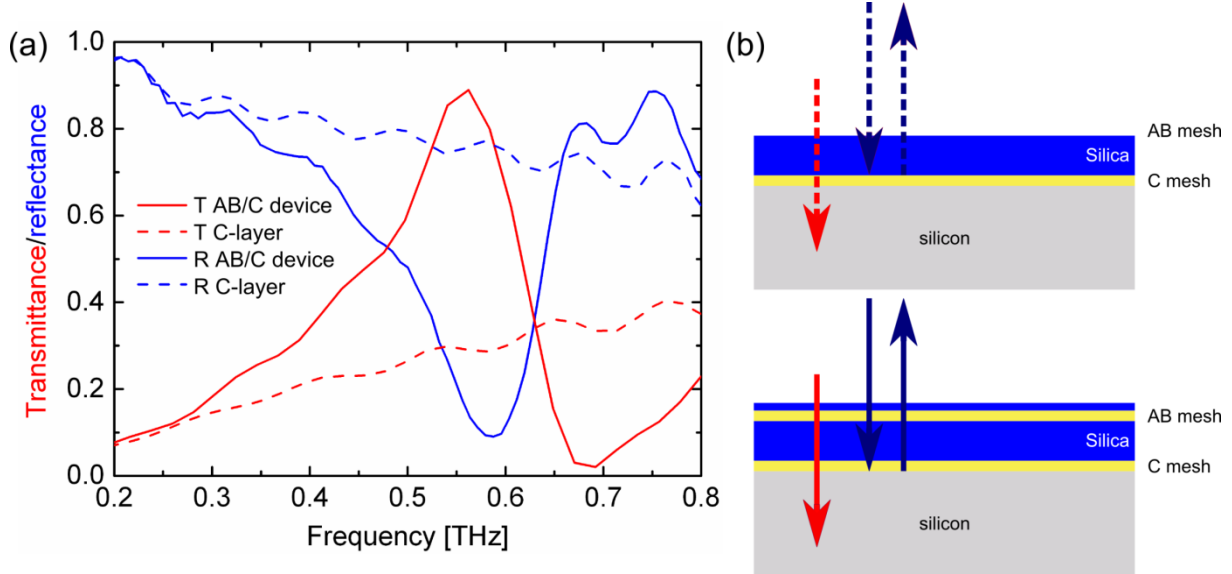


Figure 4.27: (a) transmittance (red) and reflectance (blue) for both the whole AB/C device (solid curves) and C-layer (dashed curves). The averaged data for four devices and two C-layer samples are presented. (b) illustration of measured geometries.

As expected quite low C mesh transmittance is greatly improved by cancelation of scattering with the help of the AB layer and reaches almost 90 % at the resonance frequency.

The direct comparison of numerical and measurement results displays an excellent agreement as shown in Fig. 4.28.

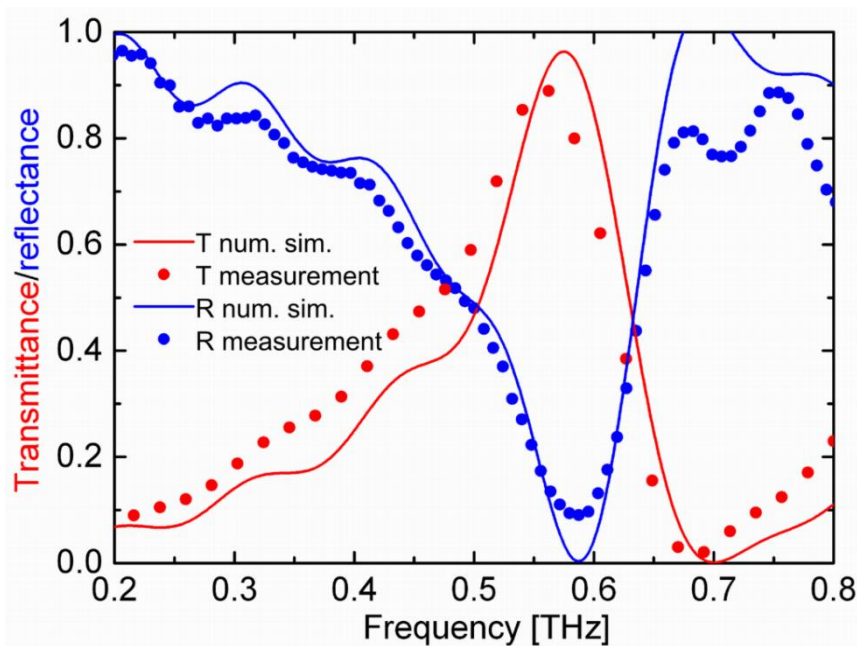


Figure 4.28: Transmittance (red curves) and reflectance (blue curves) data comparison between numerical (solid curved) and measurement (circles) results for AB/C device.

The insignificant quantitative deviations of results in Fig. 4.28 are mainly due to the difficulty of perfectly finding the optimum pulse cutting length in measurements. Because of the inherent noise in the spectra and slight variations in the silicon substrate thickness we cut the time domain signal at a different time-point than in simulation. Another factor that affects the transmission is the possible losses in the silica layer. The slight frequency shifts of ~ 20 GHz in the transmission peak position can be attributed to fabrication imperfections.

4.5 Conclusion

In this chapter we have presented modelling, fabrication and characterisation results of three different THz devices based on metamaterials:

- Polarization sensitive fractal planar metamaterial (section 4.2)

We presented a fractal metamaterials with strong polarization filtering properties. An excellent agreement between theoretical and experimental results has been shown. One of the main characteristics of this design is its tunability by design: by simply changing the length of the fractal elements one can choose the operating frequency window. Additionally we presented novel process for fabricating high aspect ratio, freestanding, patterned, 2 μm -thick nickel films.

- Optically active planar metamaterial for polarization manipulation (section 4.3)

We have fabricated and characterized a terahertz anisotropic Babinet-inverted dimer MM following the same recipe, for patterned 2 μm -thick nickel membrane suspended in air, as for fractal metamaterials (section 4.2.2). We find very good agreement between the design and the fabricated dimensions. Despite its relative simplicity, our V-shaped slot design shows optical activity comparable with two and three dimensional chiral materials, reaching a maximum of approximately $500^\circ/\lambda$ at 0.53 THz, and a polarization conversion difference between left-to-right and right-to-left circular polarization of approximately 65 % in the range between 0.49 and 0.52 THz.

- Optically transparent metallic electrodes based on MMs (section 4.4)

Chapter 4 Terahertz Metamaterials

By placing a composite layer consisting of dielectric and metallic stripes on top of the metallic one, we found that the back-scattering from the metallic film can be almost perfectly canceled by the composite layer under certain conditions, leading to transparency of the whole structure. We performed proof-of-concept experiments in the terahertz domain to verify our theoretical predictions, using carefully designed metamaterials to mimic plasmonic metals in optical regime. Experiments are in excellent agreement with full-wave simulations. As expected quite transmittance of metallic electrode (30 %) is greatly improved by cancelation of scattering with the help of the composite layer and reaches almost 90 % at the resonance frequency.

5 Conclusion and outlook

This thesis has been dealing with three different terahertz time-domain spectroscopy systems (THz-TDS) for characterization of both linear and non-linear optical properties of chalcogenide glasses. Additionally several design of devices for THz radiation manipulation has been evaluated, fabricated and characterized.

During the characterization of chalcogenide glasses at THz frequencies, several important observations were done. By the use of ultrabroadband THz-TDS system where THz pulse is generated in induced gas plasma, we have observed a transition from disorder response of the glasses to medium- and long-range order response, namely Ioffe-Regel transition. The Ioffe-Regel transition occurs when the mean free path between scattering events of acoustic plane waves propagating in the material approaches the wavelength of the plane wave. At wavelengths longer than this length, scattering will be the dominant loss factor and result in a universal (monotonous) behavior of the absorption coefficient. At shorter wavelengths, plane-wave propagation dominates. Here we directly observe this transition from disorder-induced loss to a collective response mediated by medium- and long-range order of the glass. For As_2S_3 and GaLaS glasses, this transition took place at 4-5 THz and 6-7 THz respectively. Besides the highly complex dispersion profiles for both glasses, another unexpected observation was made. Two transparency windows have been identified in As_2S_3 glass at frequencies 7.2-8.5 and 12-13 THz. Can those windows be tuned by changing the composition of chalcogenide samples?

Chalcogenide glasses are well known for their very high third-order (Kerr) nonlinearity. During our investigation of their non-linear behavior induced by a highly intense THz pulse generated in a LiNbO_3 crystal, we observed a rapid third-order non-linear dynamics (Kerr effect) in both As_2S_3 and As_2Se_3 bulk samples. By optical Kerr-gate sampling we measured the THz-induced nonlinear refractive indices at 800 nm to be $n_2 = 1.746 \cdot 10^{-14} \text{ cm}^2/\text{W}$ for As_2S_3 and $n_2 = 3.440 \cdot 10^{-14} \text{ cm}^2/\text{W}$ for As_2Se_3 . To our best knowledge this is the first observation of the THz-induced optical Kerr effect in a solid material. The observed ultrafast nonlinearities

in chalcogenide glasses and transparency windows can make them promising candidates for fast nonlinear THz devices.

We have evaluated, fabricated and characterized several different devices for THz radiation manipulation.

a) Terahertz antennas for field enhancement

Microscopic model of the THz field enhancement in a metal nanoslit have shown that the field enhancement in the subwavelength slit is proportional to $1/\omega$. By the use of ultraviolet lithography we fabricated THz antennas with a gap size span from approximately 800 nm to 2.5 μm . Numerical simulations predicted that such a span covers a field enhancement of approximately 40 – 90 times. We observed a dramatic ratio of electromigration of gold in the gap areas when the THz antennas were exposed high power THz pulse. To our surprise it was also possible to visualize the absolute value of the electric field pattern of THz antennas by scanning electron microscope, patterned by the residual layer of photoresist. These field patterns have revealed that THz antennas with a narrow gap behave similar to the ones with no gap, due to the high ratio of electromigration that connects the two metallic structures together.

b) Polarization sensitive fractal planar metamaterial

We presented a fractal metamaterials with strong polarization filtering properties. They were patterned by an original fabrication method that allows fabricating 2 μm thick nickel free standing films. Fractal metamaterials showed to possess 60 % field transmission at around 1 THz for TE polarized light while the TM waves have almost 80 % field transmission peak at 0.6 THz. One of the main characteristics of this design is its tunability by design: by simply changing the length of the fractal elements one can choose the operating frequency window. The presented fabrication flow is a versatile platform for other designs that are sensitive to thick substrates and we believe that due to the simple designs of fractal and Babinet-inverted metamaterials, it has a great potential to be integrated as a component in THz optical circuitry.

c) Optically active planar metamaterial for polarization manipulation

Conclusion and outlook

By utilizing the same fabrication processes as for fractal metamaterials we fabricated free-standing planar anisotropic Babinet-inverted metamaterial. Despite its relative simplicity, our V-shaped slot design shows optical activity comparable with two and three dimensional chiral materials, reaching a maximum of approximately $500 \text{ }^\circ/\lambda$ at 0.53 THz, and a polarization conversion difference between left-to-right and right-to-left circular polarization of approximately 65 % in the range between 0.49 and 0.52 THz. By optimizing the angle and distance between the rods even stronger circular polarization conversion may be achieved.

d) Optically transparent metallic electrodes based on MMs

The metal electrode transmittance can be improved by canceling the scattering from a metallic film with the help of a metamaterial-inspired composite layer on top of the structure. We performed proof-of-concept experiments in the terahertz domain to verify our theoretical predictions, using carefully designed metamaterials to mimic plasmonic metals in optical regime. Experiments are in excellent agreement with full-wave simulations. As expected quite transmittance of metallic electrode (30 %) is greatly improved by cancelation of scattering with the help of the composite layer and reaches almost 90 % at the resonance frequency. This approach, although demonstrated here for the THz regime, can be extended to other important frequency domains, e.g. the visible range, where demanding applications of transparent electrodes in photovoltaic cells, touch screens and other display devices exist. The design proposed here is only applicable to one particular in-plane electric field polarization; however it can be easily generalize to exhibit in-plane isotropic properties.

Ph.D. Publications

6 Ph.D. Publications

6.1 Publications related to this thesis

Peer-reviewed journals

- | | | |
|------|---|---|
| 2013 | Terahertz induced Kerr effect in amorphous chalcogenide glasses
<u>M. Zalkovskij</u> , A. C. Strikwerda, K. Iwaszczuk, A. Popescu, D. Savastru, R. Malureanu, A. V. Lavrinenko and P. U. Jepsen | Submitted to Applied Physics Letters |
| 2013 | Optically active Babinet planar metamaterial film for terahertz polarization manipulation
<u>M. Zalkovskij</u> , R. Malureanu, C. Kremers, D. N. Chigrin, A. Novitsky, S. Zhukovsky, P. T. Tang, P. U. Jepsen and A. V. Lavrinenko | Laser and Photonics Review, 7 , p810-817 |
| 2012 | Ultrabroadband terahertz spectroscopy of chalcogenide glasses
<u>M. Zalkovskij</u> , C. Z. Bisgaard, A. Novitsky, R. Malureanu, D. Savastru, A. Popescu, P. U. Jepsen, and A. V. Lavrinenko | Applied Physics Letters, 100 , 031901 |
| 2012 | A new method for obtaining transparent electrodes
R. Malureanu*, <u>M. Zalkovskij</u> *, Z. Song*, C. Gritti, A. Andryieuski, Q. He, L. Zhou, P. U. Jepsen, and A. V. Lavrinenko (*equal contribution) | Optics Express, 20 , p22770-22782 |
| 2011 | Microscopic model of the THz field enhancement in a metal nanoslit
A. Novitsky, <u>M. Zalkovskij</u> , R. Malureanu and A. Lavrinenko | Optics Communications, 284 , p5495-5500 |

Peer-reviewed conference contributions

- | | | |
|------|--|---|
| 2013 | Metamaterials and Metasurfaces in THz Applications
A. Lavrinenko, R. Malureanu, <u>M. Zalkovskij</u> , P. U. Jepsen, A. Novitsky, S. Zhukovsky, A. Andriueyski, D. N. Chigrin, C. Kremers, Z. Y. Song, Q. He, and L. Zhou | The International Conference on Coherent and Nonlinear Optics (ICONO), June 18-22, Moscow, Russia (invited talk by A. Lavrinenko) |
| 2013 | Fabrication and characterization of transparent metallic electrodes in the terahertz domain
<u>M. Zalkovskij</u> , R. Malureanu, Z. Song, C. Gritti, A. Andryieuski, Q. He, L. Zhou, P. U. Jepsen, and A. V. Lavrinenko | International Workshop on Terahertz Science and Technology 2013, April 1-5, Kyoto, Japan (poster presentation by M. Zalkovskij) |
| 2013 | Transparent electrodes in the terahertz regime – a new approach
R. Malureanu*, Z. Song*, <u>M. Zalkovskij</u> *, C. Gritti, A. Andryieuski, Q. He, L. Zhou, P. U. Jepsen and A. V. Lavrinenko (*equal contribution) | 4th International Conference on Metamaterials, Photonic Crystals and Plasmonics, March 18-22, Sharjah, UAE (invited talk by R. Malureanu) |
| 2012 | A new mechanism to design transparent electrodes: THz realizations
Z. Song*, R. Malureanu*, <u>M. Zalkovskij</u> *, C. Gritti, A. Andryieuski, Q. He, P. U. Jepsen, A. V. Lavrinenko, and L. Zhou. (*equal contribution) | The International Workshop on Metamaterials (Meta12). October 8-12, Nanjing, China, (published paper, ISBN: 978-1-4673-2807-4). |

Ph.D. Publications

- 2012 Anisotropic anti-rod dimer metamaterial film for terahertz polarization manipulation
M. Zalkovskij, R. Malureanu, A. Novitsky, P. U. Jepsen, A. V. Lavrinenko, C. Kremers and D. N. Chigrin
The 37th International Conference on Infrared, Millimeter and Terahertz Waves, September 23-28, Wollongong, Australia (oral presentation by M. Zalkovskij)
- 2012 Passive THz metamaterials
A.V. Lavrinenko, R. Malureanu, M. Zalkovskij, P.U.Jepsen, A. Novitsky, D. N. Chigrin, C. Kremers, Z. Y. Song, Q. He and L. Zhou,
The 6th International Congress on Advanced Electromagnetic Materials in Microwaves and Optics, September 17-22, St. Petersburg, Russia, (invited talk by A. Lavrinenko, published paper p.451-453, ISBN 978-952-67611-2-1).
- 2012 Metamaterials modelling, fabrication and characterisation techniques
R. Malureanu, M. Zalkovskij, A. Andryieuski, A. Novitsky, A. Ivinskaya, P.U. Jepsen, A. Popescu, D. Savastru, C. Kremers, D. Chigrin and A. V. Lavrinenko
The 6th International Conference Advanced Topics in Optoelectronics, Microelectronics and Nanotechnologies, August 23-26, Constanta, Romania (keynote by R. Malureanu).
- 2012 Fabrication and characterization of terahertz anisotropic anti-rod dimer planar metamaterials
M. Zalkovskij, R. Malureanu, A. Novitsky, P. U. Jepsen, A. V. Lavrinenko, C. Kremers and D. N. Chigrin
Proceedings of 3rd EOS Topical Meeting on THz Science and Technology, , June 17-20, Prague, Czech Republic (oral presentation by M. Zalkovskij)
- 2012 Ultrabroadband THz spectroscopic investigation of As₂S₃
M. Zalkovskij, R. Malureanu, A. Novitsky, D. Savastru, A. Popescu, A. V. Lavrinenko and P. U. Jepsen
Proceedings of CLEO 2012, the Conference on Laser and Electro-Optics, May 6-11, San Jose, USA (oral presentation by M. Zalkovskij, published paper)
- 2011 Wavelength-independent field enhancement in subwavelength gratings
A. Ivinskaya, A. Novitsky, D. Shyroki, M. Zalkovskij, R. Malureanu and A.V. Lavrinenko
The Fifth International Congress on Advanced Electromagnetic Materials in Microwaves and Optics, October 10-15, Barcelona, Spain (published paper)

None-peer-reviewed conference contributions

- 2013 Terahertz wave manipulation with metamaterials based on metal and graphene
A. Andryieuski, R. Malureanu, M. Zalkovskij, S. Zhukovsky, C. Gritti, A. Novitsky, D. Markovich, D. Chigrin, P. U. Jepsen and A. V. Lavrinenko
Days on Diffraction, May 27-31, Saint Petersburg, Russia (invited talk by A. Andryieuski)
- 2011 Two-dimensional fractal metamaterials for applications in THz
R. Malureanu, P. U. Jepsen, M. Zalkovskij, A. V. Lavrinenko, S. Xiao and L. Zhou
13th International Conference on Transparent Optical Networks, June 26-30, Stockholm, Sweden (published paper)
- 2011 Ultrabroadband THz spectroscopy of disordered materials
M. Zalkovskij, R. Malureanu, A. V. Lavrinenko and P. U. Jepsen
Proceedings of the 1st International Symposium on Terahertz Nanoscience, November 24-29, Osaka, Japan (invited talk by P. U. Jepsen, published paper)

Ph.D. Publications

- 2011 Characterization of arsenic tri-sulfide optical properties at broadband terahertz frequencies
M. Zalkovskij, C. Z. Bisgaard, A. Novitsky, R. Malureanu, D. Savastru, A. Popescu, P. U. Jepsen, and A. V. Lavrinenko
Danish Physical Society, Annual Meeting, June 22, Nyborg, Denmark (poster presentation by P. U. Jepsen)

6.2 Publications unrelated to this thesis

Peer-reviewed journals

- 2013 Metamaterial Polarization Converter Analysis: Limits of Performance
D. Markovich, A. Andryieuski, M. Zalkovskij, R. Malureanu and A. V. Lavrinenko
Applied Physics B: Lasers and Optics, DOI 10.1007/s00340-013-5383-8
- 2012 Non-resonant terahertz field enhancement in periodically arranged nanoslits
A. Novitsky, A. M. Ivinskaya, M. Zalkovskij, R. Malureanu, P. U. Jepsen, and A. V. Lavrinenko
Journal of Applied Physics, **112**, 074318
- 2012 Optical waveguide mode control by nanoslit-enhanced terahertz field
A. Novitsky, M. Zalkovskij, R. Malureanu, P. U. Jepsen, and A. V. Lavrinenko
Optics Letters, **18**, p3903-3905
- 2010 Controlled Ag electroless deposition in bulk structures with complex three-dimensional profiles
R. Malureanu, M. Zalkovskij, A. Andryieuski and A. V. Lavrinenko
Journal of Electrochemical Society, **157**, p284-288

Peer-reviewed conference contributions

- 2014 High Transmittivity Half Wavelength Device for the Terahertz Regime
R. Malureanu, W. Sun, M. Zalkovskij, Q. He, L. Zhou, P. U. Jepsen, A. Lavrinenko
SPIE Photonic West, February 1-6, San Francisco, USA (invited talk by R. Malureanu)
- 2013 Ultrafast terahertz dynamics in bulk and nanostructured materials
P. U. Jepsen, D. G. Cooke, K. Iwaszczuk, A. Strikwerda, P. Klarskov, and M. Zalkovskij
2013 MRS Fall Meeting & Exhibit, December 1-6, Boston, USA (oral presentation by P. U. Jepsen)
- 2013 Terahertz-field-induced photoluminescence of nanostructured gold films
K. Iwaszczuk, R. Malureanu, M. Zalkovskij, A. C. Strikwerda and P. U. Jepsen
The 38th International Conference on Infra red, Millimeter and Terahertz Waves, September 1-6, Mainz, Germany (oral presentation by K. Iwaszczuk)
- 2013 Terahertz cross-phase modulation of an optical mode
A. Lavrinenko, A. Novitsky, M. Zalkovskij, R. Malureanu and P. Jepsen
Proceedings of CLEO 2013, the Conference on Laser and Electro-Optics, June 9-14, San Jose, USA (oral presentation by A. Lavrinenko)
- 2013 3D terahertz beam profiling
SPIE Photonic West, February 2-7, San Francisco, USA (oral presentation by P.

Ph.D. Publications

- P. K. Pedersen, A. Strikwerda, T. Wang, M. Zalkovskij and P. U. Jepsen
Pedersen, published paper)
- 2012 Light modulation abilities of nanostructures
A. V. Lavrinenko, V. E. Babicheva, A. Novitsky, M. Zalkovskij, R. Malureanu, P. U. Jepsen, I. V. Kulkova and K. Yvind
TaCoNa-2012, October 24-26, Bad-Honnef, Germany, (invited talk by A. Lavrinenko, published paper, **1475**, p.25-27).
- 2011 Fabrication and characterization of woodpile structures
M. Zalkovskij, R. Malureanu, A. Andryieuski and A.V. Lavrinenko
Proceedings of SPIE, the International Society for Optical Engineering (published paper)

7 Bibliography

- [1] J. Fitzgerald, E. Berry, N. N. Zinovev, G. C. Walker, M. a Smith, and J. M. Chamberlain, "An introduction to medical imaging with coherent terahertz frequency radiation.," *Physics in medicine and biology*, vol. 47, no. 7, pp. R67–84, Apr. 2002.
- [2] J. Fitzgerald, E. Berry, N. N. Zinov'ev, S. Homer-Vanniasinkam, R. E. Miles, J. M. Chamberlain, and M. a Smith, "Catalogue of human tissue optical properties at terahertz frequencies.," *Journal of biological physics*, vol. 29, no. 2–3, pp. 123–8, Jun. 2003.
- [3] P. H. Siegel, "Terahertz Technology in Biology and Medicine," *IEEE Transactions on Microwave Theory and Techniques*, vol. 52, no. 10, pp. 2438–2447, Oct. 2004.
- [4] P. C. Ashworth, E. Pickwell-MacPherson, E. Provenzano, S. E. Pinder, A. D. Purushotham, M. Pepper, and V. P. Wallace, "Terahertz pulsed spectroscopy of freshly excised human breast cancer," *Optics Express*, vol. 17, no. 15, p. 12444, Jul. 2009.
- [5] V. P. Wallace, A. J. Fitzgerald, E. Pickwell, R. J. Pye, P. F. Taday, N. Flanagan, and T. Ha, "Terahertz pulsed spectroscopy of human Basal cell carcinoma.," *Applied spectroscopy*, vol. 60, no. 10, pp. 1127–33, Oct. 2006.
- [6] M. Brucherseifer, M. Nagel, P. Haring Bolivar, H. Kurz, a. Bosserhoff, and R. Büttner, "Label-free probing of the binding state of DNA by time-domain terahertz sensing," *Applied Physics Letters*, vol. 77, no. 24, p. 4049, 2000.
- [7] S. J. Kim, B. Born, M. Havenith, and M. Gruebele, "Real-time detection of protein-water dynamics upon protein folding by terahertz absorption spectroscopy.," *Angewandte Chemie (International ed. in English)*, vol. 47, no. 34, pp. 6486–9, Jan. 2008.
- [8] J. Federici and L. Moeller, "Review of terahertz and subterahertz wireless communications," *Journal of Applied Physics*, vol. 107, no. 11, p. 111101, 2010.
- [9] R. Piesiewicz, J. Jemai, M. Koch, and T. Kurner, "THz channel characterization for future wireless gigabit indoor communication systems," vol. 5727, pp. 166–176, Mar. 2005.
- [10] T. Kleine-Ostmann and T. Nagatsuma, "A Review on Terahertz Communications Research," *Journal of Infrared, Millimeter, and Terahertz Waves*, vol. 32, no. 2, pp. 143–171, Jan. 2011.
- [11] K. W. & D. M. Mittleman, "Metal wires for terahertz wave guiding," vol. 432, no. November, pp. 376–379, 2004.

Bibliography

- [12] M. Wächter, M. Nagel, and H. Kurz, “Metallic slit waveguide for dispersion-free low-loss terahertz signal transmission,” *Applied Physics Letters*, vol. 90, no. 6, p. 061111, 2007.
- [13] S. Maier, S. Andrews, L. Martín-Moreno, and F. García-Vidal, “Terahertz Surface Plasmon-Polariton Propagation and Focusing on Periodically Corrugated Metal Wires,” *Physical Review Letters*, vol. 97, no. 17, p. 176805, Oct. 2006.
- [14] N. Krumbholz, K. Gerlach, F. Rutz, M. Koch, R. Piesiewicz, T. Kürner, and D. Mittleman, “Omnidirectional terahertz mirrors: A key element for future terahertz communication systems,” *Applied Physics Letters*, vol. 88, no. 20, p. 202905, 2006.
- [15] D. L. Woolard, R. Brown, M. Pepper, and M. Kemp, “Terahertz Frequency Sensing and Imaging: A Time of Reckoning Future Applications?,” *Proceedings of the IEEE*, vol. 93, no. 10, pp. 1722–1743, Oct. 2005.
- [16] M. C. Kemp, P. F. Taday, B. E. Cole, J. A. Cluff, A. J. Fitzgerald, and W. R. Tribe, “Security applications of terahertz technology,” *Proceeding of SPIE*, vol. 5070, pp. 44–52, 2003.
- [17] W. L. Chan, J. Deibel, and D. M. Mittleman, “Imaging with terahertz radiation,” *Reports on Progress in Physics*, vol. 70, no. 8, pp. 1325–1379, Aug. 2007.
- [18] Y. C. Shen, T. Lo, P. F. Taday, B. E. Cole, W. R. Tribe, and M. C. Kemp, “Detection and identification of explosives using terahertz pulsed spectroscopic imaging,” *Applied Physics Letters*, vol. 86, no. 24, p. 241116, 2005.
- [19] J. F. Federici, B. Schulkin, F. Huang, D. Gary, R. Barat, F. Oliveira, and D. Zimdars, “THz imaging and sensing for security applications—explosives, weapons and drugs,” *Semiconductor Science and Technology*, vol. 20, no. 7, pp. S266–S280, Jul. 2005.
- [20] R. Huber, F. Tauser, a Brodschelm, M. Bichler, G. Abstreiter, and a Leitenstorfer, “How many-particle interactions develop after ultrafast excitation of an electron-hole plasma,” *Nature*, vol. 414, no. 6861, pp. 286–9, Nov. 2001.
- [21] H. Němec, P. Kužel, and V. Sundström, “Far-infrared response of free charge carriers localized in semiconductor nanoparticles,” *Physical Review B*, vol. 79, no. 11, p. 115309, Mar. 2009.
- [22] M. Schall, M. Walther, and P. Uhd Jepsen, “Fundamental and second-order phonon processes in CdTe and ZnTe,” *Physical Review B*, vol. 64, no. 9, p. 094301, Aug. 2001.
- [23] M. Zalkovskij, C. Zoffmann Bisgaard, A. Novitsky, R. Malureanu, D. Savastru, A. Popescu, P. Uhd Jepsen, and A. V. Lavrinenko, “Ultrabroadband terahertz spectroscopy of chalcogenide glasses,” *Applied Physics Letters*, vol. 100, no. 3, p. 031901, 2012.
- [24] G. M. Day, J. a Zeitler, W. Jones, T. Rades, and P. F. Taday, “Understanding the influence of polymorphism on phonon spectra: lattice dynamics calculations and terahertz

Bibliography

- spectroscopy of carbamazepine.," *The journal of physical chemistry. B*, vol. 110, no. 1, pp. 447–56, Jan. 2006.
- [25] U. Heugen, G. Schwaab, E. Bründermann, M. Heyden, X. Yu, D. M. Leitner, and M. Havenith, "Solute-induced retardation of water dynamics probed directly by terahertz spectroscopy.," *Proceedings of the National Academy of Sciences of the United States of America*, vol. 103, no. 33, pp. 12301–6, Aug. 2006.
- [26] D. H. Auston, "Picosecond optoelectronic switching and gating in silicon," *Applied Physics Letters*, vol. 26, no. 3, p. 101, 1975.
- [27] D. H. Auston, K. P. Cheung, and P. R. Smith, "Picosecond photoconducting Hertzian dipoles," *Applied Physics Letters*, vol. 45, no. 3, p. 284, 1984.
- [28] C. Fattinger and D. Grischkowsky, "Point source terahertz optics," *Applied Physics Letters*, vol. 53, no. 16, p. 1480, 1988.
- [29] D. Grischkowsky and M. Mandehgar, "The THz refractivity of water vapor," *2012 37th International Conference on Infrared, Millimeter, and Terahertz Waves*, pp. 1–3, Sep. 2012.
- [30] K. Sakai, *Terahertz optoelectronics*, 1st ed. Springer, 2005.
- [31] P. U. Jepsen, R. H. Jacobsen, and S. R. Keiding, "Generation and detection of terahertz pulses from biased semiconductor antennas," *Journal of the Optical Society of America B*, vol. 13, no. 11, p. 2424, Nov. 1996.
- [32] "www.picometrix.com."
- [33] P. C. Upadhyaya, W. Fan, A. Burnett, J. Cunningham, a G. Davies, E. H. Linfield, J. Lloyd-Hughes, E. Castro-Camus, M. B. Johnston, and H. Beere, "Excitation-density-dependent generation of broadband terahertz radiation in an asymmetrically excited photoconductive antenna.," *Optics letters*, vol. 32, no. 16, pp. 2297–9, Aug. 2007.
- [34] J. D. Buron, D. H. Petersen, P. Bøggild, D. G. Cooke, M. Hilke, J. Sun, E. Whiteway, P. F. Nielsen, O. Hansen, A. Yurgens, and P. U. Jepsen, "Graphene conductance uniformity mapping," *Nano letters*, vol. 12, no. 10, pp. 5074–81, Oct. 2012.
- [35] H. Hamster, A. Sullivan, and S. Gordon, "Subpicosecond, electromagnetic pulses from intense laser-plasma interaction," *Physical review ...*, vol. 71, no. 17, pp. 2725–2728, 1993.
- [36] D. J. Cook and R. M. Hochstrasser, "Intense terahertz pulses by four-wave rectification in air," vol. 25, no. 16, pp. 1210–1212, 2000.

Bibliography

- [37] M. Kress, T. Löff, S. Eden, M. Thomson, and H. G. Roskos, "Terahertz-pulse generation by photoionization of air with laser pulses composed of both fundamental and second-harmonic waves," vol. 29, no. 10, pp. 1120–1122, 2004.
- [38] T. Bartel, P. Gaal, K. Reimann, M. Woerner, and T. Elsaesser, "Generation of single-cycle THz transients with high electric-field amplitudes," vol. 30, no. 20, pp. 2805–2807, 2005.
- [39] X. Xie, J. Dai, and X.-C. Zhang, "Coherent Control of THz Wave Generation in Ambient Air," *Physical Review Letters*, vol. 96, no. 7, p. 075005, Feb. 2006.
- [40] J. Dai, X. Xie, and X. Zhang, "Detection of broadband terahertz waves with a laser-induced plasma in gases," *Physical review letters*, 2006.
- [41] N. Karpowicz, J. Dai, X. Lu, Y. Chen, M. Yamaguchi, H. Zhao, X.-C. Zhang, L. Zhang, C. Zhang, M. Price-Gallagher, C. Fletcher, O. Mamer, A. Lesimple, and K. Johnson, "Coherent heterodyne time-domain spectrometry covering the entire 'terahertz gap'," *Applied Physics Letters*, vol. 92, no. 1, p. 011131, 2008.
- [42] G. Vaillancourt, T. Norris, and J. Coe, "Operation of a 1-kHz pulse-pumped Ti: sapphire regenerative amplifier," *Optics letters*, vol. 15, no. 6, pp. 317–319, 1990.
- [43] C. S. Wang, J. M. Chen, R. Becker, and a. Zdetsis, "Second order Raman spectrum and phonon density of states of silicon," *Physics Letters A*, vol. 44, no. 7, pp. 517–518, Aug. 1973.
- [44] M. D. Thomson, V. Blank, and H. G. Roskos, "Terahertz white-light pulses from an air plasma photo-induced by incommensurate two-color optical fields.," *Optics express*, vol. 18, no. 22, pp. 23173–82, Oct. 2010.
- [45] E. Matsubara, M. Nagai, and M. Ashida, "Ultrabroadband coherent electric field from far infrared to 200 THz using air plasma induced by 10 fs pulses," *Applied Physics Letters*, vol. 101, no. 1, p. 011105, 2012.
- [46] M. Bass, P. Franken, J. Ward, and G. Weinreich, "Optical rectification," *Physical Review Letters*, vol. 9, no. 11, pp. 28–31, 1962.
- [47] M. C. Hoffmann and J. A. Fülöp, "Intense ultrashort terahertz pulses: generation and applications," *Journal of Physics D: Applied Physics*, vol. 44, no. 8, p. 083001, Mar. 2011.
- [48] D. H. Auston, "Subpicosecond electro-optic shock waves," *Applied Physics Letters*, vol. 43, no. 8, p. 713, 1983.
- [49] J. Hebling, G. Almasi, I. Kozma, and J. Kuhl, "Velocity matching by pulse front tilting for large area THz-pulse generation.," *Optics express*, vol. 10, no. 21, pp. 1161–6, Oct. 2002.

Bibliography

- [50] A. G. Stepanov, J. Hebling, and J. Kuhl, "Efficient generation of subpicosecond terahertz radiation by phase-matched optical rectification using ultrashort laser pulses with tilted pulse fronts," *Applied Physics Letters*, vol. 83, no. 15, p. 3000, 2003.
- [51] J. Hebling, A. G. Stepanov, G. Almasi, B. Bartal, and J. Kuhl, "Tunable THz pulse generation by optical rectification of ultrashort laser pulses with tilted pulse fronts," *Applied Physics B: Lasers and Optics*, vol. 78, no. 5, pp. 593–599, Mar. 2004.
- [52] K.-L. Yeh, M. C. Hoffmann, J. Hebling, and K. a. Nelson, "Generation of 10 μ J ultrashort terahertz pulses by optical rectification," *Applied Physics Letters*, vol. 90, no. 17, p. 171121, 2007.
- [53] J. a Fülöp, L. Pálfalvi, S. Klingebiel, G. Almási, F. Krausz, S. Karsch, and J. Hebling, "Generation of sub-mJ terahertz pulses by optical rectification.," *Optics letters*, vol. 37, no. 4, pp. 557–9, Feb. 2012.
- [54] S.-W. Huang, E. Granados, W. R. Huang, K.-H. Hong, L. E. Zapata, and F. X. Kärtner, "High conversion efficiency, high energy terahertz pulses by optical rectification in cryogenically cooled lithium niobate.," *Optics letters*, vol. 38, no. 5, pp. 796–8, Mar. 2013.
- [55] Q. Wu and X.-C. Zhang, "Free-space electro-optic sampling of terahertz beams," *Applied Physics Letters*, vol. 67, no. 24, p. 3523, 1995.
- [56] A. Nahata, D. H. Auston, T. F. Heinz, and C. Wu, "Coherent detection of freely propagating terahertz radiation by electro-optic sampling," *Applied Physics Letters*, vol. 68, no. 2, p. 150, 1996.
- [57] P. Jepsen, C. Winnewisser, M. Schall, V. Schyja, S. Keiding, and H. Helm, "Detection of THz pulses by phase retardation in lithium tantalate.," *Physical review. E, Statistical physics, plasmas, fluids, and related interdisciplinary topics*, vol. 53, no. 4, pp. R3052–R3054, Apr. 1996.
- [58] Yun-Shik Lee, *Principles of Terahertz Science and Technology*. Boston, MA: Springer US, 2009.
- [59] a. Leitenstorfer, S. Hunsche, J. Shah, M. C. Nuss, and W. H. Knox, "Detectors and sources for ultrabroadband electro-optic sampling: Experiment and theory," *Applied Physics Letters*, vol. 74, no. 11, p. 1516, 1999.
- [60] G. Gallot, J. Zhang, and R. McGowan, "Measurements of the THz absorption and dispersion of ZnTe and their relevance to the electro-optic detection of THz radiation," *Applied Physics ...*, 1999.
- [61] Q. Wu and X.-C. Zhang, "7 terahertz broadband GaP electro-optic sensor," *Applied Physics Letters*, vol. 70, no. 14, p. 1784, 1997.

Bibliography

- [62] H. Hirori, A. Doi, F. Blanchard, and K. Tanaka, "Single-cycle terahertz pulses with amplitudes exceeding 1 MV/cm generated by optical rectification in LiNbO₃," *Applied Physics Letters*, vol. 98, no. 9, p. 091106, 2011.
- [63] R. Frerichs, "New optical glasses with good transparency in the infrared," *JOSA*, vol. 43, no. 12, pp. 1153–1157, 1953.
- [64] A. Zakery, "Optical properties and applications of chalcogenide glasses: a review," *Journal of Non-Crystalline Solids*, vol. 330, no. 1–3, pp. 1–12, Nov. 2003.
- [65] B. J. Eggleton, B. Luther-Davies, and K. Richardson, "Chalcogenide photonics," *Nature Photonics*, vol. 5, no. 3, pp. 141–148, Feb. 2011.
- [66] T. Han, S. Madden, D. Bulla, and B. Luther-davies, "Low loss Chalcogenide glass waveguides by thermal nano-imprint lithography," *Optics Express*, vol. 18, no. 18, pp. 19286–19291, 2010.
- [67] S. Madden, D.-Y. Choi, D. A. Bulla, A. V Rode, B. Luther-Davies, V. G. Ta'eed, M. D. Pelusi, and B. J. Eggleton, "Long, low loss etched As₂S₃ chalcogenide waveguides for all-optical signal regeneration.," *Optics express*, vol. 15, no. 22, pp. 14414–21, Oct. 2007.
- [68] S. Wong, M. Deubel, F. Pérez-Willard, S. John, G. A. Ozin, M. Wegener, and G. von Freymann, "Direct Laser Writing of Three- Dimensional Photonic Crystals with a Complete Photonic Bandgap in Chalcogenide Glasses," *Advanced Materials*, vol. 18, no. 3, pp. 265–269, Feb. 2006.
- [69] E. P. J. Parrott, J. a. Zeitler, L. F. Gladden, S. N. Taraskin, and S. R. Elliott, "Extracting accurate optical parameters from glasses using terahertz time-domain spectroscopy," *Journal of Non-Crystalline Solids*, vol. 355, no. 37–42, pp. 1824–1827, Oct. 2009.
- [70] L. Duvillaret, F. Garet, and J. Coutaz, "A reliable method for extraction of material parameters in terahertz time-domain spectroscopy," *Selected Topics in Quantum ...*, 1996.
- [71] S. Taraskin, S. Simdyankin, S. Elliott, J. Neilson, and T. Lo, "Universal Features of Terahertz Absorption in Disordered Materials," *Physical Review Letters*, vol. 97, no. 5, p. 055504, Aug. 2006.
- [72] A. Ioffe and A. Regel, "Non-crystalline, amorphous and liquid electronic semiconductors," *Prog. Semicond*, pp. 236–291, 1960.
- [73] F. Billes, V. Mitsa, I. Fejes, N. Mateleshko, and I. Fejsa, "Calculation of the vibrational spectra of arsenic sulfide clusters," *Journal of Molecular Structure*, vol. 513, no. 1–3, pp. 109–115, Dec. 1999.

Bibliography

- [74] D. G. Georgiev, P. Boolchand, and K. a. Jackson, "Intrinsic nanoscale phase separation of bulk As_2S_3 glass," *Philosophical Magazine*, vol. 83, no. 25, pp. 2941–2953, Sep. 2003.
- [75] H. Whitfield, "The far-infrared spectra of arsenic chalcogenides," *Aust. J. Chem.*, vol. 1, no. 24, pp. 697–701, 1971.
- [76] C. Yang, M. Paesler, and D. Sayers, "Chemical order in the glassy $\text{As}_x\text{S}_{1-x}$ system: An x-ray-absorption spectroscopy study," *Physical Review B*, vol. 39, no. 14, 1989.
- [77] M. C. Hoffmann, N. C. Brandt, H. Y. Hwang, K.-L. Yeh, and K. A. Nelson, "Terahertz Kerr effect," *Applied Physics Letters*, vol. 95, no. 23, p. 231105, 2009.
- [78] J. M. Harbold, F. O. Ilday, F. W. Wise, J. S. Sanghera, V. Q. Nguyen, L. B. Shaw, and I. D. Aggarwal, "Highly nonlinear As-S-Se glasses for all-optical switching," *Optics letters*, vol. 27, no. 2, pp. 119–21, Jan. 2002.
- [79] M. Zalkovskij, C. Zoffmann Bisgaard, A. Novitsky, R. Malureanu, D. Savastru, A. Popescu, P. Uhd Jepsen, and A. V. Lavrinenko, "Ultrabroadband terahertz spectroscopy of chalcogenide glasses," *Applied Physics Letters*, vol. 100, no. 3, p. 031901, 2012.
- [80] K. Ogusu, J. Yamasaki, S. Maeda, M. Kitao, and M. Minakata, "Linear and nonlinear optical properties of Ag-As-Se chalcogenide glasses for all-optical switching," *Optics letters*, vol. 29, no. 3, pp. 265–7, Feb. 2004.
- [81] F. Smektala, C. Quemard, L. Leneindre, J. Lucas, A. Barthélémy, and C. De Angelis, "Chalcogenide glasses with large non-linear refractive indices," *Journal of Non-Crystalline Solids*, vol. 239, no. 1–3, pp. 139–142, Oct. 1998.
- [82] H. Kobayashi, H. Kanbara, M. Koga, and K. Kubodera, "Third-order nonlinear optical properties of As_2S_3 chalcogenide glass," *Journal of Applied Physics*, vol. 74, no. 6, p. 3683, 1993.
- [83] M. A. Seo, H. R. Park, S. M. Koo, D. J. Park, J. H. Kang, O. K. Suwal, S. S. Choi, P. C. M. Planken, G. S. Park, N. K. Park, Q. H. Park, and D. S. Kim, "Terahertz field enhancement by a metallic nano slit operating beyond the skin-depth limit," *Convergence*, vol. 3, no. March, 2009.
- [84] Q.-H. Park, "Optical antennas and plasmonics," *Contemporary Physics*, vol. 50, no. 2, pp. 407–423, Mar. 2009.
- [85] A. Novitsky, M. Zalkovskij, R. Malureanu, and a. Lavrinenko, "Microscopic model of the THz field enhancement in a metal nanoslit," *Optics Communications*, vol. 284, no. 23, pp. 5495–5500, Nov. 2011.
- [86] O. Geschke, H. Klank, and P. Tellemann, *Microsystem engineering of lab-on-a-chip devices*. 2004, p. 2004.

Bibliography

- [87] K. N. Tu, "Recent advances on electromigration in very-large-scale-integration of interconnects," *Journal of Applied Physics*, vol. 94, no. 9, p. 5451, 2003.
- [88] C. Durkan, M. a. Schneider, and M. E. Welland, "Analysis of failure mechanisms in electrically stressed Au nanowires," *Journal of Applied Physics*, vol. 86, no. 3, p. 1280, 1999.
- [89] P. Ho and H. Huntington, "Electromigration and void observation in silver," *Journal of Physics and Chemistry of Solids*, vol. 27, pp. 1319–1329, 1966.
- [90] H.-T. Chen, J. F. O'Hara, A. K. Azad, and A. J. Taylor, "Manipulation of terahertz radiation using metamaterials," *Laser & Photonics Reviews*, vol. 5, no. 4, pp. 513–533, Jul. 2011.
- [91] L. Zhou, C. T. Chan, and P. Sheng, "Theoretical studies on the transmission and reflection properties of metallic planar fractals," *Journal of Physics D: Applied Physics*, vol. 37, no. 3, pp. 368–373, Feb. 2004.
- [92] G. Kenanakis, R. Zhao, a. Stavrinidis, G. Konstantinidis, N. Katsarakis, M. Kafesaki, C. M. Soukoulis, and E. N. Economou, "Flexible chiral metamaterials in the terahertz regime: a comparative study of various designs," *Optical Materials Express*, vol. 2, no. 12, p. 1702, Nov. 2012.
- [93] R. Singh, E. Plum, W. Zhang, and N. I. Zheludev, "Highly tunable optical activity in planar achiral terahertz metamaterials.," *Optics express*, vol. 18, no. 13, pp. 13425–30, Jun. 2010.
- [94] C. M. Soukoulis and M. Wegener, "Past achievements and future challenges in the development of three-dimensional photonic metamaterials," *Nature Photonics*, vol. 5, no. SEPTEMBER, Jul. 2011.
- [95] J. Zhou, D. R. Chowdhury, R. Zhao, A. K. Azad, H.-T. Chen, C. M. Soukoulis, A. J. Taylor, and J. F. O'Hara, "Terahertz chiral metamaterials with giant and dynamically tunable optical activity," *Physical Review B*, vol. 86, no. 3, p. 035448, Jul. 2012.
- [96] S. Zhang, Y.-S. Park, J. Li, X. Lu, W. Zhang, and X. Zhang, "Negative Refractive Index in Chiral Metamaterials," *Physical Review Letters*, vol. 102, no. 2, pp. 1–4, Jan. 2009.
- [97] R. Singh, E. Plum, C. Menzel, C. Rockstuhl, a. Azad, R. Cheville, F. Lederer, W. Zhang, and N. Zheludev, "Terahertz metamaterial with asymmetric transmission," *Physical Review B*, vol. 80, no. 15, pp. 4–7, Oct. 2009.
- [98] K. Iwaszczuk, A. C. Strikwerda, K. Fan, X. Zhang, R. D. Averitt, and P. U. Jepsen, "Flexible metamaterial absorbers for stealth applications at terahertz frequencies.," *Optics express*, vol. 20, no. 1, pp. 635–43, Jan. 2012.

Bibliography

- [99] H. Tao, A. C. Strikwerda, M. Liu, J. P. Mondia, E. Ekmekci, K. Fan, D. L. Kaplan, W. J. Padilla, X. Zhang, R. D. Averitt, and F. G. Omenetto, "Performance enhancement of terahertz metamaterials on ultrathin substrates for sensing applications," *Applied Physics Letters*, vol. 97, no. 26, p. 261909, 2010.
- [100] H. Tao, J. J. Amsden, A. C. Strikwerda, K. Fan, D. L. Kaplan, X. Zhang, R. D. Averitt, and F. G. Omenetto, "Metamaterial silk composites at terahertz frequencies.," *Advanced materials (Deerfield Beach, Fla.)*, vol. 22, no. 32, pp. 3527–31, Aug. 2010.
- [101] H. Tao, L. R. Chieffo, M. A. Brenckle, S. M. Siebert, M. Liu, A. C. Strikwerda, K. Fan, D. L. Kaplan, X. Zhang, R. D. Averitt, and F. G. Omenetto, "Metamaterials on paper as a sensing platform.," *Advanced materials (Deerfield Beach, Fla.)*, vol. 23, no. 28, pp. 3197–201, Jul. 2011.
- [102] S. V Zhukovsky, C. Kremers, and D. N. Chigrin, "Plasmonic rod dimers as elementary planar chiral meta-atoms.," *Optics letters*, vol. 36, no. 12, pp. 2278–80, Jun. 2011.
- [103] C. Rockstuhl and F. Lederer, "Negative-index metamaterials from nanoapertures," *Physical Review B*, vol. 76, no. 12, p. 125426, Sep. 2007.
- [104] F. Falcone, T. Lopetegui, M. Laso, J. Baena, J. Bonache, M. Beruete, R. Marqués, F. Martín, and M. Sorolla, "Babinet Principle Applied to the Design of Metasurfaces and Metamaterials," *Physical Review Letters*, vol. 93, no. 19, pp. 2–5, Nov. 2004.
- [105] L. Zhang, T. Koschny, and C. M. Soukoulis, "Creating double negative index materials using the Babinet principle with one metasurface," *Physical Review B*, vol. 87, no. 4, p. 045101, Jan. 2013.
- [106] a D. Rakic, a B. Djurisic, J. M. Elazar, and M. L. Majewski, "Optical properties of metallic films for vertical-cavity optoelectronic devices.," *Applied optics*, vol. 37, no. 22, pp. 5271–83, Aug. 1998.
- [107] D. N. Chigrin, C. Kremers, and S. V. Zhukovsky, "Plasmonic nanoparticle monomers and dimers: from nanoantennas to chiral metamaterials," *Applied Physics B*, vol. 105, no. 1, pp. 81–97, Sep. 2011.
- [108] J.-H. Choe, J.-H. Kang, D.-S. Kim, and Q.-H. Park, "Slot antenna as a bound charge oscillator.," *Optics express*, vol. 20, no. 6, pp. 6521–6, Mar. 2012.
- [109] G. Borzdov, "Elastic and sound orthonormal beams and localized fields in linear mediums: I. Basic equations," *Journal of Physics A: Mathematical and General*, vol. 6249, 2001.
- [110] L. Barkovskii, G. Borzdov, and a V Lavrinenko, "Fresnel's reflection and transmission operators for stratified gyroanisotropic media," *Journal of Physics A: ...*, vol. 1095, 1987.

Bibliography

- [111] F. J. Garcia-Vidal, T. W. Ebbesen, and L. Kuipers, "Light passing through subwavelength apertures," *Reviews of Modern Physics*, vol. 82, no. 1, pp. 729–787, Mar. 2010.
- [112] Y.-M. Bahk, J.-W. Choi, J. Kyoung, H.-R. Park, K. J. Ahn, and D.-S. Kim, "Selective enhanced resonances of two asymmetric terahertz nano resonators.," *Optics express*, vol. 20, no. 23, pp. 25644–53, Nov. 2012.
- [113] Z. Li, K. B. Alici, E. Colak, and E. Ozbay, "Complementary chiral metamaterials with giant optical activity and negative refractive index," *Applied Physics Letters*, vol. 98, no. 16, p. 161907, 2011.
- [114] S. Engelbrecht, M. Wunderlich, a. M. Shuvaev, and a. Pimenov, "Colossal optical activity of split-ring resonator arrays for millimeter waves," *Applied Physics Letters*, vol. 97, no. 8, p. 081116, 2010.
- [115] D. S. Hecht, L. Hu, and G. Irvin, "Emerging Transparent Electrodes Based on Thin Films of Carbon Nanotubes, Graphene, and Metallic Nanostructures," *Advanced Materials*, vol. 23, no. 13, pp. 1482–1513, Apr. 2011.
- [116] M. Vosgueritchian, D. J. Lipomi, and Z. Bao, "Highly Conductive and Transparent PEDOT:PSS Films with a Fluorosurfactant for Stretchable and Flexible Transparent Electrodes," *Advanced Functional Materials*, vol. 22, no. 2, pp. 421–428, Jan. 2012.
- [117] R. Bel Hadj Tahar, T. Ban, Y. Ohya, and Y. Takahashi, "Tin doped indium oxide thin films: Electrical properties," *Journal of Applied Physics*, vol. 83, no. 5, p. 2631, 1998.
- [118] D. R. Cairns, R. P. Witte, D. K. Sparacin, S. M. Sachsman, D. C. Paine, G. P. Crawford, and R. R. Newton, "Strain-dependent electrical resistance of tin-doped indium oxide on polymer substrates," *Applied Physics Letters*, vol. 76, no. 11, p. 1425, 2000.
- [119] T. W. Ebbesen, H. J. Lezec, H. F. Chaemi, T. Thio, and H. F. Wolff, "Extraordinary optical transmission through sub-wavelength hole arrays," *Nature*, vol. 391, p. 667, Feb. 1998.
- [120] J. A. Porto and F. J. Garci, "Transmission Resonances on Metallic Gratings with Very Narrow Slits," pp. 2845–2848, 1999.
- [121] L. Zhou, W. Wen, C. T. Chan, and P. Sheng, "Electromagnetic-Wave Tunneling Through Negative-Permittivity Media with High Magnetic Fields," *Physical Review Letters*, vol. 94, no. 24, p. 243905, Jun. 2005.
- [122] D. J. Bergman, "THE DIELECTRIC CONSTANT OF A COMPOSITE MATERIAL IN CLASSICAL PHYSICS* David J. BERGMAN," vol. 9, no. 9, pp. 377–407, 1978.
- [123] J. Pendry, A. Holden, W. Stewart, and I. Youngs, "Extremely low frequency plasmons in metallic mesostructures.," *Physical review letters*, vol. 76, no. 25, pp. 4773–4776, Jun. 1996.

Bibliography

- [124] M. Naftaly and R. E. Miles, "Terahertz time-domain spectroscopy of silicate glasses and the relationship to material properties," *Journal of Applied Physics*, vol. 102, no. 4, p. 043517, 2007.
- [125] M. a Ordal, L. L. Long, R. J. Bell, S. E. Bell, R. R. Bell, R. W. Alexander, and C. a Ward, "Optical properties of the metals Al, Co, Cu, Au, Fe, Pb, Ni, Pd, Pt, Ag, Ti, and W in the infrared and far infrared.," *Applied optics*, vol. 22, no. 7, pp. 1099–20, Apr. 1983.